NATIONAL TECHNICAL UNIVERSITY OF ATHENS
SCHOOL OF ELECTRICAL AND COMPUTER ENGINEERING
SCHOOL OF MECHANICAL ENGINEERING

INTERDISCIPLINARY POSTGRADUATE PROGRAMME
Translational Engineering in Health and Medicine

Development of a Robust Algorithm for 3D-Rendering of Multi-2D Electromechanical Wave Imaging Maps and CT Registration

---

Postgraduate Diploma Thesis

Aikaterini Afentouli

Supervisor
Dr. Konstantina S. Nikita
Professor in School of Electrical and Computer Engineering
National Technical University of Athens

Co-Supervisor
Dr. Elisa E. Konofagou
Professor of Biomedical Engineering and Radiology
Columbia University in the City of New York

Athens, October 2024

NATIONAL TECHNICAL UNIVERSITY OF ATHENS
SCHOOL OF ELECTRICAL AND COMPUTER ENGINEERING
SCHOOL OF MECHANICAL ENGINEERING

INTERDISCIPLINARY POSTGRADUATE PROGRAMME
"Translational Engineering in Health and Medicine"

Development of a Robust Algorithm for 3D-Rendering of Multi-2D Electromechanical Wave Imaging Maps and CT Registration

---

Postgraduate Diploma Thesis

Aikaterini Afentouli

Supervisor
Dr. Konstantina S. Nikita
Professor in School of Electrical and Computer Engineering
National Technical University of Athens

Co-Supervisor
Dr. Elisa E. Konofagou
Professor of Biomedical Engineering and Radiology
Columbia University in the City of New York

The postgraduate diploma thesis has been approved by the examination committee on October 14th, 2024

1st member	*2nd member*	*3rd member*
Dr. Konstantina S. Nikita	**Dr. Elisa E. Konofagou**	**Dr. Athanasios Voulodimos**
(Prof. in NTUA)	*(Prof. in Columbia University)*	*(Asst. Prof. in NTUA)*

Athens, October 2024

Aikaterini Afentouli
Graduate of the Interdisciplinary Postgraduate Programme,
"Translational Engineering in Health and Medicine",
Master of Science,
School of Electrical and Computer Engineering,
National Technical University of Athens

NATIONAL TECHNICAL UNIVERSITY OF ATHENS

Abstract

Translational Engineering in Health & Medicine
School of Electrical and Computer Engineering

Master's of Science

Development of a Robust Algorithm for 3D-Rendering of Multi-2D Electromechanical Wave Imaging Maps and CT Registration

by Aikaterini Afentouli

This study addresses the need for improved, non-invasive localization of arrhythmogenic sources in cardiac arrhythmias, which are common and can be life-threatening if untreated. Current methods for arrhythmia characterization can be either imprecise or highly invasive, limiting their clinical accessibility. Electromechanical Wave Imaging (EWI), a non-invasive ultrasound-based modality, offers real-time 2D and 3D maps of the heart's electrical activation and holds promise for advancing arrhythmia localization.

The primary objective of this thesis is to develop an advanced algorithm for rendering multiple 2D EWI views, improving cardiac arrhythmia localization and enhancing clinical utility. This work also introduces a 3D registration process with cardiac CT data to refine anatomical accuracy and provide patient-specific insights.

Significant upgrades to the existing 3D EWI algorithm focused on increasing automation, flexibility, and accuracy in visualizing the heart's electromechanical activity. Additionally, 3D point clouds were registered to CT data, followed by non-rigid surface registration to align 3D EWI maps with CT-derived anatomy.

Key findings show improvements in spatial coverage and activation mapping accuracy, particularly in under-sampled regions, with the inclusion of structures like the left ventricular outflow tract (LVOT) and mitral valve. The development of a user-friendly graphical interface enhances accessibility for researchers and clinicians. The fusion of functional EWI data with anatomical CT models allows more precise arrhythmia localization, which may lead to improved treatment outcomes.

In conclusion, this thesis enhances the accuracy, efficiency, and usability of 3D EWI, positioning it as a more robust and clinically viable tool for studying and treating cardiac conditions. Algorithmic improvements, enhanced visualization, and user-centered design push the boundaries of current EWI technology, making it more adaptable and easier to implement in clinical practice.

Keywords: *Cardiac arrhythmias, Arrhythmia localization, Ultrasound, Echocardiography, Electromechanical Wave Imaging (EWI), Electromechanical activation, Image processing, 3D rendering, Computational Geometry, Cardiac computed tomography (CT), Spatial registration, 3D registration*

"The more I find out, the more I realize that I don't know what's going on."

- Frank Herbert

Acknowledgements

I would like to express my deepest gratitude to my supervisor, Dr. Konstantina Nikita, Professor in the School of Electrical and Computer Engineering at the National Technical University of Athens (NTUA) and Director of the Master's in Translational Engineering in Health and Medicine. Thank you for giving me the opportunity to participate in this MSc program and for the chance to undertake an internship at Columbia University. This experience has truly been life-changing, and I would not be where I am today without it.

Furthermore, I would like to express my heartfelt appreciation to my co-super-visor, Dr. Elisa E. Konofagou, Professor of Biomedical Engineering and Radiology at Columbia University in the City of New York, USA. Thank you for entrusting me with the opportunity to work alongside you and your team in the Ultrasound and Elasticity Imaging Laboratory. My time there has evolved into something more meaningful than I ever expected. I am truly grateful for the opportunities and the freedom to engage in such an interesting and important research project.

I would also like to thank everyone who has provided guidance during this time. A million thanks to PhD student Melina Tourni at UEIL for her invaluable guidance and feedback throughout this project. Our meetings and conversations played a vital role in ensuring a smooth working environment and the successful progress of the project.

Last but not least, I would like to thank my family and friends for their unwavering faith and support during significant milestones and for their humor during the more challenging periods. You truly lift me up.

Contents

List of Figures

List of Tables

List of Abbreviations

2D	**T**wo-**D**imensional
3D	**T**hree-**D**imensional
4C	**F**our-**C**hamber
AP	**A**ccessory **P**athways
ASE	**A**merican **S**ociety of **E**chocardiography
ANT	**A**nterior
A	**A**pical
A2C	**A**pical **2** **C**hamber
A3C	**A**pical **3** **C**hamber
A3.5C	**A**pical **3.5** **C**hamber
A4C	**A**pical **4** **C**hamber
A5C	**A**pical **5** **C**hamber
ARVC	**A**rrhythmogenic **R**ight **V**entricular **C**ardiomyopathy
Ao	**A**orta
AFib	**A**trial **F**ibrillation
AFL	**A**trial **F**lutter
AT	**A**trial **T**achycardia
AV	**A**trio**v**entricular
BMI	**B**ody **M**ass **I**ndex
CRT	**C**ardiac **R**esynchronization **T**herapy
CMR	**C**ardiac **M**agnetic **R**esonance **I**maging
CT	**C**omputed **T**omography
DCM	**D**ilated **C**ardiomyopathy
EF	**E**jection **F**raction
ECGi	**E**lectro**c**ardiographic **I**maging
EAM	**E**lectro**a**natomic **M**apping
ECG	**E**lectro**c**ardiogram
EWI	**E**lectromechanical **W**ave **I**maging
EP	**E**lectrophysiology
EDL	**E**quivalent **D**ouble **L**ayer
FOV	**F**ield-**O**f-**V**iew
GUI	**G**raphical **U**ser **I**nterface
IVC	**I**nferior **V**ena **C**ava
ICE	**I**ntra**c**ardiac **E**chocardiography
ICP	**I**terative **C**losest **P**oint
LAT	**L**ateral
LGE	**L**ate **G**adolinium **E**nhancement
LA	**L**eft **A**trium
LV	**L**eft **V**entricle
LVOT	**L**eft **V**entricular **O**utflow **T**ract
LAX	**L**ong **A**xis

MRI	**M**agnetic **R**esonance **I**maging
MMI	**M**ulti**m**odal **I**maging
NRICP	**N**on-**R**igid **I**terative **C**losest **P**oint
NSR	**N**ormal **S**inus **R**hythm
P	**P**arasternal
PLAX	**P**arasternal **L**ong-**A**xis
PSAX	**P**arasternal **S**hort-**A**xis
PZE	**P**iezo**e**lectric
PET-CT	**P**ositron **E**mission **T**omography-**C**omputed **T**omography
PVCs	**P**remature **V**entricular **C**ontractions
POST	**P**osterior
RF	**R**adio-**F**requency
RFA	**R**adio-**F**requency **A**blation
RA	**R**ight **A**trium
RV	**R**ight **V**entricle
RVIT	**R**ight **V**entricular **I**nflow **T**ract
RVOT	**R**ight **V**entricular **O**utflow **T**ract
SAX	**S**hort **A**xis
SA	**S**ino**a**trial
STE	**S**peckle **T**racking **E**chocardiography
SC	**S**ub**c**ostal
SCD	**S**udden **C**ardiac **D**eath
SSN	**S**upra**s**ternal **N**otch
SVTs	**S**upra**v**entricular **A**rrhythmias
TTE	**T**ransthoracic **E**chocardiography
TV	**T**ricuspid **V**alve
UNISYS	**U**niversal **V**entricular **B**ullseye **V**isualization
VE	**V**entricular **E**ctopy
VFib	**V**entricular **F**ibrillation
VT	**V**entricular **T**achycardia
ZC	**Z**ero-**C**rossings

List of Symbols

A	amplitude	m
f	frequency	Hz
I	intensity	$\mathrm{W\,m^{-2}}$
T	period	s
V	velocity	$\mathrm{m\,s^{-1}}$
λ	wavelength	m

For the times when "just keep swimming" was enough.

Chapter 1

Introduction

1.1 Cardiovascular Diseases and Arrhythmias

The heart is one of the most vital organs in the human body, relying on complex mechanisms to maintain life. Despite extensive research and advances in healthcare, heart disease remains the leading cause of death worldwide; in the European Union alone, cardiovascular diseases were responsible for nearly one-third (32.4%) of all deaths in 2021[1, 2, 3].

Among the various conditions affecting the heart, arrhythmias— irregularities in the heart's rhythm—are particularly significant. Arrhythmias occur when the heart's electrical signals are disrupted, causing an abnormal heartbeat. Some common types include atrial or ventricular fibrillation (AF/VF), premature atrial or ventricular contractions (PACs/PVCs), Wolff-Parkinson-White syndrome, and heart block. AF and VF, in particular, are among the most serious arrhythmias. AF alone was linked to 219.4 thousand documented deaths globally in 2019[4], with a mortality rate of 15.3 per 100,000 population in Europe during the same year[5].

Cardiovascular diseases are projected to increase by 40% by 2030, with the aging global population being primarily impacted. Within the European Union, over 14 million people over the age of 65 are expected to be affected from AF[6]. Patients with AF often experience distressing symptoms such as palpitations, chest pain, dizziness, and heart failure-like conditions, all of which severely affect their quality of life and physical capacity. Furthermore, the side effects of treatments, frequent hospitalizations, and the invasive nature of certain interventions can significantly diminish a patient's overall well-being[7, 8]. The goal of modern healthcare is not only to extend patient lifespans, but also to enhance their quality of life through effective and minimally invasive treatments. However, current healthcare systems face substantial challenges in diagnosing and treating cardiac arrhythmias. Advanced diagnostic tools and interventions often require specialized medical equipment and highly trained personnel, which are not always readily available, particularly in resource-constrained environments such as low- and middle-income countries[9]. With the expected rise in cardiovascular disease, there is a growing need for faster, more accurate, and accessible methods for diagnosing and treating cardiac arrhythmias.

Although many arrhythmias are not life-threatening and may not require immediate treatment, others pose significant risks and can even lead to sudden cardiac death (SCD)[10]. SCD affects approximately 1 in 1,000 people each year in Western countries, with up to 20% of these cases showing no

clear structural heart disease[11]. The most common cause of SCD is the failure of the heart to contract properly due to dangerous arrhythmias, which disrupt blood flow to vital organs. Early detection and accurate spatiotemporal mapping of cardiac arrhythmias are critical for reducing the risk of fatal events and ensuring timely intervention and treatment.

Currently, the electrocardiogram (ECG) remains the most widely used non-in-vasive tool for diagnosing and characterizing arrhythmias[12]. It is a simple and non-invasive test that can be performed on any patient, but its ability to accurately localize the source of the arrhythmia is limited. For more precise diagnosis, electrophysiology (EP) studies are often employed. This invasive procedure involves threading catheters into the heart to intracardially record electrical activity, making it a reliable method for diagnosing and treating arrhythmias. However, its invasiveness, radiation exposure and the need for specialized facilities make it less accessible to all patients. Additional imaging techniques, such as echocardiography, computed tomography (CT), and magnetic resonance imaging (MRI), are often necessary to provide detailed anatomical assessments[13]. Echocardiography, using ultrasound, offers real-time images of heart structure and function but lacks detailed electrical information. CT provides high spatial resolution images of the heart and vessels, but exposes patients to radiation. MRI, while excellent for soft tissue contrast and avoiding radiation, is time-consuming and costly. Despite these advances, there is still a significant need for non-invasive, accurate, and efficient imaging technologies to bridge the gap between current capabilities and clinical demands.

In response to these challenges, Electromechanical Wave Imaging (EWI) has emerged as a promising, non-invasive imaging modality that builds upon the principles of echocardiography. EWI provides real-time, high-resolution 2D and 3D maps of the heart's electromechanical activity by tracking the mechanical deformations caused by electrical activation in the myocardium. Unlike traditional imaging methods, EWI captures both electrical and mechanical aspects of cardiac function, enabling more precise localization of arrhythmia origins without the need for invasive procedures[14]. Furthermore, EWI can be performed with standard ultrasound equipment, making it a cost-effective and accessible tool for diagnosing and managing cardiac arrhythmias. By offering real-time feedback during procedures such as catheter ablation and cardiac resynchronization therapy, EWI has the potential to improve treatment outcomes and reduce the risks associated with arrhythmia-related complications.

1.2 Scope and Aims

Building upon the foundational principles of Electromechanical Wave Imaging (EWI), the scope of this thesis encompasses significant improvements to the existing 3D electromechanical activation map generation algorithm. These advancements aim to make the system more clinically viable, providing improved accuracy, flexibility, and ease of use for both researchers and clinicians. Specifically, the thesis addresses several key research objectives:

- *Algorithm Enhancements and Automation*: The first goal is to refine the current 3D rendering algorithm by automating many of the processes that were previously manual and time-intensive. This includes eliminating the need for direct code manipulation and integrating steps into a streamlined workflow, thus reducing the potential for user error and making the technology more accessible for non-technical users. The algorithm will also be made view-agnostic, allowing for flexible rendering of any apical views focused on the left ventricle (LV), which in turn improves the coverage of under-sampled areas and enhances data representation.

- *User Interface and Clinical Usability*: To make the technology more accessible for widespread clinical use, a graphical user interface (GUI) will be developed to consolidate all functionalities. This interface will simplify the complex processes involved in EWI, facilitating smoother interactions for users and reducing the time required for data processing. These upgrades aim to enable users to visualize 3D electromechanical maps in real time.

- *Co-registration of EWI Data with Patient CT Scans*: Another central aim of this thesis is to enhance the anatomical accuracy of the electromechanical activation maps by achieving spatial registration between 3D-rendered EWI data and patient-specific CT scans. By projecting the EWI-derived activation data onto the CT-based anatomical shell, this research introduces a novel technique for integrating electromechanical and anatomical information. This fusion of modalities is expected to deliver a more personalized and spatially precise representation of cardiac activity, thereby improving the clinical relevance of the maps in diagnosing and treating complex arrhythmias.

By addressing these objectives, this thesis aims to not only improve the accuracy and efficiency of 3D-rendered EWI rendering but also to position it as a robust, clinically viable tool for studying and treating various cardiac conditions. Through a combination of algorithmic refinements, enhanced visualization techniques, and user-centered design, the work presented here seeks to push the boundaries of current EWI technology, making it more adaptable, reliable, and easier to implement in clinical settings.

1.3 Thesis Outline

This thesis is organized into five chapters to guide the reader through the research on advancing Electromechanical Wave Imaging (EWI) technology. It begins with foundational concepts and progressively delves into specific methodologies, results, and discussions related to two main topics of investigation.

The Literature Review (Chapter 2) provides an extensive background on heart anatomy, function, and the clinical significance of arrhythmias. It reviews current clinical imaging techniques used for arrhythmia localization, such as electrocardiography, echocardiography, and intracardiac mapping, as well as research methods like Electrocardiographic Imaging (ECGi) and

Electromechanical Wave Imaging (EWI). The thesis is then divided into the two main sections, each focusing on a key area of research.

Chapter 3 discusses the advanced 3D rendering algorithm development for 2D EWI. A more detailed focus is placed on EWI, describing its principles, the physics behind echocardiography, and current methods for 3D rendering of electromechanical maps, setting the stage for subsequent technical advancements explored. It outlines the methodology for refining the 3D rendering EWI algorithm to improve accuracy, efficiency, and clinical usability and describes the steps taken to automate manual processes, implement view-agnostic rendering, and develop a user-friendly graphical interface. The results and discussion section compares improvements in rendering performance and usability with the original algorithm and evaluates the benefits for real-time clinical applications.

Chapter 4 shifts focus to the 3D Registration of EWI and CT Models. This section explores the spatial integration of electromechanical data from EWI with patient-specific anatomical models derived from CT scans. The chapter presents the methodologies used for achieving this registration, including the Iterative Closest Point (ICP) and Non-Rigid ICP algorithms. It then discusses the results of the registration process and evaluates its clinical significance, with a focus on the potential for enhanced anatomical accuracy and personalized treatment. Like Chapter 3, it includes dedicated methods, results and discussion sections.

Finally, in Chapter 5, the Conclusions and Future Work, the thesis provides an overarching discussion of the findings from both main sections, integrating the outcomes of the advanced rendering and 3D registration processes. This chapter addresses the broader implications of the research, discusses the limitations encountered during the study, and outlines potential future directions for further refinement of EWI technology. The chapter concludes by reflecting on the potential impact of these advancements on clinical practice and the management of cardiac arrhythmias.

1.4 Disclaimer

This work was completed in partial fulfillment of the requirements for the Master of Science degree in the Translational Engineering in Health & Medicine program, within the School of Electrical and Computer Engineering. The research and development described in this thesis were conducted in collaboration with the Ultrasound and Elasticity Imaging Laboratory at Columbia University in the City of New York. All work, data, and results presented in this thesis are the intellectual property of Dr. Elisa Konofagou and Columbia University in the City of New York. All images used in this thesis were either created by the author or adapted from external sources. A detailed table of image sources is provided in Appendix B for reference.

Chapter 2

Literature Review

2.1 Heart Anatomy and Function

The heart is one of the most vital organs in all living beings, serving as a central component of the cardiovascular system. It is a muscular organ responsible for ensuring continuous and efficient circulation of blood throughout the body. As part of the circulatory system, the heart functions as a pump, transmitting oxygenated blood to tissues while also receiving deoxygenated blood for reoxygenation, thus maintaining the cycle of circulation.

In the standard anatomical position (upright body, facing forward, arms at the sides, and legs parallel), the heart is situated between the lungs beneath the sternum, with its lower tip, or apex, pointing slightly to the left. Here, left and right are referenced in terms of anatomical orientation. Structurally, the heart is divided into four chambers: the upper left and right atria, and the lower left and right ventricles, all of which are surrounded by robust muscular walls. A thick wall of muscle named septum separates the left and right side of the heart. The left atrium communicates with the left ventricle via the mitral valve, while the right atrium is connected to the right ventricle through the tricuspid valve. Additional heart valves include the pulmonary and aortic valves, all of which function as one-way valves to prevent backflow. The left ventricular outflow tract (LVOT), located within the left ventricle, connects to the aorta and facilitates the flow of oxygenated blood from the heart to the rest of the body. Several major blood vessels are directly associated with the heart's chambers to facilitate circulation, including the aorta, pulmonary artery, pulmonary veins, and the superior and inferior venae cavae. The anatomical positioning of the heart within the thoracic cavity and a detailed schematic of its internal structures are shown in Figure 2.1. The heart muscle, or myocardium, also requires its own oxygen supply, which is delivered by the coronary arteries.

Several anatomical regions can be identified around the left ventricular (LV) walls based on their orientation within the thoracic cavity. The posterior region refers to the area of the LV facing the spine, while the inferior region lies closest to the sternum. The septal region comprises the walls of the septum and can be further subdivided into the anteroseptal and posterior septal segments, based on their proximity to the anterior or posterior aspects of the heart. Finally, the region towards the patient's left side is termed the lateral region. The lateral wall can be further categorized depending on its position relative to adjacent areas: the anterolateral or posterior lateral regions.

A simplified overview of a normal cardiac cycle is shown in Figure 2.2 and can be described as follows: during a period of relaxation, deoxygenated

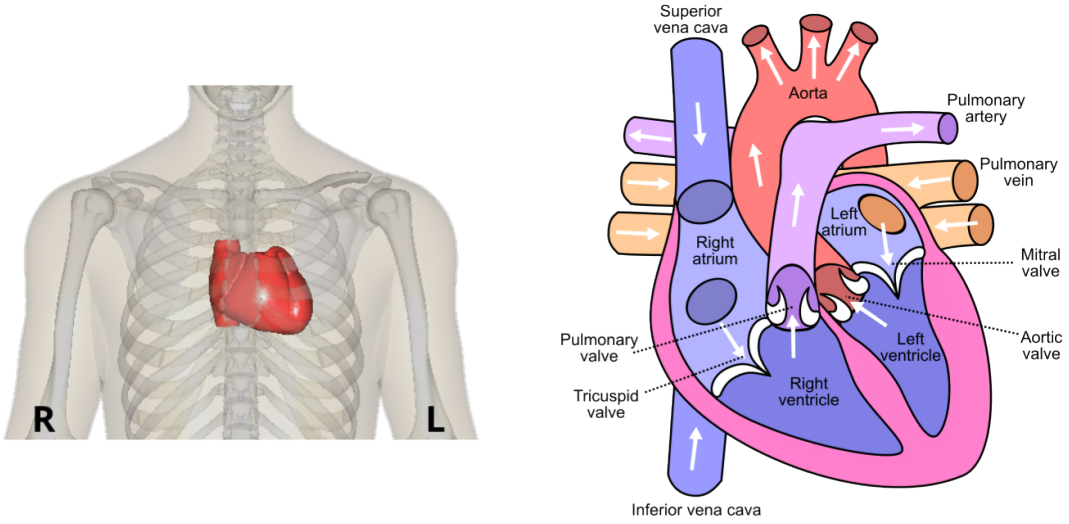

Figure 2.1: (a) Anatomical positioning of the heart relative to the human chest, showing the ribs and heart location within the thoracic cavity. (b) Detailed schematic of the heart's key internal structures, including the left and right ventricles, atria, valves, and major arteries.

blood enters the right atrium via the superior and inferior venae cavae. It then passes through the tricuspid valve into the right ventricle, which subsequently contracts, pushing blood through the pulmonary valve into the pulmonary artery, where it is transported to the lungs for oxygenation. Simultaneously, oxygenated blood from the lungs returns to the left atrium via the pulmonary veins. It is then passed through the mitral valve into the left ventricle, where it is ejected through the aortic valve into the aorta for systemic distribution. This process is continuous, with both sides of the heart working in tandem. The cyclical nature of cardiac function relies on alternating phases of contraction and relaxation, known as systole and diastole, respectively. Systole refers to the contraction phase, where blood is actively ejected from the ventricles, while diastole refers to the relaxation phase, allowing for ventricular filling[15, 16].

The coordinated contraction and relaxation of the heart during systole and diastole is regulated by a highly precise and timely activation of specific nodes within the myocardium, composed of specialized cells, the cardiomyocytes. These nodes form part of an intricate electrical conduction system, which activates with each cardiac cycle to synchronize myocardial contractions and ensure efficient blood flow between the heart's four chambers. In a healthy heart, electrical activity originates in the sinoatrial (SA) node, often referred to as the heart's natural pacemaker. The SA node is located in the upper portion of the right atrial wall and generates an action potential that initiates an electrical impulse. This impulse travels through the heart's conduction pathways, inducing coordinated contraction of the myocardium. The components of the heart's electrical conduction system include the SA node, the atrioventricular (AV) node, the bundle of His, and the Purkinje fibers. Figure 2.3 illustrates the conduction system, highlighting these key components.

Once the electrical signal is generated by the SA node, it propagates through the atria, causing atrial contraction. It then reaches the AV node, located at

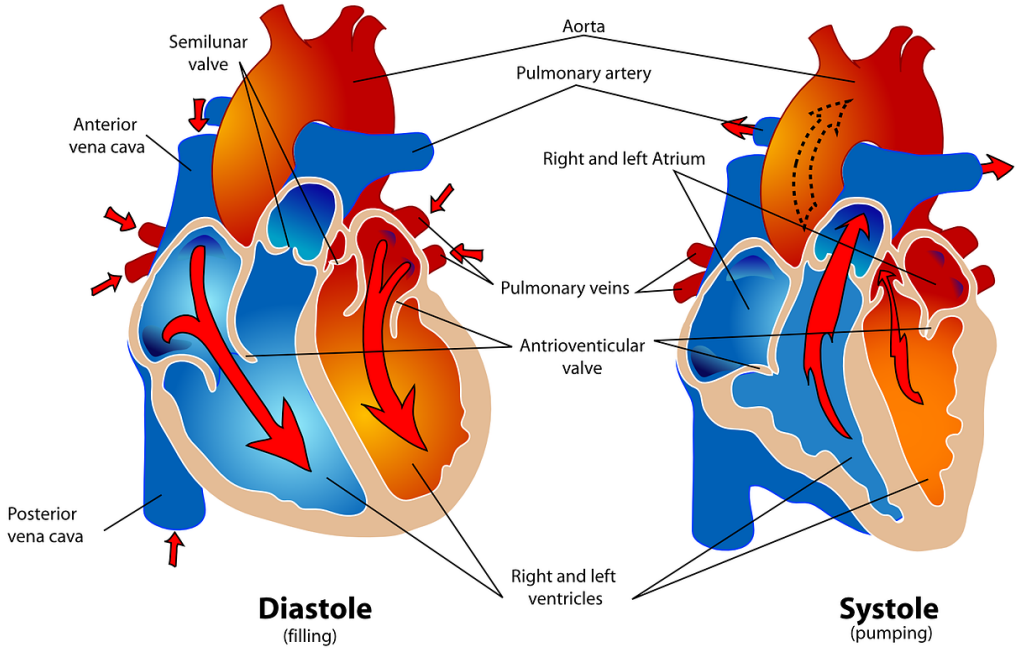

Figure 2.2: Visual representation of the heart's function during diastole (left) and systole (right), illustrating key structures with arrows indicating the direction of blood flow.

the junction of the atria and ventricles, where the impulse slows momentarily to allow for the complete transfer of blood from the atria to the ventricles. The signal then travels through the bundle of His, which divides into the right and left bundle branches, facilitating the conduction of the impulse to the ventricles. From here, the signal spreads via the Purkinje fibers, initiating a coordinated contraction of the ventricles. The distribution of Purkinje fibers across both ventricles ensures that ventricular contraction occurs at multiple initiation points, leading to efficient blood ejection[15, 16, 17].

The entire process of electrical conduction can be visualized in a standard electrocardiogram (ECG). The ECG waveform provides a graphical representation of the electrical activity within a single cardiac cycle. This cycle is reflected in the PQRST complex, a series of distinct deflections corresponding to different stages of cardiac depolarization and repolarization[18], as shown in Figure 2.4. The figure illustrates a typical ECG waveform and highlights the corresponding events per segment during one cardiac cycle. Depolarization refers to the process by which cardiac cells undergo an electrical change that triggers muscle contraction, while repolarization is the subsequent return of the cells to their resting electrical state.

A healthy heart functions under normal sinus rhythm (NSR), in which the electrical impulses originate from the SA node and follow the previously described conduction pathway. In NSR, the timing between consecutive depolarizations of the atria, represented by consistent intervals between P waves, remains constant. The complete cardiac cycle is typically completed in approximately 0.8 seconds[17, 18]. However, there are numerous factors that can impair the proper functioning or conduction of the human heart. A weakened heart muscle, often leading to heart failure, compromises the

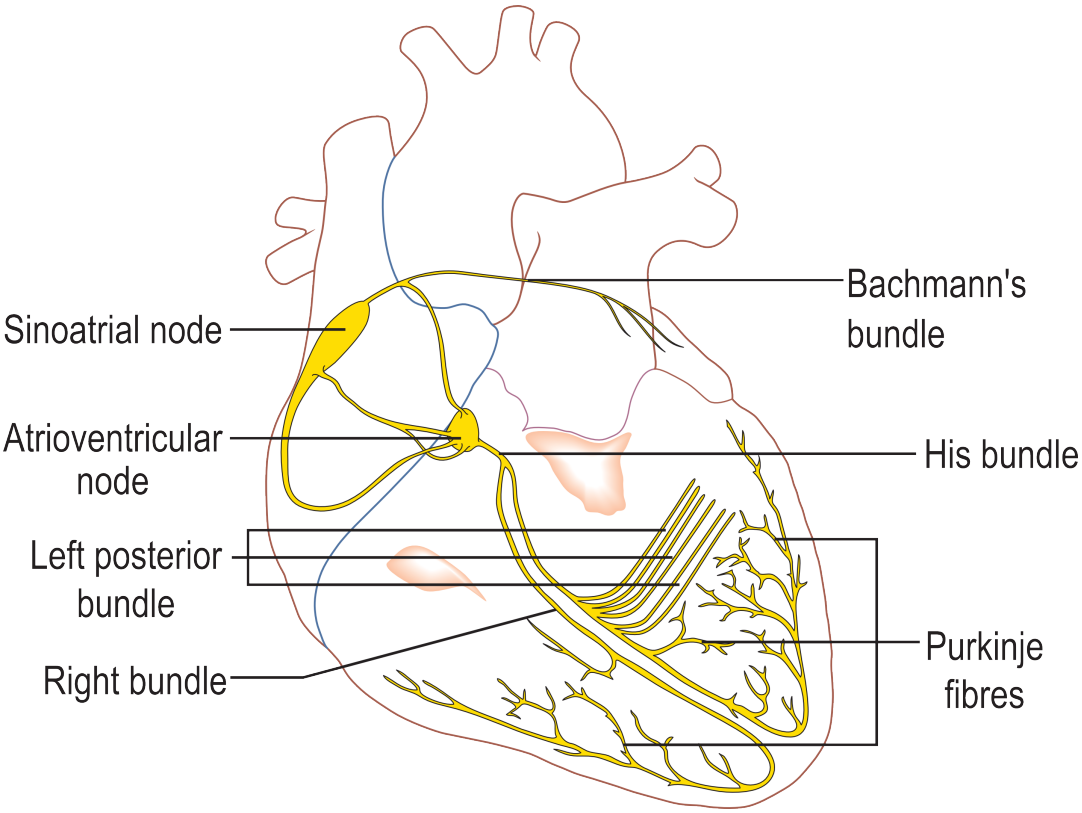

Figure 2.3: Illustration of the electrical conduction system of the human heart, highlighting the key components: the sinoatrial (SA) node, atrioventricular (AV) node, bundle of His, and Purkinje fibers.

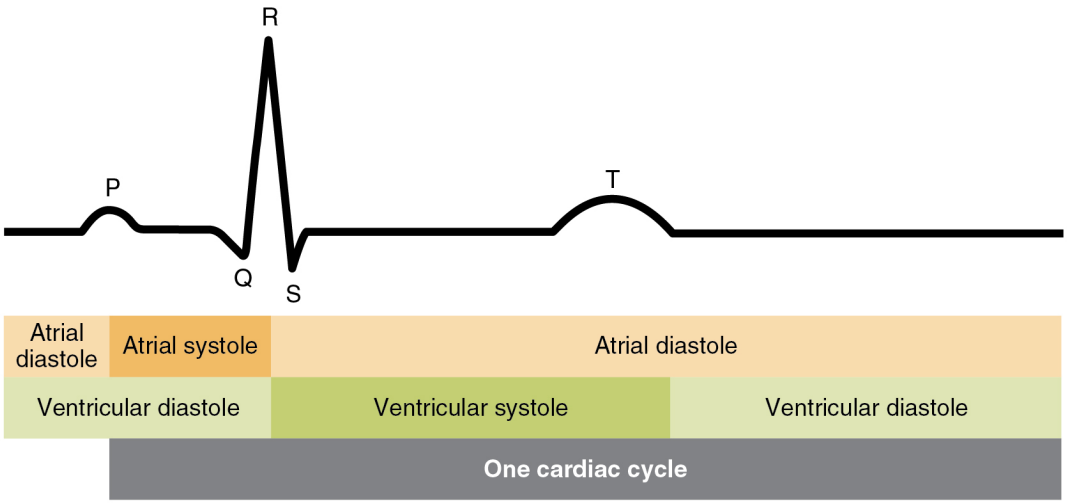

Figure 2.4: Electrocardiogram (ECG) displaying a typical PQRST waveform, with corresponding events during one cardiac cycle.

heart's ability to pump blood efficiently. Valvular diseases can allow for the backflow of blood, disrupting normal circulation, while structural and functional changes in the heart muscle, such as those caused by cardiomyopathies or ischemia, can further hinder cardiac performance. Additionally, arrhythmias—irregular heartbeats resulting from a malfunction in the heart's electrical conduction system—pose significant challenges. To diagnose and plan treatment for these conditions, clinicians commonly rely on a variety of modalities. These include electrocardiography (ECG) for monitoring electrical activity, computed tomography (CT) for structural assessment, magnetic resonance imaging (MRI), and echocardiography using ultrasound for functional evaluation. While these tools are vital, new technologies and advancements in the field of cardiology are continually being developed to enhance diagnosis and treatment.

2.2 Arrhythmias and Their Clinical Importance

An irregular heartbeat—whether it's too fast, too slow, or has an uneven rhythm—is classified as an arrhythmia and any disruption to the heart's conducting system can cause an irregular heartbeat. If the cells producing the electrical signals do not work properly, if those signals do not follow the normal conductive route, or if the heartbeat is initiated from any part of the heart other than the SA node, it can result in an irregular heart beat.

In general, a broad distinction of arrhythmias is based on the heart rate. Heart rates greater than 100 beats per minute fall into the category of tachycardia, while a heart rate of less than 60 beats per minute is considered bradycardia. Depending on the origin of the irregular beat, tachycardia can be further categorized into ventricular arrhythmias, if the origin is below the AV node, or supraventricular arrhythmias (SVTs) (or atrial arrhythmias), if the origin is above the AV node. Another categorization can be made by the duration of the QRS complex on an ECG. Narrow QRS complex tachycardias (less than 120 milliseconds) include sinus tachycardia and atrial tachycardia, while wide QRS complex tachycardias (120 milliseconds or more) are classified into monomorphic and polymorphic types, including ventricular fibrillation[19]. Finally, arrhythmias can be grouped based on their underlying mechanisms into focal arrhythmias, caused by abnormal impulse formation, and reentrant arrhythmias, caused by conduction disturbances that result in circular electrical patterns within the heart[20].

Supraventricular tachycardias affect the upper chambers of the heart and include conditions like atrial fibrillation (AFib), atrial flutter (AFL), and atrial tachycardia (AT). In AFib, the chaotic nature of the signals at the upper atria floods the SA node and leads to an irregular and often very rapid heart rhythm[21]. AFL and AT are both characterized by a faster-than-normal heartbeat but differ in their ECG patterns and origins[22]. On the other hand, ventricular arrhythmias impact the lower chambers of the heart and include ventricular tachycardia (VT), ventricular fibrillation (VFib), and premature ventricular contractions (PVCs). Like AFib, VFib is an irregular heartbeat caused by an electrical malfunction. However, while AFib can persist for years with manageable symptoms, VFib is far more severe, often leading to sudden cardiac arrest within minutes if not treated immediately. PVCs occur

when the electrical signal originates in the ventricles rather than the SA node, resulting in an abnormal heartbeat.

Heart disorders, like coronary artery disease, heart valve disorders and heart failure, are among the most common causes of arrhythmias. Some arrhythmias may be caused by anatomical abnormalities present at birth, while for others no cause can be identified. Changes to the electrical system of the heart can also occur due to aging as well as drug use, prescription or not. Heart muscle may also be damaged by many disease processes such as infarction, hypertension and pulmonary embolism. Symptoms include dizziness, fluttering or pounding sensations, shortness of breath, chest pain, and forceful extra heartbeats. If left untreated, arrhythmias can cause heart, brain, or other organs damage and can lead to life-threatening stroke, heart failure, or cardiac arrest[10, 23, 24].

Arrhythmia treatment is dependent upon the underlying cause. Medicine can treat rapid and irregular heartbeats in many people, but sometimes can not treat an arrhythmia adequately and more invasive procedures are required. The most common alternative for arrhythmia treatment is catheter ablation that uses flexible catheters that reach the heart through the blood vessels. Some catheters have specialized tips to record and locate the arrhythmogenic site, while others can send radiofrequency (RF) waves, extremely cold temperatures, or laser light to scar the area and prevent the abnormal signals from forming. Catheter ablation is an extremely invasive procedure, and accurate location of the ablation site is important to reduce the procedure time and maximize the success of the procedure. Another approach is cardiac resynchronization therapy (CRT), where an implanted device delivers an electrical pulse to depolarize the myocardium, coordinating the function of the left and right ventricles through a pacemaker[25].

Understanding the various types of arrhythmias, their causes, and their symptoms is essential for accurate diagnosis and effective treatment. Precise localization of arrhythmias is critical for selecting the appropriate clinical interventions and customizing treatment plans. Advances in imaging techniques have significantly improved our ability to pinpoint arrhythmogenic sources, facilitating more accurate diagnoses and better patient outcomes.

2.3 Cardiac Imaging Techniques for Arrhythmia Localization

A variety of imaging techniques are used to visualize the heart and pinpoint areas of abnormal electrical activity. In clinical practice, the most commonly used methods include electrocardiography, echocardiography, and intracardiac mapping. Over time, advanced research techniques have emerged to provide more detailed insights into the heart's electromechanical function. Two notable examples, Electrocardiographic Imaging (ECGi) and Electromechanical Wave Imaging (EWI), are explored further in this chapter. Each of these techniques has its own advantages and limitations, which are discussed in detail.

2.3.1 Clinical Modalities

Electrocardiography (ECG)

The electrocardiogram (ECG), first invented in 1903, remains the primary noninvasive tool for diagnosing and localizing cardiac arrhythmias[12]. It is a simple, noninvasive test that can be easily performed on any patient. It works by recording the heart's electrical activity through electrodes placed on specific locations on the body. The ECG captures electrical signals generated by the depolarization and repolarization of myocytes in the atria and ventricles, producing distinct waveforms corresponding to different phases of the cardiac cycle[16].

The standard 12-lead configuration includes nine electrodes placed on the chest and torso, with the remaining three on the right arm, left arm, and left ankle. The recorded electrical signals are displayed as voltage over time and are categorized into three main waveforms: the P wave (representing atrial depolarization), the QRS complex (ventricular depolarization), and the T wave (ventricular repolarization). The P wave typically lasts between 80–100 milliseconds, with the QRS complex following approximately 200 milliseconds after the onset of the P wave and lasting around 100 milliseconds[16, 18, 26].

Clinicians use ECGs to assess (1) conduction disturbances, (2) myocardial infarction or ischemia, (3) atrial or ventricular hypertrophy, and (4) electrolyte imbalances or drug-induced effects. In particular, ECGs are integral in diagnosing arrhythmias, ischemic heart disease, and other cardiac conditions. For patients with infrequent or intermittent symptoms, continuous monitoring through a Holter monitor, which records ECG data over 24 hours or longer, is often employed[12, 16]. Several key intervals and segments in an ECG trace are routinely evaluated by clinicians. These include the P-R interval, QRS duration, S-T segment, and Q-T interval. Prolonged P-R intervals suggest delayed conduction through the atrioventricular (AV) node, while a wide QRS complex points to delays in ventricular conduction through the bundle of His and Purkinje fibers. Abnormalities in the S-T segment, such as elevation or depression, can indicate conditions like myocardial infarction, coronary artery disease, or pericarditis. Additionally, a prolonged Q-T interval suggests delayed repolarization of the cardiomyocytes[16, 26].

Figure 2.5 illustrates five common ECG irregularities. In cases of second-degree (partial) block (Figure 2.5a), which occurs when some but not all signals from the atria fail to reach the ventricles, the P waves are intermittently not followed by QRS complexes, indicating a disruption in signal transmission between the atria and ventricles. Atrial fibrillation (Figure 2.5b) is characterized by chaotic electrical activity prior to the QRS complex, resulting in irregular intervals between ventricular contractions. Ventricular tachycardia (Figure 2.5c) features an abnormal QRS complex shape, reflecting a rapid, uncoordinated ventricular rhythm. In ventricular fibrillation (Figure 2.5d), the absence of organized electrical activity leads to ineffective ventricular contractions and poses a life-threatening risk. Finally, third-degree block (Figure 2.5e) shows complete dissociation between P waves and QRS complexes, where the SA node's signals are blocked at the AV node, causing independent atrial and ventricular rhythms. Distinguishing between the different

wave patterns on the ECG is crucial for diagnosing and differentiating various cardiac arrhythmias.

However, ECGs are limited in that they primarily detect electrical disturbances and cannot directly identify structural abnormalities such as arterial blockages and do not always reveal the location origin. Additionally, ECG interpretation is subject to variability depending on the quality of the recorded data and the experience of the practitioner analyzing it. Because the electrodes are placed externally, minimizing patient movement is critical to reduce signal interference from other sources, such as skeletal muscle activity. External factors, like obesity, can further complicate the interpretation of ECGs[27]. To assist in arrhythmia localization, various algorithms have been developed to analyze ECG data and provide clinical insights[16]. While these algorithms demonstrate high accuracy (90-93%)[28, 29, 30, 31] for detecting accessory pathways and focal atrial tachycardias (ATs), their effectiveness is lower for ectopic ventricular rhythms, with accuracies ranging from 72-82%[32, 33, 34]. Despite these advancements, algorithmic performance tends to be less reliable in real-world clinical practice due to a variety of external and patient-specific factors[35].

Echocardiography

Echocardiography is a widely used non-invasive imaging modality that utilizes ultrasound technology to assess cardiac structure and function. First introduced for cardiovascular diagnosis by Edler and Hertz in 1954, it has since undergone significant advancements and is now an essential tool in the diagnosis, management, and follow-up of patients with various heart diseases. Compared to other imaging modalities, transthoracic echocardiography (TTE) remains the most commonly employed due to its non-invasive nature, absence of risks or side effects, and ability to provide real-time imaging of the heart[36].

The fundamental component of an echocardiography system is the transducer, which both transmits and receives ultrasound waves. These waves propagate through the body, interact with various cardiac structures, and return to the transducer, which are then analyzed to generate images. These images, known as echocardiograms (or simply "echos"), can be displayed in two-dimensional (2D) or three-dimensional (3D) formats depending on the mode of imaging utilized. Several imaging modes exist, each offering unique advantages. A-mode (Amplitude mode) displays the amplitude of returning echoes, B-mode (Brightness mode) produces a 2D cross-sectional image of the heart, while M-mode (Motion mode) visualizes the motion of heart structures over time, providing valuable temporal data on valve movement and chamber dynamics. Strain imaging is used to assess myocardial deformation, offering insights into regional heart function. Contrast echocardiography uses contrast agents to enhance visualization of cardiac structures, particularly when traditional echocardiography produces suboptimal images.

Cardiac sonographers or trained physicians typically perform echocardiography using phased-array transducers that operate at frequencies ranging from 2 to 15 megahertz (MHz). These transducers are positioned at specific anatomical locations on the chest or abdomen, with different angles and

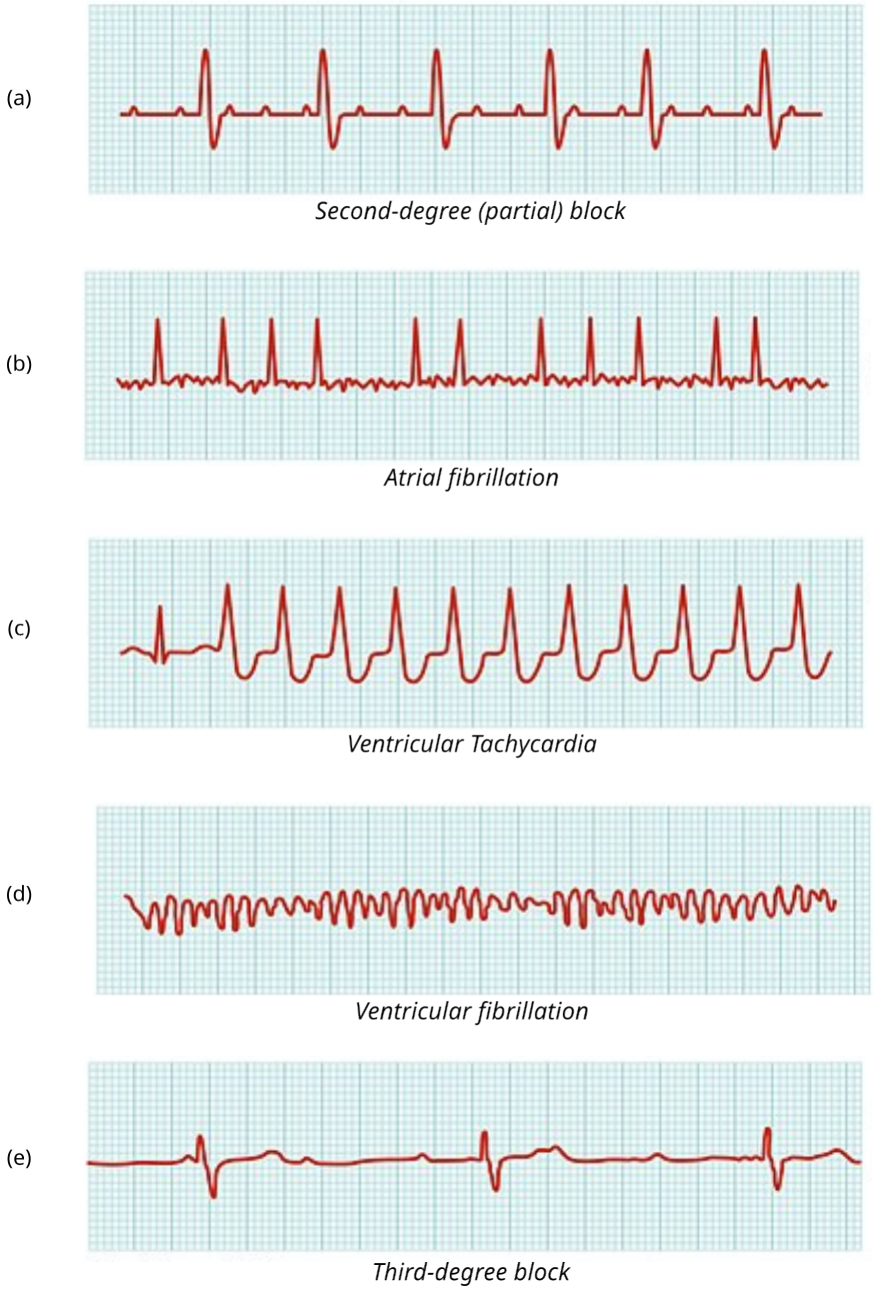

Figure 2.5: Comparison of five abnormal ECG patterns. (a) Second-degree (partial) block, showing P waves not consistently followed by QRS and T waves. (b) Atrial fibrillation, with abnormal electrical activity and increased frequency between QRS complexes. (c) Ventricular tachycardia, characterized by an unusual QRS complex shape. (d) Ventricular fibrillation, displaying a complete lack of normal electrical activity. (e) Third-degree block, where P waves are not followed by QRS complexes, indicating that some SA node impulses do not reach the AV node.

orientations used to capture various imaging planes. Figure 2.6 illustrates the placement of the transducer on a human subject during the imaging process, as well as an example B-mode echocardiographic image showing key cardiac structures such as the LA, the LV, the RA, and the RV.

Echocardiography can be broadly categorized into three types, each offering specific insights into cardiac function and anatomy. Transthoracic Echocardiography (TTE) is the most commonly performed type of echocardiography. It is a non-invasive procedure in which the ultrasound transducer is placed on the chest wall to obtain real-time images of the heart. TTE provides critical information regarding heart size, function, valve abnormalities, and the presence of pericardial effusion. The various views obtained during a TTE exam allow for a thorough assessment of different cardiac structures, such as the left and right ventricles, atria, and valves. Its ease of use, low cost, and lack of patient risk make it ideal for routine clinical evaluation.

Transesophageal Echocardiography (TEE) involves placing a specialized ultrasound probe into the esophagus to obtain clearer images of the heart, particularly the posterior structures. Figure 2.7a illustrates the TEE procedure, where the probe is positioned near the posterior heart wall for optimal imaging. This technique is especially valuable when TTE images are suboptimal, such as in patients with obesity or lung disease. TEE provides detailed imaging of the atria, valves, and thoracic aorta, making it useful in detecting clots, assessing valve pathologies, and guiding interventional procedures. However, TEE is more invasive than TTE and requires patient sedation, which limits its routine use to specific clinical scenarios.

Intracardiac Echocardiography (ICE) is a specialized echocardiographic technique in which an ultrasound probe is inserted into the heart via a catheter. Figure 2.7b depicts the ICE procedure, showing the probe being introduced through the inferior vena cava (IVC) to provide real-time internal imaging during catheter-based interventions, such as atrial septal defect closure or ablation therapy for arrhythmias. ICE offers high-resolution images and precise guidance for procedures that require transseptal punctures or access to the left atrium[36, 37].

Echocardiography is useful for the management of a wide range of cardiovascular conditions and allows for the assessment of both anatomical and functional aspects of the heart. Key clinical applications include evaluation of cardiac structure like wall thickness, chamber size, and the presence of congenital defects. It can also assess valve function and is employed pre- and post-operative evaluations of cardiac surgeries. It is also useful for left and right ventricular function assessment, detection of pericardial conditions and guidance of catheter-based interventions during surgery[38]. This information is vital not only for diagnosis but also for surveillance, management, and post-procedural assessment of arrhythmias[36, 39].

Recent advancements in three-dimensional echocardiography (3D echo) have further enhanced the capabilities of echocardiography by providing more accurate assessments of heart function and volume, as well as improved visualization of complex structures, such as the mitral valve and left atrium. This technology allows for more reproducible measurements compared to 2D echocardiography and is increasingly used in surgical planning and interventions. However, 3D echo requires greater technical expertise and is not

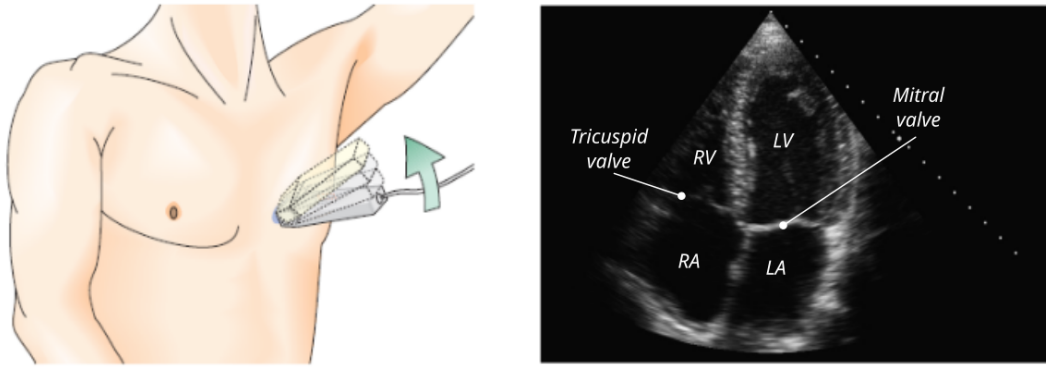

Figure 2.6: (a) Illustration of a human subject lying down with an echocardiography transducer placed on the chest, demonstrating the transducer's movement during the imaging process. (b) Example B-mode echocardiographic image displaying key cardiac structures, including the left atrium (LA), left ventricle (LV), right atrium (RA), and right ventricle (RV).

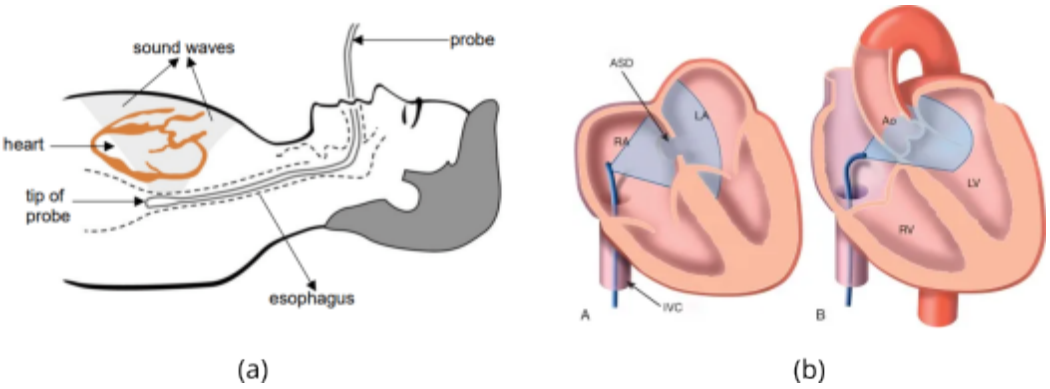

Figure 2.7: (a) Diagram illustrating the procedure of transesophageal echocardiography, with the probe inserted through the esophagus to position the tip near the posterior heart wall for imaging. (b) Diagram showing intracardiac mapping, where the probe is introduced through the inferior vena cava (IVC) and positioned inside the heart, enabling internal scanning of cardiac structures.

as widely available as standard 2D imaging[40].

Overal, echocardiography, and especially TTE, provides real-time images from the heart. Images can be obtained quickly with the least patient discomfort. It is designed to be portable and used as a bedside imaging modality. It gives comprehensive information regarding the cardiac structure and function and the hemodynamic flow at a relatively inexpensive cost. Despite its many advantages, echocardiography image assessment can be affected by patient factors such as obesity[41], obstructive lung disease, or an inability to hold their breath, which can lead to suboptimal visualization of cardiac structures. Additionally, echocardiography is highly operator-dependent, requiring the sonographer to have extensive knowledge of instrumentation, anatomy, and pathology to obtain accurate and diagnostically useful images. Artifacts may also arise due to natural barriers such as the rib cage, further complicating image acquisition[37, 42].

Intracardiac Mapping

Intracardiac mapping is the foundation in the diagnosis and treatment of cardiac arrhythmias. This technique involves the use of one or more catheters with specialized tips, which are inserted into the heart chambers to collect data directly from the myocardial walls. These catheters are typically equipped with electrodes that can record electrical activity, allowing for precise mapping of the heart's conduction system. Intracardiac mapping is fundamental in guiding ablation therapies, as it provides critical information needed to differentiate between healthy myocardium and scar tissue. Furthermore, it enables the creation of 3D activation maps that localize areas of abnormal electrical activity, which is essential in identifying arrhythmogenic regions during catheter ablation procedures. Catheter-based mapping can be classified into two main types: contact and non-contact mapping. In contact mapping, the catheter makes direct contact with the heart walls, providing highly localized data. In contrast, non-contact mapping allows for the acquisition of electrograms without direct contact, using methods such as inverse algorithms to reconstruct the electrical activity. Both techniques have demonstrated considerable value in localizing arrhythmias, with multiple catheters often deployed simultaneously to compare signals from different sites and improve accuracy in identifying the origins of arrhythmic activity. This capability of simultaneous data collection is particularly useful in pinpointing the precise locations of abnormal electrical conduction[26, 43, 44].

Intracardiac mapping techniques are often tailored to the specific type of arrhythmia—whether focal or reentrant—and the pacing maneuvers used during the procedure. In activation sequence mapping, the arrhythmogenic site is identified by timing the onset of successive electrograms recorded from the catheter, relative to a reference signal. For focal arrhythmias, the site exhibiting the earliest electrogram is determined to be the origin of the abnormal rhythm. Pace mapping is another technique, particularly useful for focal tachycardias. It is based on the principle that stimulating an arrhythmogenic site will produce a 12-lead ECG identical to spontaneous arrhythmia. This technique involves pacing different regions of the heart to match the ECG patterns observed during the arrhythmia, thereby localizing the arrhythmic source. For reentrant arrhythmias, such as atrial flutter, entrainment mapping is widely used. This technique involves pacing maneuvers to "capture" the tachycardia circuit, allowing clinicians to determine whether the arrhythmia is part of a reentrant loop. This is critical for diagnosing and treating reentrant arrhythmias, where the abnormal rhythm circulates through a specific pathway[26, 45, 46].

Modern advances in intracardiac mapping have led to the development of electroanatomic mapping (EAM) systems, which combine both electrical and anatomical data to generate detailed 3D models of the heart. These systems localize catheters in real time and track their movements to create accurate 3D geometry of the heart chambers during a procedure. Some of the most widely used commercial systems include Carto, EnSite, and Rhythmia, each utilizing different techniques for catheter localization[26, 46, 47]. Additionally, electrograms recorded from the heart's surface can be used in inverse algorithms to reconstruct 3D potential maps. The prerequisite for this process is the availability of geometrical data, which can be obtained through

imaging modalities like CT, MRI, or intracardiac echocardiography (ICE)[44]. ICE is a complementary technique that differs from traditional electrogram-based mapping. Instead of using electrical data, ICE relies on an ultrasound catheter to produce real-time anatomical images of the heart. ICE is especially valuable during catheter ablation procedures, improving both safety and efficacy by providing real-time feedback on catheter placement. While ICE primarily focuses on anatomical imaging, it can be used in conjunction with intracardiac mapping to enhance procedural outcomes.

EAM systems have become a vital tool in the precise diagnosis and treatment of tachycardias, particularly in guiding catheter ablation procedures. One of the primary benefits of EAM is its ability to localize arrhythmias with similar success rates to traditional methods, but with reduced radiation exposure and procedure time, making it particularly valuable for managing a variety of rhythm abnormalities[48, 49, 50]. Despite its advantages, intracardiac mapping remains a highly invasive procedure. The insertion of catheters into the heart carries inherent risks, including infection, bleeding, and potential damage to the cardiac tissue. Additionally, the specialized equipment and expertise required to perform EAM come with substantial costs, limiting its availability in some healthcare settings. Mapping complex arrhythmias can also be time-intensive, which may prolong the procedure and increase patient discomfort. While EAM systems provide critical information that improves the precision of arrhythmia localization and treatment, they should not be used in isolation. Relying solely on EAM could result in inaccurate diagnoses or incorrect localization of arrhythmic sites. In some cases, this may lead to the creation of ineffective or misleading activation maps. Therefore, EAM should be integrated with other diagnostic modalities and clinical insights to ensure accurate mapping and optimal patient outcomes[51].

2.3.2 Research Techniques

Electrocardiographic Imaging (ECGi)

Electrocardiographic imaging (ECGi) was developed to overcome the limitations of conventional ECG techniques, providing a more comprehensive assessment of cardiac electrical activity. As a non-invasive, multi-lead, imaging modality, ECGi significantly improves upon the standard 12-lead ECG by offering a 3D representation of the heart, along with activation maps that display the timing and location of electrical events. This additional detail enhances the diagnostic utility of ECGi, making it particularly valuable in the preoperative planning phase for more invasive procedures such as electrophysiology studies. By providing detailed activation maps, ECGi can accurately pinpoint the origin of arrhythmias like tachycardia, thus guiding the procedure and improving outcomes. Moreover, ECGi is increasingly employed in patients undergoing cardiac resynchronization therapy (CRT) to assess treatment progression, monitor the electrophysiological response, and assist in selecting candidates and optimizing lead placement[52, 53, 54, 55].

Building on the foundations of the traditional 12-lead ECG, ECGi uses multi- electrode arrays placed across the body or chest, combined with 3D imaging techniques such as computed tomography (CT) or magnetic resonance imaging (MRI), to reconstruct an electroanatomic map of the heart

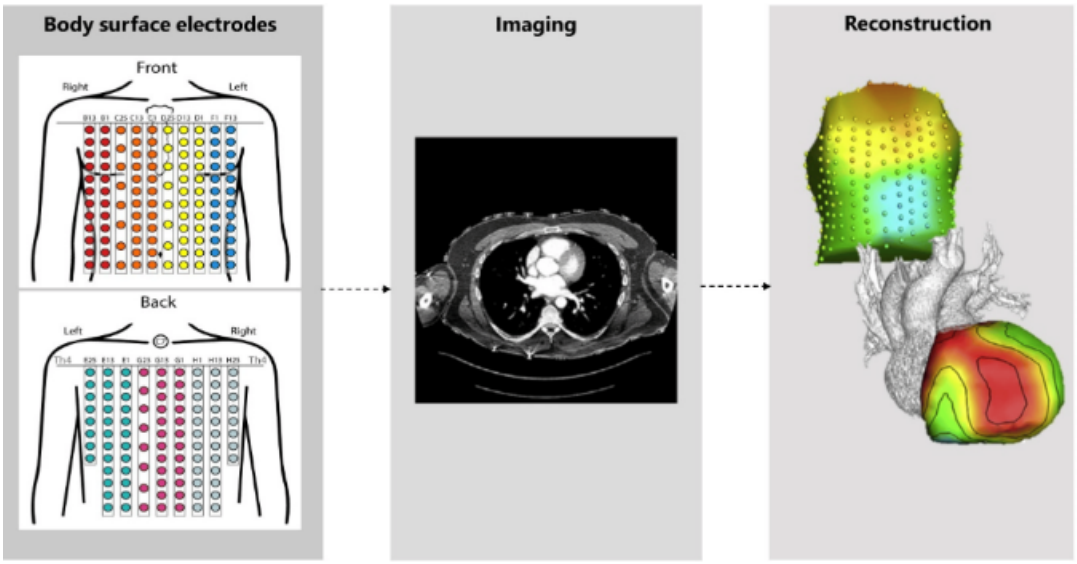

Figure 2.8: Overview of the electrocardiographic imaging (ECGi) procedure. ECGi begins with recording body surface electrocardiograms (ECGs) using 256 electrodes. Cardiac computed tomography (CT) is then employed to create a patient-specific heart and torso geometry. By combining these data, epicardial potentials are mathematically reconstructed.

(Figure 2.8). This technique is based on the principle that the heart's electrical activity propagates through the torso, which acts as a passive conductor. By recording electrical signals from the body surface, clinicians can estimate the electrical potentials on the heart's surface, thus reconstructing the epicardial electrical activity from non-invasive measurements. The reconstruction process relies on anatomical data derived from CT or MRI scans, and sophisticated computational algorithms are used to solve the inverse problem of electrocardiography—i.e., determining the cardiac electrical source responsible for the observed body-surface potentials. Several models have been developed to adapt ECGi to different diagnostic requirements. For example, the Equivalent Double Layer (EDL) model can represent electrical activity in all four cardiac chambers, including the epicardium and endocardium, while 3D Cardiac Electrical Imaging is primarily focused on the ventricles, offering 3D estimates of electrical activation timing throughout the myocardium [12, 16, 53].

ECGi has been extensively validated through multiple studies involving both animal and human models. It has been shown to accurately capture cardiac electrical activity during various conditions, including normal sinus rhythm, ventricular pacing, and atrial flutter. Unlike standard ECG, ECGi can provide detailed visualizations of both activation and repolarization patterns[56, 57, 58, 59]. Reported reconstructions offer a spatial accuracy of approximately 10 mm, providing precise localization of abnormal electrical sources[52, 54].

Despite its clinical benefits, ECGi presents certain challenges. The method is highly dependent on the clinical application in question, as different parameters must be optimized for each case. Additionally, the procedure can be time-consuming, requiring specialized expertise not only to perform the imaging but also to interpret the results[55]. Electrode placement, a critical

factor in the accuracy of ECGi, is often labor-intensive and may extend procedure times. While some systems utilize pre-constructed electrode vests, the number of electrodes used can vary significantly, with some manufacturers using up to 300 electrodes to ensure adequate body-surface coverage[60]. Furthermore, the need for CT or MRI imaging, particularly the exposure to radiation in the case of CT, introduces further complexity and limits ECGi's use to well-equipped clinical settings. The development of faster, more user-friendly systems and the integration of ECGi with other imaging modalities are crucial steps towards broader adoption and improved accessibility.

Electromechanical Wave Imaging (EWI)

Electromechanical Wave Imaging (EWI) is an ultrasound-based modality capable of non-invasively generating two-dimensional maps of the heart's electrical activation in real time. EWI functions by tracking the electromechanical activity of the myocardium, specifically the mechanical deformations that occur as a result of electrical activation during the cardiac cycle. These mechanical waves, which follow the propagation of electrical signals throughout the myocardium and cardiac chambers, can be captured to determine the timing of electromechanical activation. This activation is defined as the moment when the myocardial tissue transitions from a relaxed to a contracted state. By capturing this event at each point along the myocardium, a detailed map of the electrical activation wave propagation can be constructed[14, 61].

Full 3D EWI can capture the entire heart in three dimensions in a single heartbeat, providing a comprehensive picture of the electromechanical activation however its lower spatial resolution reduces its accuracy in localizing arrhythmias, making it spatially less accurate than 2D EWI. Furthermore, to achieve similar temporal resolution as 2D EWI—necessary for accurately capturing the electromechanical wave—full 3D EWI requires four Vantage 256 ultrasound systems, which drastically increases both cost and operational complexity. These constraints make bedside use and widespread clinical adoption challenging. Given these limitations, 3D-rendered EWI has become a practical alternative for visualizing the complex 3D activation patterns. In 3D-rendered EWI, 2D maps are registered and rendered in space to create a 3D map, depicting the propagation of the electromechanical wave in a clear and accessible format[62]. This approach combines the higher spatial resolution of 2D EWI with the spatial representation of 3D, making it both practical and effective for clinical use.

The duration of the electromechanical wave is approximately 60 to 100 milliseconds, necessitating the use of echocardiography imaging at very high frame rates to accurately capture the myocardial activation. EWI achieves the required spatial and temporal resolution by significantly increasing the acquisition frequency during standard transthoracic echocardiography. High-frame rate imaging data are then correlated with the patient's electrocardiogram (ECG) signals to produce precise activation maps for each myocardial wall segment. The radiofrequency data acquired are processed alongside the ECG data to extract wall displacements, strain patterns, and ultimately, the electromechanical activation maps. This process is computationally efficient,

requiring only an ultrasound scanner and a standard computer system, with data processing times of approximately 10 minutes[14].

EWI offers several key advantages, including real-time feedback, no radiation, and non-invasiveness, while also providing reproducible and angle-independent electromechanical maps across multiple cardiac cycles, acquisitions, and echocardiography views[63]. Multiple studies in both canine models and human subjects have demonstrated EWI's capability to accurately characterize electromechanical activation in all four cardiac chambers, both during pacing and normal sinus rhythm[64, 65]. Moreover, EWI has shown sensitivity to detecting and mapping early-stage ischemia and assessing myocardial conduction properties, making it a valuable tool for tracking ischemic onset and disease progression without the need for invasive procedures[66]. Additionally, EWI has demonstrated potential in evaluating cardiac resynchronization therapy (CRT) patients, providing crucial insights into ventricular synchronization[67].

EWI also has significant clinical utility in the planning of ablation procedures, offering improved accuracy in identifying arrhythmia origins compared to traditional ECG techniques, even in cases where ECGi may fall short[68]. EWI can map both single source[69, 70] and chaotic arrhythmias [71]. Specifically, it has shown enhanced precision in localizing arrhythmias such as atrial tachycardia (AT), atrial flutter (AFL), premature ventricular complexes (PVC), and accessory pathways (AP) in Wolff-Parkinson-White syndrome, prior to catheter ablation[35]. Figure 2.9 provides a detailed example of EWI's effectiveness in localizing arrhythmias before and after a successful RF ablation. In Figure 2.9a, the EWI isochrones of a patient's ventricles before ablation show the earliest activation in the lateral LV, marked in red. After the catheter ablation, as shown in Figure 2.9b, the earliest activation has shifted to the septum, indicating a successful modification of the abnormal conduction pathway. The 3D-rendered EWI isochrones further highlight the precise location of the arrhythmia origin and the normalization of ventricular activation post-ablation. This makes EWI a promising tool for the non-invasive diagnosis, treatment planning, and follow-up of patients with arrhythmias or those undergoing pacing therapies, offering a low-cost, real-time solution even in settings with limited time or resources.

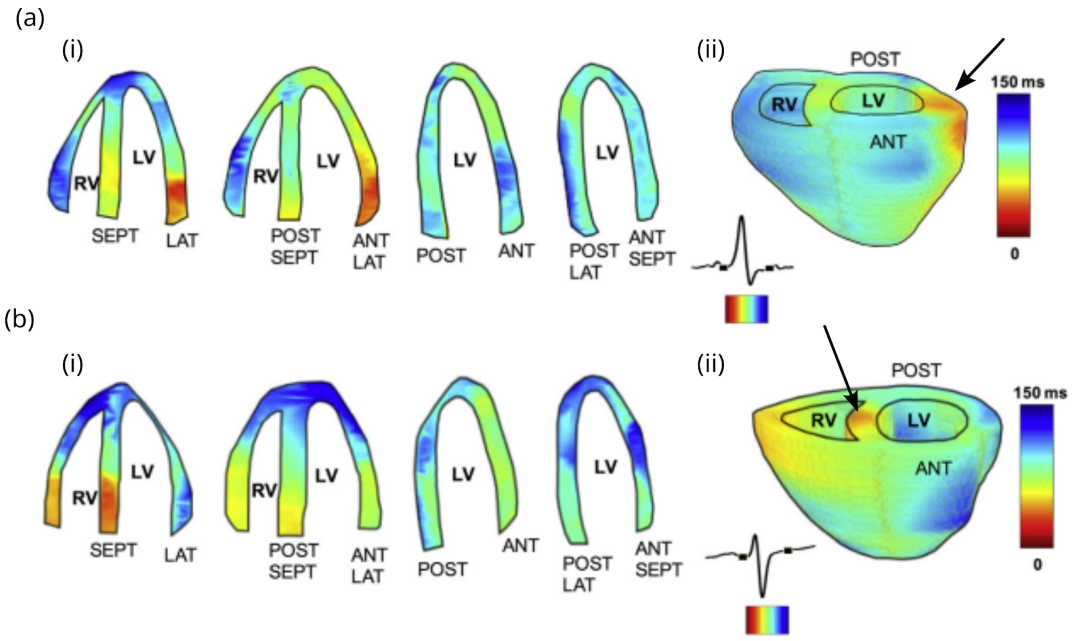

Figure 2.9: EWI isochrones of a patient before and after successful RF ablation. Red indicates the earliest activation and blue the latest for all isochrones. (a) (i) Four 2D EWI isochrones of the ventricles before catheter ablation, showing the earliest activation in the lateral (LAT) LV. (ii) 3D-rendered EWI isochrone before ablation with an arrow indicating the earliest activation site. (b) (i) Four 2D EWI isochrones of the ventricles after catheter ablation, showing the earliest activation now in the septum. (ii) 3D-rendered EWI isochrone after ablation showing normal ventricular activation, with an arrow marking the earliest activation site.

However, like all echocardiography-based techniques, EWI is subject to certain limitations. Image quality is highly dependent on patient-specific factors such as body mass index (BMI), breath-holding ability, and patient movement during image acquisition. The sonographer's expertise also plays a critical role in obtaining accurate images, while anatomical obstacles such as the lungs and ribs can impede data collection. In the generation of 3D activation maps, there are additional challenges, including the number of transthoracic echocardiographic (TTE) views available and maintaining consistent transducer placement on the patient's chest during imaging[62]. Ongoing research aims to further refine EWI technology, with efforts focused on improving its accuracy and predictive capabilities. Future developments hold promise for EWI's role in personalized arrhythmia treatments, with potential adoption in clinical settings as an integral part of non-invasive arrhythmia diagnosis and management. The continued evolution of EWI may lead to more precise and tailored interventions for individual patients, advancing the field of cardiac electrophysiology.

Chapter 3

3D Rendering of Electromechanical Wave Imaging

3.1 Introduction

The development of accurate and efficient three-dimensional (3D) rendering algorithms is critical to improving Electromechanical Wave Imaging (EWI) as a clinical tool for cardiac diagnosis and treatment. The current algorithm for generating 3D electromechanical activation maps, while functional, is limited in several key areas. It works only with a small set of predefined echocardiographic views, specifically four apical views centered around the left ventricle (LV), and requires manual manipulation of code for each step of the process. The dependence on predefined views, combined with the complexity of manual user input, can hinder the broader clinical application of EWI, especially for non-technical users. As a result, current workflows are both time-intensive and prone to error, creating significant barriers to its effective use in real-time clinical settings.

This chapter outlines the efforts made to overcome these limitations by significantly improving the 3D rendering algorithm. The goal of these advancements is to create a user-friendly and accessible platform that can be more easily adopted in clinical environments. Specifically, the enhanced algorithm automates many previously manual processes, making it simpler for non-specialist users to operate the software. Additionally, it introduces view-agnostic capabilities that allow for flexible rendering of any combination of apical views focused on the left ventricle, thus expanding the range of usable data and improving spatial coverage, particularly in previously undersampled areas. These upgrades are expected to reduce computation times and streamline the entire workflow, making the system more robust, reliable, and practical for real-time cardiac imaging.

The methodology section of this chapter delves into the principles behind these improvements. It begins by providing an in-depth overview of echocardiography, focusing on transthoracic echocardiography (TTE) and the physical principles it is based upon. This section also reviews the imaging planes and echocardiographic views relevant to EWI, to help with the later detailed explanation of how EWI functions as a non-invasive tool for tracking electromechanical activity within the myocardium. Following that, a series of models demonstrating the improved capabilities of the new algorithm are presented focusing on showcasing the system's ability to render 3D activation maps from a broader range of apical views, providing greater

flexibility and data coverage. In addition, comparative metrics between the original and new algorithms are highlighted to quantify improvements in accuracy, rendering times, and data representation.

Finally, the outcomes of these advancements, considering their clinical implications are discussed exploring the strengths and potential limitations of the new algorithm, as well as its future applications in both research and clinical practice.

3.2 In-depth overview of Transthoracic Echocardiography

Echocardiography encompasses several methodologies, each offering unique insights into cardiac anatomy and function. However, this thesis will not delve into all modalities and techniques. Instead, it will focus specifically on transthoracic echocardiography (TTE) using B-mode imaging. TTE is a widely used, non-invasive technique that provides valuable diagnostic information by utilizing different imaging windows to assess the heart. Each window reveals distinct cardiac structures, making it critical for a comprehensive evaluation of various cardiac conditions.

In this chapter, a detailed overview of TTE will be presented, starting with foundational principles of echocardiography, covering the relevant physics and the key imaging planes used to visualize the heart. This will be followed by an overview of the most commonly used acquisition planes in TTE, with emphasis on views most relevant to the objectives of this thesis. This understanding of TTE image acquisition and generation will serve as an essential foundation for comprehending the methodology behind Electromechanical Wave Imaging (EWI), the focus of this research.

3.2.1 Physics Behind Echocardiography

Sound is a form of energy transmitted through a medium via pressure waves. Ultrasound, which refers to sound waves with frequencies exceeding 15–20 kHz, is inaudible to humans but valuable for imaging applications. These waves are characterized by several key parameters: wavelength (λ), which is the distance a wave travels in one cycle; amplitude (A), which describes the maximum displacement of the wave; frequency (f), the number of cycles per second (Hertz, Hz); intensity (I), representing the rate of energy flow through the medium; and period (T), the time required for a complete wave cycle. The velocity of these sound waves, V, is dependent on the medium they pass through. For example, ultrasound waves travel at 330 m/s in air and 1540 m/s in soft tissue[72]. The fundamental relationship governing wave propagation is:

$$V = f \times \lambda$$

Given that the propagation velocity in a specific medium is constant, an increase in frequency results in a decrease in wavelength and, consequently, shallower penetration into tissues. Conversely, lower frequencies correspond to greater penetration but at the cost of reduced resolution (Figure 3.1).

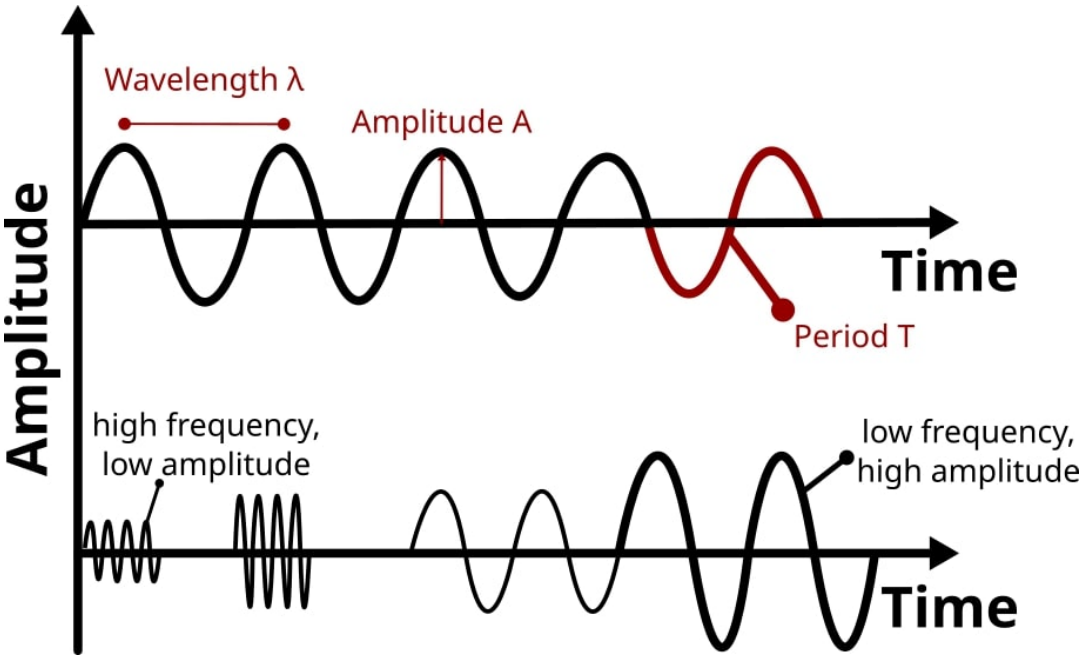

Figure 3.1: Diagram of a sound wave showing key characteristics: amplitude (A), period (T), frequency (f), and wavelength (λ).

As a wave, ultrasound can be directed, reflected, refracted, and absorbed when it encounters different tissues such as skin, chest wall, lung, pericardium, and blood. When ultrasound strikes a boundary between two mediums, part of the wave is reflected, while the remaining portion continues through the medium. Scattering occurs when the wave encounters a boundary between tissues of varying stiffness, resulting in the random dispersion of a small portion of the beam. If the wave crosses into a medium with differing stiffness, refraction alters its direction. Some of the wave's energy is also absorbed, converting acoustic energy into thermal energy[37, 73]. These interactions cause the sound wave to lose both intensity and amplitude, a phenomenon known as attenuation.

The ultrasound probe, or phased-array transducer, is the device that generates and receives these waves. It contains piezoelectric crystal elements (PZE), which convert electrical signals into mechanical pressure waves. The term "phased" refers to the controlled excitation of PZE elements[37, 74, 75]. In clinical use, the transducer alternates between producing and receiving ultrasound waves, as it cannot perform both functions simultaneously. As the waves propagate through the body, interactions with various structures (such as bones and organs) produce reflected waves, or echoes, that return to the transducer. These echoes provide the data necessary to create two-dimensional ultrasound images using the pulse-echo method. By analyzing the round-trip times and amplitudes of these echoes, clinicians can reconstruct anatomical images[37, 73]. When waves encounter rough or irregular surfaces, they are scattered in various directions, producing weaker signals known as backscatter. Not all backscatter returns to the transducer for image generation; however, it contributes to the granular patterns called speckles, which can be tracked throughout the imaging cycle. Speckle tracking forms

the basis for Speckle Tracking Echocardiography (STE), which is used to evaluate the motion of cardiac tissues[37, 76].

In brightness mode (B-mode) imaging, the amplitudes of returning echoes are analyzed to create points of varying brightness along the ultrasound beam's path. These points are used to construct a 2D image by combining multiple B-mode lines. The appearance of these images is influenced by the interaction between ultrasound waves and tissue boundaries. When the beam strikes a smooth boundary perpendicularly, strong echoes are generated and appear as bright, highly reflective structures. However, when irregular surfaces are encountered, weaker echoes with lower amplitudes appear as shades of gray. Structures that absorb most of the ultrasound beam, such as fluid-filled areas, appear echo-free (black) on B-mode images[73].

The wavelength and frequency of the incident echoes influence both the depth of penetration and the image quality. Amplitude, on the other hand, determines the brightness of the structures visible on B-mode imaging. When the ultrasound beam encounters a smooth tissue boundary or interface at a 90-degree angle, most of the waves are reflected directly back to the transducer. This results in strong echoes, which appear as bright, highly reflective structures on the image. In contrast, when the ultrasound beam hits rough or irregular surfaces, it scatters in various directions, causing weaker echoes and producing lower-amplitude signals. These weaker echoes manifest as shades of gray on the B-mode image. Structures that absorb most of the ultrasound beams, generating minimal or no reflections, appear as echo-free (black) regions on the display. The appearance of echoes is also influenced by the travel path of the ultrasound beam. Echoes from surfaces that are closer to the transducer reflect back sooner, before substantial energy is lost, and therefore appear brighter on the image. Echoes returning from deeper tissue levels arrive later and are therefore weaker, resulting in darker areas on the echocardiogram. Furthermore, there is a relationship between the velocity of the ultrasound beam and the scaling of the image. A higher velocity of the beam tends to produce an enlarged image on the display[73].

Considering these principles and the interplay between velocity, frequency, and wavelength, it becomes evident how ultrasound waves of lower frequency penetrate tissues more deeply but offer lower resolution due to longer wavelengths. This allows them to travel greater distances with less attenuation but compromises their ability to distinguish small structures, resulting in lower resolution images. On the other hand, higher frequency waves have shorter wavelengths, providing greater resolution but at the cost of limited depth penetration due to quicker energy loss[77]. This differentiation between bright and gray areas forms the fundamental basis of B-mode echocardiography.

3.2.2 Imaging Planes in TTE

The heart is composed of four chambers: the left and right atria and ventricles, separated by the septum. Although the two sides share structural similarities, the heart is not a fully symmetrical organ. Furthermore, the slight rotation of the apex, the lower portion of the heart, towards the left creates an angular disparity between the heart's major axis, defined by the long axis of

the left ventricle (LV), and the body's longitudinal axis. In most adults, this angle is approximately 60° (Figure 3.2a,b). The long axis of the LV serves as a critical anatomical reference point for defining standard echocardiographic imaging planes.

With the cardiac long axis defined, three principal imaging planes are identified around the heart: the cardiac short axis (SAX), the cardiac long axis (LAX), and the four-chamber (4C) view, also referred to as the apical view (Figure 3.2c). In addition to these imaging planes, the transducer can be placed in different anatomical positions: parasternal (P), apical (A), subcostal (SC), or from the suprasternal notch (SSN) (Figure 3.2d). Each echocardiographic view is described based on three key components: the transducer's position, the imaging plane, and the structures or regions being visualized. For example, views such as the apical four-chamber (A4C) or apical two-chamber (A2C) are commonly used for comprehensive evaluation of the heart's anatomy.

Echocardiographic images are obtained by placing the ultrasound transducer, with the aid of acoustic coupling gel, on specific points of the chest or abdominal wall. By manipulating the transducer, the sonographer can visualize different cross-sections of the heart, ensuring a detailed assessment of its structure and function. Key transducer movements include sliding, angling, rotating, and tilting. The transducer is equipped with an index mark to assist with probe positioning and orientation. This mark aids in interpreting the orientation of the acquired B-mode images. Typically, the American Society of Echocardiography (ASE) convention is followed, wherein the index mark corresponds to the right side of the image display, providing consistent and interpretable anatomical images[37].

During TTE, a variety of standard views are employed to assess the structural and functional integrity of the heart. Each view offers a unique perspective, highlighting specific chambers, valves, and surrounding structures. While numerous other views and viewing planes exist, such as the parasternal long-axis (PLAX), parasternal short-axis (PSAX), subcostal, and suprasternal views, they fall outside the scope of this thesis. For the purpose of this research, the focus will be on several key apical views and the right ventricular inflow tract (RVIT) view, which are of particular relevance. These views are essential for understanding the electromechanical properties of the heart and contribute directly to the methods discussed in subsequent chapters.

The apical views, in particular, are among the most frequently used for transthoracic imaging and provide critical information about the heart's anatomy and function. These views are obtained by positioning the transducer near the true cardiac apex and directing it toward the heart's base, allowing for optimal visualization of the chambers and valves (Figure 3.3). Key apical views that will be explored in detail include:

- *Apical Four-Chamber (A4C) View*: This is one of the most fundamental views in echocardiography, providing a comprehensive display of all four heart chambers (right and left atria and ventricles). The transducer is positioned at the cardiac apex aimed toward the right shoulder with the index marker oriented toward the patient's bed (Figure 3.4). The A4C view offers a detailed visualization of the mitral and tricuspid valves, as well as the inferior septum and lateral walls of the ventricles.

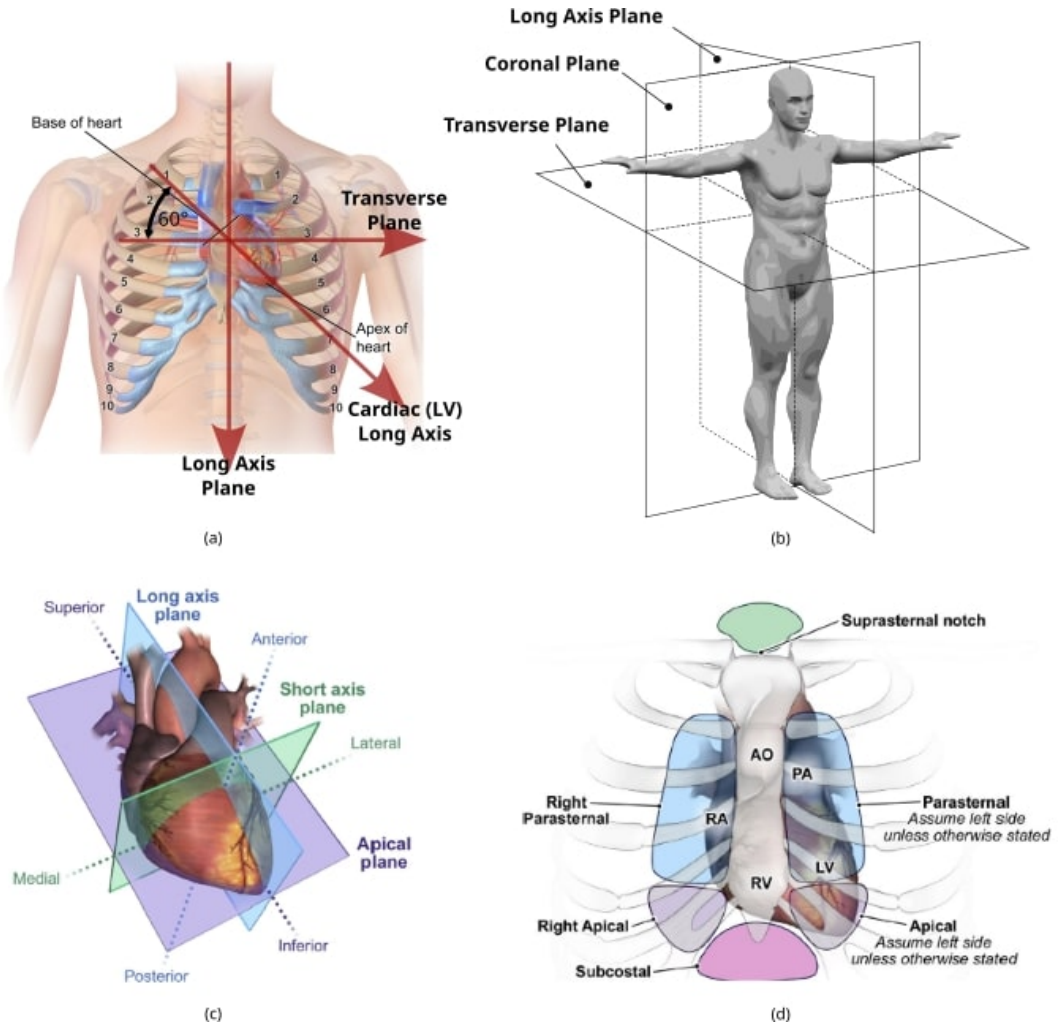

Figure 3.2: (a) Human torso with heart and rib cage, illustrating the transverse plane, long axis, and left ventricular (LV) long axis, along with the angles between these planes, demonstrating the heart's inclined position within the thorax. (b) Anatomical model of the human body showing the three standard anatomical planes. (c) Heart model depicting three key cardiac planes—short axis, apical, and medial—and the regions of the heart, including anterior, posterior, superior, lateral, medial, and inferior. (d) Human torso with rib cage and heart, highlighting the echocardiographic imaging windows: parasternal, apical, suprasternal, and subcostal views.

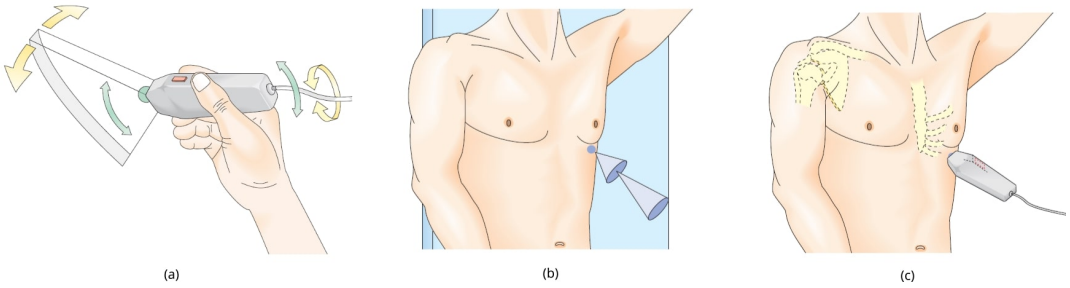

Figure 3.3: (a) Echocardiography transducer with red index marker and arrows illustrating potential movements, including angling, rotating, and tilting. (b) Diagram showing the location of the heart's true apex. (c) Placement of the transducer near the true apex, aimed toward the heart's base to acquire apical views.

This view allows for the evaluation of ventricular size, wall motion, and atrioventricular valve function.

- *Apical Two-Chamber (A2C) View*: By rotating the transducer approximately 60° counterclockwise from the A4C view, the A2C view isolates the left-sided structures. This view focuses on the left atrium, the mitral valve, and the left ventricle, particularly the anteroseptal and posterior walls (Figure 3.5). The A2C view is critical for assessing the function and morphology of the left ventricle and mitral valve.
- *Apical Three-Chamber (A3C) View*: Achieved through an additional 60° counterclockwise rotation from the A2C view, the A3C (or apical long-axis) view displays both the anterior septum and the posterolateral segments of the left ventricle, alongside the left ventricular outflow tract (LVOT) and aortic valve (Figure 3.6). This view resembles the parasternal long-axis (PLAX) view but provides a more comprehensive view of the apex.
- Apical Five-Chamber (A5C) View: From the A4C view, the A5C view is obtained by angling the transducer anteriorly until the LVOT and aorta come into focus. In addition to the four chambers, this view highlights the aortic valve, often referred to as the "fifth chamber," making it useful for assessing left ventricular outflow (Figure 3.7).
- *Apical 3.5-Chamber (A3.5C) View*: This is an intermediate view between the A4C and A2C planes, achieved through slight counterclockwise transducer rotation of 30° from the A4C (Figure 3.8). In this position, the right chambers are slightly foreshortened compared to A4C. Although not a standard acquisition, it is frequently used to offer a unique perspective on the heart's anatomy, providing additional information about the anterior LV and RV walls and posterior septal wall that may not be captured in standard views[62, 78].

In addition to these apical views, the Right Ventricular Inflow Tract (RVIT) View will also be highlighted due to its importance in examining the right heart's function.

- *Right Ventricular Inflow Tract View (RVIT)*: To acquire this view, the sonographer begins with the probe positioned with the PLAX view. With

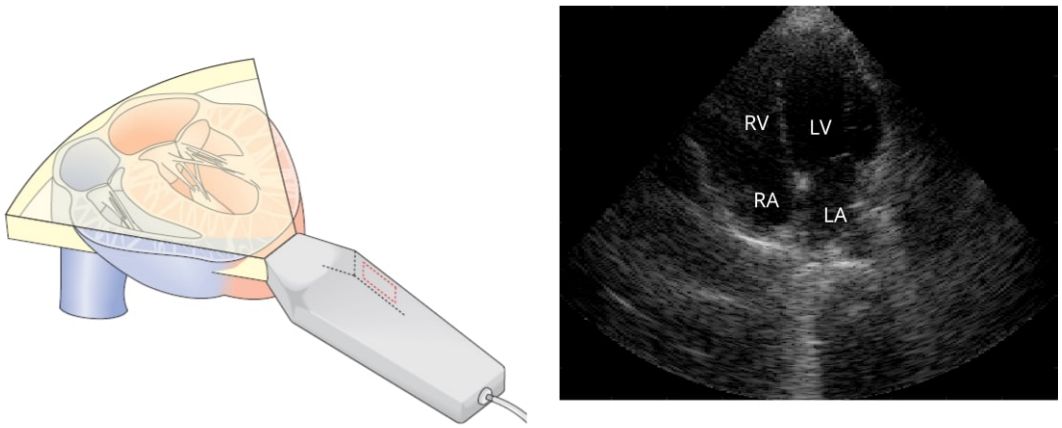

Figure 3.4: (a) Illustration of the echocardiography probe positioned at the apical four-chamber view, with a cross-section of the heart showing internal structures and the transducer marker directed toward the left side of the patient. (b) Example B-mode image of the apical four-chamber view, with the four heart chambers clearly labeled.

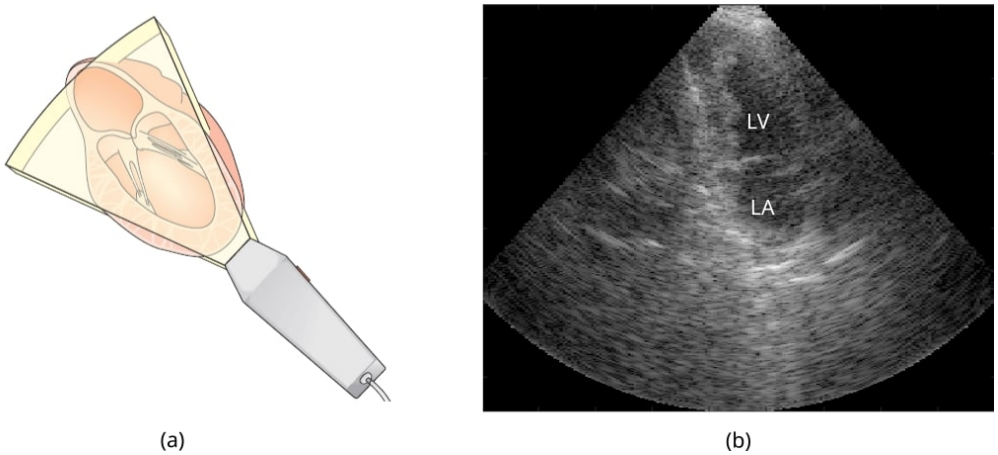

Figure 3.5: (a) Illustration of the echocardiography probe positioned at the apical two-chamber view, with a cross-section of the heart showing internal structures and the transducer marker on the left side of the patient, towards the left shoulder. (b) Example B-mode image of the apical two-chamber view, with the heart chambers clearly labeled.

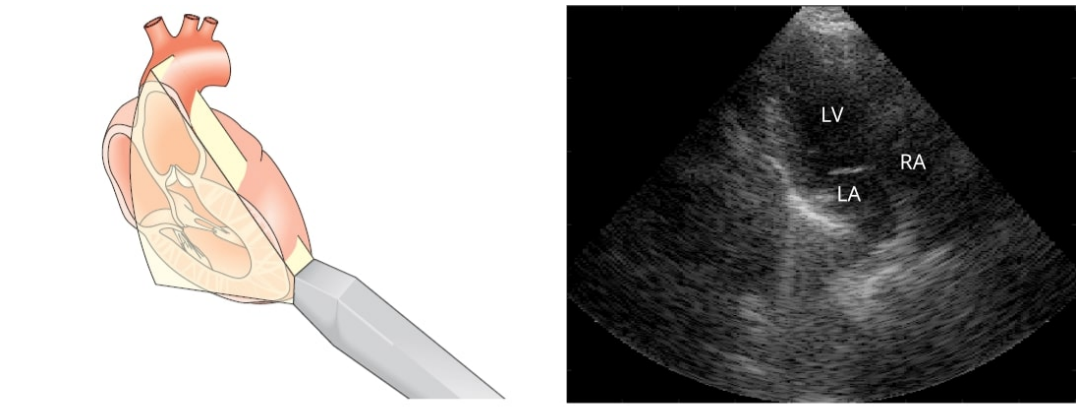

Figure 3.6: (a) Illustration of the echocardiography probe positioned at the apical three-chamber view, with a cross-section of the heart showing internal structures. The transducer is rotated 60° further counterclockwise. (b) Example B-mode image of the apical three-chamber view, with the three heart chambers clearly labeled.

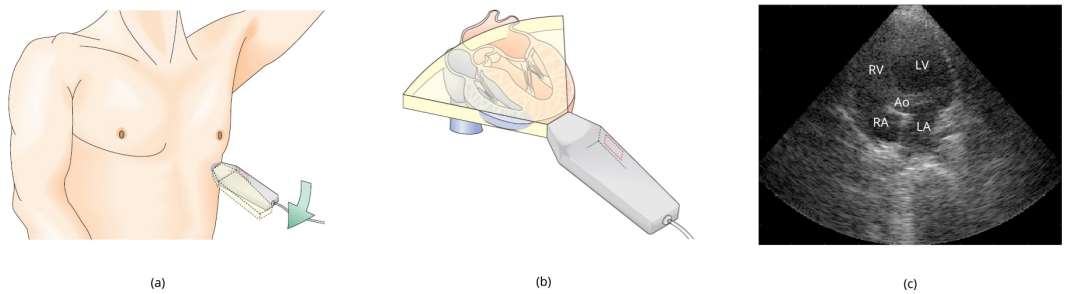

Figure 3.7: (a) Illustration of the transducer tilting from the apical four-chamber view to acquire the apical five-chamber view. (b) Illustration of the echocardiography probe positioned at the apical three-chamber view, with a cross-section of the heart showing internal structures. (c) Example B-mode image of the apical five-chamber view, clearly labeling the four heart chambers and the aorta.

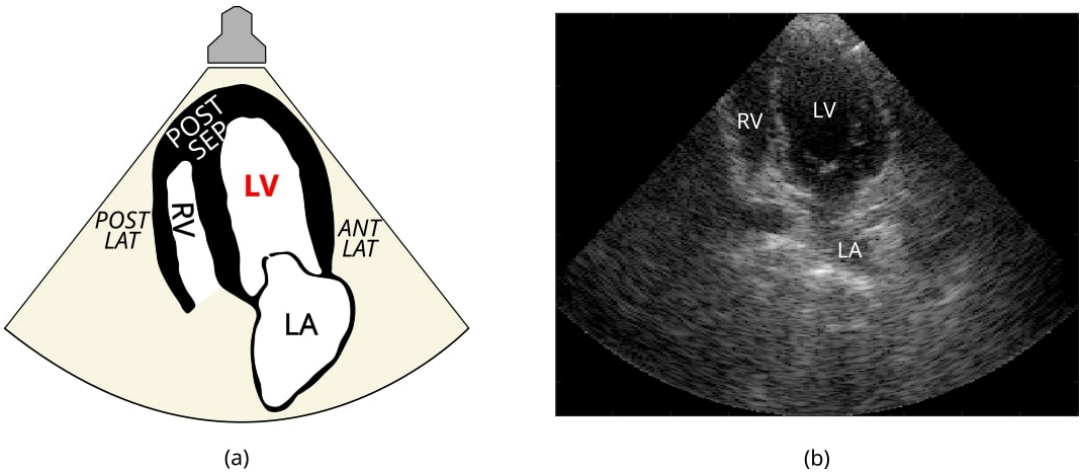

Figure 3.8: (a) Illustration of the echocardiography probe positioned at the apical three and a half-chamber view, with a cross-section of the heart showing internal structures. The transducer is rotated 30° clockwise from the apical four-chamber view. (b) Example B-mode image of the apical three and a half-chamber view, with the three heart chambers clearly labeled.

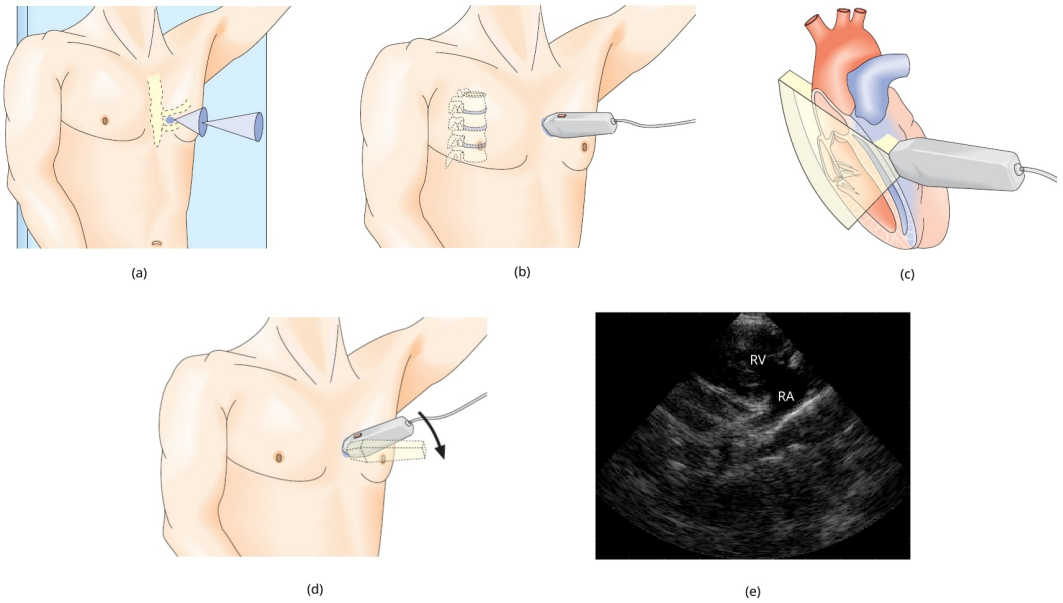

Figure 3.9: (a) Illustration showing the location of the parasternal window in the fourth intercostal space to the left of the sternum on a patient lying on their left side. (b) Illustration of transducer positioning to achieve the parasternal long-axis (PLAX) view, aimed perpendicularly towards the spine. (c) Cross-sectional view of the heart from the PLAX position, displaying internal structures from the tip of the ventricle to the aorta. (d) Depiction of the transducer tilting towards the patient's right hip to capture the right ventricular inflow tract (RVIT) view. (e) Example B-mode image of the RVIT view, with the right ventricle and atria clearly labeled.

the patient lying in a left lateral position with the left arm behind their head, the acoustic window is located between the 4th and 5th ribs, just to the left of the breastbone. The transducer is aimed perpendicularly toward the spine and the ultrasound displays a longitudinal section of the heart from the tip of the ventricle to the aorta. Keeping the patient's position and the transducer's mark orientation unchanged, the RVIT view is obtained by tilting the transducer inferiorly toward the patient's right hip. Small angular adjustments might be needed for optimal visualization[79, 80]. The RVIT view focuses on examination of the structure and function of the right heart chambers, including the tricuspid valve (TV). Portions of the right ventricle with the anterior RV wall positioned in the upper part and the inferior RV wall in the left. To the lower part of the acquisition, the RA is visible (Figure 3.9).

The above form the foundation of a comprehensive transthoracic echocardiographic examination, ensuring a thorough assessment of cardiac anatomy and function. However, two of the major obstacles during TTE are the rib cage and the air-filled lungs. These structures can obstruct the transmission of the ultrasound beam, making it necessary to utilize alternative viewing windows that avoid or minimize exposure to those tissues. Depending on patient anatomy and clinical needs, nonstandard viewing windows may be required to be explored. From the apical plane, there are a number of different views that can be acquired by rotating the probe counterclockwise around the cardiac long axis. Their orientation is not standard and depends on patient anatomy and the sonographer's expertise.

3.3 Introduction to Electromechanical Wave Imaging

Electromechanical Wave Imaging (EWI) is an innovative, non-invasive ultrasound based imaging technique, designed to track the heart's mechanical activity in real time. Unlike traditional techniques, which primarily focus on the electrical conduction of cardiac tissue, EWI enables the direct capture of the myocardium's mechanical deformations following electrical excitation. This allows the visualization of the electromechanical wave propagation throughout the heart, offering insights into the functional and structural integrity of myocardial tissue.

In this chapter, an in-depth analysis of the technical principles of EWI is presented, with a focus on the mathematical models and algorithms used in generating two- and three-dimensional activation maps. Starting with the ultrasound acquisition technique, the methodologies for estimating myocardial displacement and strain are explained, along with the process for calculating activation timings across the myocardium. Finally, the chapter addresses the steps involved in creating three-dimensional activation maps, offering a detailed description of the algorithms used to construct a comprehensive spatial representation of electromechanical activity.

3.3.1 High Frame Rate Acquisition

With the ultrasound probe coated with ultrasound gel and positioned at the apical viewing window of the patient, apical echocardiographic views are acquired with a Verasonics Research Vantage 256 (Verasonics Inc., Kirkland, WA, USA) and a 2.5 MHz P-4.2 phased array (ALT P4-2, Philips, Andover, Massachusetts). In standard 2D EWI imaging, these include the A4C, A3C, and A2C plus the additional non-standard A3.5C view. Using a high frame rate (2000 frames per second) single diverging wave sequence, with a virtual source focused 10.2 mm behind the 64 transducer elements, ultrasound radio-frequency signals (RF) are acquired to capture the minute movements and deformations of the heart walls during a heart cycle. Due to the tradeoffs associated with high frame rate imaging, particularly the lower resolution and signal-to-noise ratio in B-mode reconstructions, a standard 64-line B-mode acquisition is performed to facilitate accurate myocardium segmentation. The ECG signals are also acquired synchronously with ultrasound data.

Retrospective echocardiogram (ECG)-gating is used in order to temporally align the high frame rate acquisition with the anatomical B-mode acquisition using the R-wave peak signaling the ventricular activation. ECG-gating is a technique used to combine individual imaged sectors at different angles over several cardiac cycles into a large field-of-view (FOV) at high beam density while at the same time attaining high frame rates. The RF lines of each sector from separate cycles are then combined into a full-view 2D[81]. Combination of the data obtained from each one of the elements is called beam-forming and is performed during post-processing, resulting in the reconstruction of one RF frame per transmit. These RF frames contain phase information that is lost when generating B-mode images. Ultrasound

RF frames were reconstructed in polar coordinates from the raw signals obtained from the probe elements using a delay-and-sum algorithm[64]. Since the echo of each source reaches the probe elements from different paths, the captured signals have a similar waveform but different delays and phases. These delays can be determined from the speed of sound in the tissue, the distance between the elements and the distance between the source of the echo. By applying these delays during beam-forming so that all are in phase, the final signals can then be summed to obtain the final signal.

3.3.2 Myocardium segmentation and Axial Displacement Estimation

Initial segmentation is manually performed on the first frame of the reconstructed B-mode image, providing a reference point. To track myocardial motion throughout the cardiac cycle, a 1D axial RF cross-correlation method is performed[82]. This involves comparing the reference segmentation window to other windows from different frames of ultrasound data within a predefined search range, in this case, a 6.2 mm search window with 90% shift overlap. The degree of similarity is quantified using a cost function, and motion is inferred from the temporal or spatial shift between the reference window and the best-matching window. Subsequently, the computed displacements are used to track myocardial movement on the anatomical B-mode throughout one cardiac cycle[61, 64].

3.3.3 Axial Incremental Strain Estimation

Following displacement estimation, 1D axial incremental strains—representing the change in strain between consecutive frames— are estimated for each pixel in the myocardium mask using a least-squares estimator with a 5 mm kernel[83]. Cumulative strain, which reflects the total deformation accumulated over time, is closely linked to incremental strain through its temporal derivative. A significant aspect of this relationship is that when cumulative strain reaches its extremum (either a maximum or a minimum), the incremental strain approaches zero. This results in a zero-crossing point, which may shift from positive-to-negative or negative-to-positive, depending on the alignment of the heart wall relative to the axial estimation direction. Radial thinning (negative strain) is associated with longitudinal lengthening, whereas radial thickening (positive strain) correlates with longitudinal shortening. The specific zero-crossings of interest also vary with the imaging perspective. For apical views, positive-to-negative zero-crossings are most relevant, while in parasternal long-axis views, negative-to-positive crossings are more pertinent, due to the orientation of the ultrasound beam in relation to the myocardium[63, 64].

The resulting strains, incremental or cumulative, can be visualized by color-coding them and layering them on top of the grayscale B-modes with only the region of interest shown for better interpretation. Healthy apical contracting tissue can have interframe strains in the order of 10^{-3} magnitude. Since the myocardial wall movement can be tracked throughout the cycle, this can be visualized for the entire heart cycle. This can also be done with the previously calculated displacements.

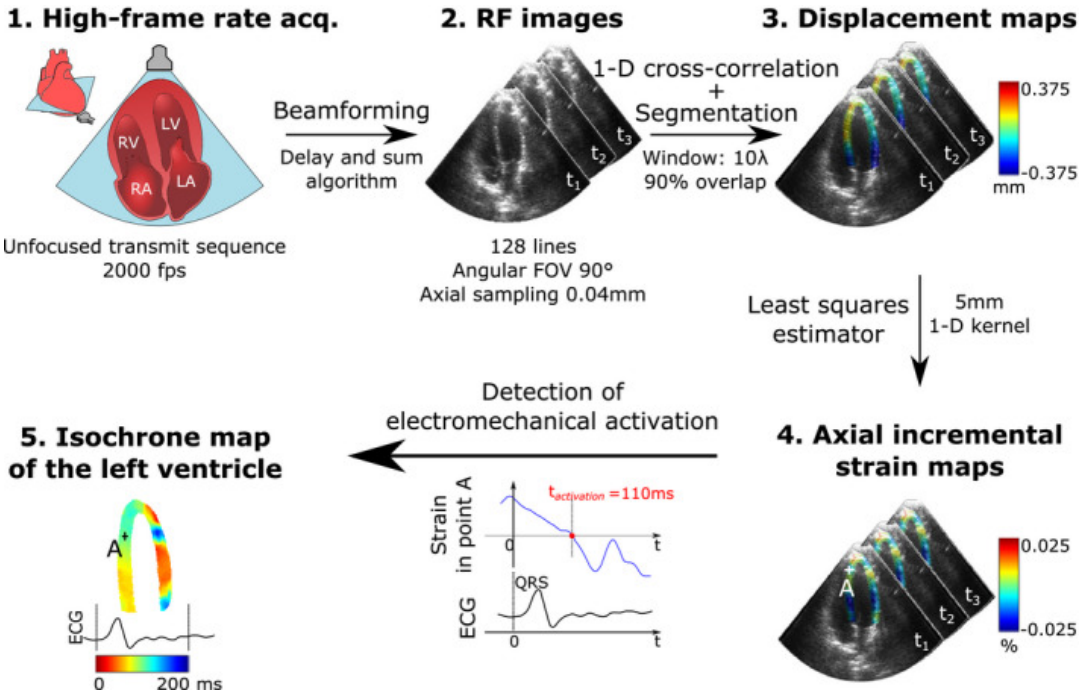

Figure 3.10: Pipeline flowchart of EWI algorithm: 2-D images of the heart are acquired at a high frame rate, the axial displacements, and the incremental strains of the myocardium are estimated; the zero-crossings of the strains indicating the electromechanical activation are detected for each point in order to generate an activation map.

3.3.4 2D Isochrone Generation

To determine the onset of myocardial contraction, the first positive-to-negative zero-crossing (negative-to-positive for parasternal long-axis views) following the onset of electrical activation, defined as the start of the QRS complex on the electrocardiogram (ECG), is identified. For atrial contractions, the origin is defined by the P-wave. A set of representative points on the myocardium are selected, and their zero-crossings (ZC) are manually extracted from the incremental strain curves. Since manual selection of ZC can be time consuming and limited by inter-observer variability and operator bias when dealing with large data populations, more recently an automated technique for ZC selection has been developed[78]. These points are then used in a Delaunay triangulation-based cubic interpolation to generate a smooth, continuous representation of the myocardial surface also known as the 2D isochrone[63]. This process is repeated for each acquired view. A complete pipeline flowchart for EWI is shown in Figure 3.10.

3.3.5 3D Rendered Isochrone Generation

The originally developed standard 3D electromechanical activation map generation algorithm[62], operates under two primary hypotheses: (a) the relative positions of all four views are organized in a theoretically ideal configuration, adhering to conventional cardiac imaging practices, and (b) the apical points and median axes of the four different views are aligned and correspond to the apical points within the 3D matrix used for map construction.

The process begins with tracing the left ventricle (LV) (or left atrium (LA)), after which the traced points are passed into a computational function designed to fit an ellipsoid shape. The major axis of this fitted ellipsoid is assumed to represent the median axis of the LV, thereby defining the z-axis direction in the resulting 3D representation. This median axis serves as a critical reference point for the spatial orientation of the heart within the 3D mapping space.

Following the establishment of the median axis, the algorithm proceeds with the extraction of positional and activation time values from the two-dimensional (2D) isochrone images. This extraction is carried out in polar coordinates for precision and consistency. For each point incrementally along the z-axis, the radial distance of each wall point is calculated using a perpendicular transverse axis. Activation timings are then extracted for each point (Figure 3.11). These calculated values are stored in a 3D matrix at locations defined by the polar coordinates: radius, theoretical angle (specific to each view with a 180-degree difference between opposing walls), and altitude along the z-axis. This sequence is repeated for each of the four views to ensure comprehensive data coverage.

Upon completion, the 3D matrix is populated with eight theta values, corresponding to two values per view, distributed around a 360-degree circle. A radial interpolation process is applied to these theta values for each radial position and z-axis position. This interpolation results in a smooth circumferential profile within the 3D matrix, which effectively describes the geometry and electromechanical activation times in polar coordinates. These polar coordinates are subsequently transformed into a Cartesian coordinate system to facilitate visualization. Custom MATLAB functions are utilized to plot these data, allowing for the detailed visualization of the cardiac activation patterns. The pre-interpolation positions of the four initial echocardiographic views are stored in a separate 3D matrix, which can be visualized as needed to provide a reference framework.

While the original algorithm was primarily developed to render the ventricles, it was later adapted to include the right ventricular (RV) wall, thus enabling complete chamber visualization while preserving the integrity of the matrix format. Although the existing algorithm demonstrates significant capabilities for generating 3D electromechanical activation maps, its usability and effectiveness are limited by several factors.

Firstly, the algorithm is not user-friendly. It requires considerable manual input and manipulation, necessitating a foundational knowledge of coding and the ability to manually execute various algorithmic steps. This complexity poses a barrier to adoption for clinicians and researchers who may not possess advanced programming skills. Additionally, the algorithm is designed to run offline, relying on code that is dispersed across multiple scripts. This structure demands a thorough understanding of the procedural steps, making it challenging to use without specialized knowledge.

Secondly, the algorithm's functionality depends heavily on accurate manual segmentation of the heart chambers. Since the algorithm processes only full-heart data, users must perform additional segmentation to delineate specific heart chambers. This requirement increases the workload and introduces the possibility of user-induced variability and errors. Moreover, the

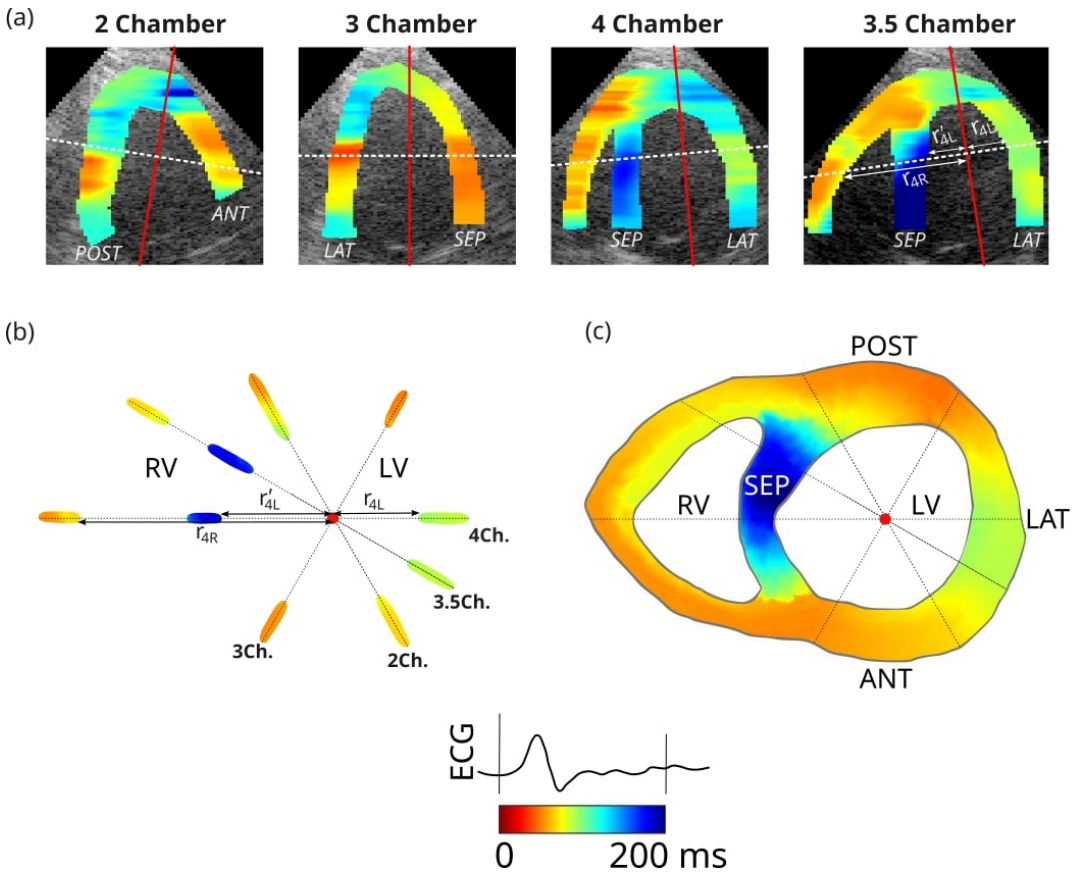

Figure 3.11: (a) Isochrone maps generated from the four acquisitions for normal rhythm. The median axis is indicated with a solid line, while the dotted lines correspond to the considered transverse slice. (b) For the considered slice, in each view, the radial positions of the walls (e.g., r_{4L}) and the activation time values are extracted and organized in a 3D matrix, in polar coordinates. (c) A linear interpolation around the circumference yields a smooth map.

algorithm often uses substantial computational resources rendering data that are ultimately unnecessary and later cropped or excluded during visualization. This inefficiency limits the algorithm's practicality, particularly when rendering data for multiple patients.

Another significant limitation is the algorithm's dependency on the A4C view for accurate positioning and value extraction. This dependency, stemming from how the code was initially structured, does not directly affect the results or outcomes but limits the algorithm's versatility. Also, the fixed view configuration can lead to under-sampling in certain regions, particularly along the anterior RV wall. Such under-sampling may result in gaps or reduced detail in the representation of cardiac activation patterns, potentially compromising the comprehensive accuracy of the activation map.

3.4 Methodology

3.4.1 Data Overview

This study utilized data from three human patients and one canine subject to investigate cardiac function and abnormalities through advanced ultrasound acquisition and electromechanical wave imaging (EWI) 3D rendering

techniques. Each subject presented with distinct cardiac conditions, including various forms of ventricular ectopy, cardiomyopathy, and, impaired left ventricular function. These cases were specifically selected to highlight the limitations of the current 3D rendering algorithm for EWI, and the advancements of the proposed 3D rendering algorithm with a focus on improving localization and visualization of abnormal cardiac tissue.

Patient A is a 24-year-old female diagnosed with dilated cardiomyopathy (DCM) and mid-septal fibrosis, which were identified through cardiac MRI. She presented with a high burden of symptomatic ventricular ectopy (VE) originating from the right and left ventricular outflow tracts (RVOT and LVOT). A previous attempt at radiofrequency ablation (RFA) targeting these ectopic sites was unsuccessful. Given the persistence of her symptoms and arrhythmias, the patient underwent further diagnostic evaluation, with the possibility of performing a transvenous ethanol ablation to eliminate the ectopic foci. The case of Patient A highlights a common challenge in the treatment of VE in patients with DCM and myocardial fibrosis, where standard ablation procedures may not fully address the underlying pathology. The presence of fibrosis in the mid-septum likely contributed to the initiation and maintenance of abnormal electrical activity, making the patient's condition more resistant to conventional therapies.

Patient B is a 61-year-old female with frequent ventricular ectopy, originating from the RVOT, as revealed by multiple Holter ECG studies, which recorded between 15% to 31% of her heartbeats as ectopic. Her baseline ECG suggested arrhythmogenic right ventricular cardiomyopathy (ARVC), though further imaging, including cardiac MRI and Positron Emission Tomography - Computed Tomography (PET-CT), did not detect any structural abnormalities consistent with ARVC. A previous endocardial-only RVOT ablation failed to eliminate the ectopic foci, and she was subsequently evaluated for a combined endo-epicardial radiofrequency ablation procedure. This patient's case demonstrates the difficulty in treating high-burden ventricular ectopy, particularly when imaging fails to reveal structural causes such as ARVC. The transition from an endocardial-only ablation to a combined endo-epicardial approach reflects the clinical need to address both surface and deeper myocardial substrates to achieve therapeutic success.

Patient C is a 27-year-old male with frequent premature ventricular contractions (PVC) and impaired left ventricular function, with an ejection fraction (EF) of 45%. Despite the high PVC burden, his cardiac MRI showed no evidence of myocardial scarring, and the PVCs were believed to be the primary cause of his reduced ventricular function. The ectopic activity was localized to the aortic root and LVOT, areas that often serve as challenging targets for ablation. The patient underwent a non-contrast CT ECGi study, which was used to guide the ablation procedure. Patient C's condition is indicative of the impact of PVCs on ventricular function in the absence of structural heart disease, as confirmed by the lack of scarring on MRI. The impairment in left ventricular function, combined with the high burden of PVCs, necessitated a precise mapping of the ectopic origin for effective ablation.

A healthy male mongrel canine, weighing 31 kg, was included in this

study to provide comparative data on cardiac arrhythmia and the application of EWI in a non-human full heart model. The data had been previously acquired for a different study, with approval from the Institutional Animal Care and Use Committee of Columbia University.

3.4.2 Data Collection and Processing

This section describes the methodology used for ultrasound data acquisition and electromechanical wave imaging (EWI) processing. It is important to note that data collection and initial processing had already been carried out, and the final processed data were provided. The focus here is on explaining the steps taken in obtaining and preparing the data for analysis.

For motion estimation, the equipment described above was utilized. Ultrasound waves were emitted in a circular pattern at a rate of 2000 fps, followed by standard B-mode acquisitions to capture detailed images of the heart's anatomy. The phased array transducer was placed at the apical window to acquire multiple ultrasound views by a trained sonographer. These acquisitions encompassed the four standard apical views—A4C, A3C, A2C, and A3.5—as well as additional predefined probe rotations around the apical window, which were tailored to each patient. In some cases, the right ventricular inflow tract (RVIT) view was obtained by positioning the transducer at the parasternal long-axis window. Multiple images were taken for each view, with the highest quality acquisitions selected for further analysis. For the canine subject, EWI whole heart acquisitions were obtained in the same four standard apical windows under anesthesia so that the heart was exposed and the data were collected under open-chest conditions following a lateral thoracotomy.

The next stage involved myocardium segmentation, which was performed on the first frame of each reconstructed B-mode image prior to systole. In the canine data, whole heart segmentation was performed, including the atria, the mitral valve, and the ventricles. In the human subjects, segmentation was limited to the ventricles. The standard EWI processing steps described earlier are applied to each acquisition.

For models where several non-standard views were used, a revised naming convention was implemented to organize and clarify the various apical views for this thesis. This system assigns the position and orientation of each view based on the placement of the transducer's index mark, ensuring consistency across the dataset. The patient was positioned supine, and a clock-face notation was adopted, with 12 o'clock oriented toward the patient's head and 6 o'clock toward the feet. In this framework, all apical plane views are organized around the long axis of the left ventricle, with their positions defined by corresponding clock-face times. For instance, the baseline A4C view is set at 3 o'clock, and other views are labeled by their rotation relative to this reference. In this scheme, the A4C view becomes the "3 o'clock 4Ch," while a 12 o'clock 2Ch view corresponds to a 90° rotation from the A4C position, showing the posterior and anterior walls of the left ventricle. This new notation can be better visualized in Figure 3.12.

In the case of the A5C view, which is obtained by tilting the transducer rather than rotating it, a simplified assumption was made. The A5C view

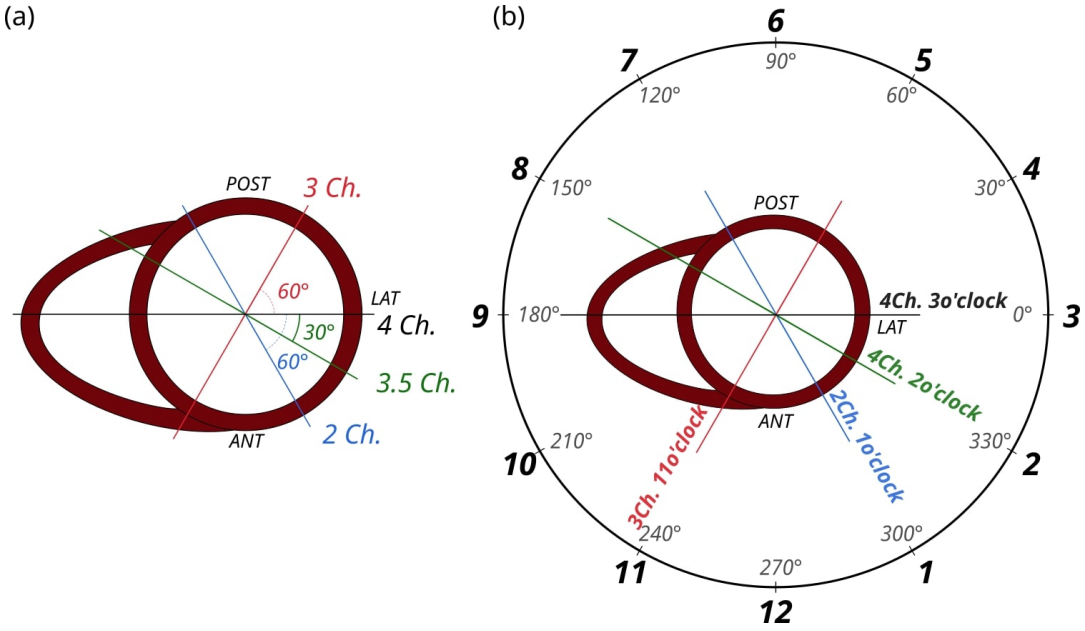

Figure 3.12: View from the heart base illustrating the relative positions of the four standard imaging planes on (a) the currently used, short-axis view, and (b) the new view notation. Views are named and oriented based on clock face positions, where each hour corresponds to a specific angular rotation around the LV median axis.

is approximated as a 20° counterclockwise rotation relative to the baseline A4C view. However, the RVIT view, focused on the median axis of the right ventricle, is not fully described by the clock-face convention. By default, this view is positioned vertically relative to the right ventricle.

3.4.3 Advanced 3D Rendering Algorithm Development

Significant upgrades were made, and new functionalities were added to the existing algorithm for generating 3D electromechanical activation maps to advance and improve its visualization capabilities. These upgrades focus on increasing flexibility, automation, and accuracy in the visualization of the heart's electromechanical activity, with the aim to enhance the ability to study various cardiac conditions.

Previously, the algorithm was restricted to four specific apical views, with predefined locations around the left ventricular (LV) axis, and relied heavily on the 4Ch view for positioning and activation time extraction. The enhanced algorithm now allows for greater flexibility, supporting multi-apical view rendering that is not constrained to these predefined views. Users can select any combination of views, even in the absence of the 4Ch view, providing more comprehensive and customizable imaging options (Figure 3.13a (i)). The only exception to this flexibility occurs when rendering using the RVIT view, which is discussed later. Additionally, views can now be placed at any desired position around the LV axis, allowing for tailored visualization based on specific clinical or research needs. This capability extends to rendering specific regions such as the atria or ventricles alone, or a full heart rendering, unlike the previous version, which was limited to full heart segmentation only. The process followed is similar as the one detailed earlier,

where the positions and activation information are extracted per view and stored in a 3D matrix (Figure 3.13b (i)) followed by a circumferential interpolation (Figure 3.14(ii)).

A notable improvement in the upgraded algorithm is the elimination of the requirement for pre-segmentation on the 2D isochrones. The original version necessitated user intervention to segment the heart chambers separately—if the user wanted to visualize the ventricles, they had to segment the atria, and vice versa. This additional segmentation step has been removed in the new implementation, which significantly reduces the need for user input and decreases computation time. The current algorithm reads the data directly, streamlining the process and making it more user-friendly and efficient. By bypassing the need for manual segmentation, the algorithm not only speeds up the analysis but also reduces the likelihood of user-induced variability and errors.

The method for determining the median axis has also been automated, enhancing consistency and reducing the potential for user error. Previously, users had to manually trace the left ventricular (LV) (or left atrial (LA)) chamber on the two-dimensional isochrone for each view. An ellipsoid was then calculated based on this tracing, with the major axis of the ellipsoid assumed to coincide with the long axis of each view. The upgraded algorithm automates this process by detecting the LV (or LA) cavity and selecting points on the inner wall using a two-dimensional ray-intersection algorithm, modified specifically for this application. These points are then used to calculate the ellipsoid. This automation reduces the time required for axis calculation, improves the consistency of axis selection across different users, and eliminates the need for manual tracing. The algorithm is also capable of automatically detecting the median axis of the right ventricle (RV).

Enhancements have also been made to the RV rendering capabilities. Previously, RV rendering was confined to angles between 120 and 240 degrees, primarily due to the limitations imposed by the four initial input views. The improved algorithm now allows interpolation beyond these angular constraints when required by the data, offering more realistic and flexible RV and RA shapes. This flexibility accommodates a wider variety of data inputs and avoids the imposition of artificially symmetrical heart shapes when the underlying data suggests otherwise.

New functionalities have been incorporated to render the left ventricular outflow tract (LVOT) effectively. The LVOT, as part of the aorta, is located in the anteroseptal region of the heart. During acquisition, the LVOT typically appears in views between $200^o - 240^o$ or between 9 and 11 o'clock on the clock face. Common views that capture the LVOT include the A5C and the A3C at the 10 and 11 o'clock positions. This feature utilizes an approach similar to that used for ventricles and atria, where the median axis is defined and a three-dimensional matrix is constructed. This matrix maintains the same format as previously but is specifically tailored around the median axis of the LVOT. The LVOT data are arranged with consistent relative theta positions, centered around the LVOT median axis (Figure 3.13b (ii)). Positional and activation values are then extracted along the z-axis and interpolated around the circumference, creating a detailed visualization (Figure 3.14(ii)). The LVOT

is automatically positioned on the 3D isochrone, though users have the flexibility to adjust its placement if necessary to suit specific visualization needs.

Further refinements were made to facilitate rendering the right ventricular inflow tract (RVIT). Since RVIT focuses on the RV's median axis, each point on the RVIT wall must be defined relative to the LV's median axis. This is achieved using simple geometrical relationships between the RVIT and the standard 4Ch view. For each point along the RVIT's median axis, new theta and radial values are assigned relative to the LV's median axis. Consequently, rather than a single RVIT view or "slice" corresponding to one position around the LV's median axis, multiple slices are generated on each side (posterior and anterior RV), allowing for a more comprehensive representation (Figure 3.13a (ii)). These slices, however, contain sparse activation values, requiring more complex interpolation methods to achieve accurate circumferential profiles, which slightly increases computation time. Despite using geometric relationships to position RVIT points, potential mismatches between the RV and RVIT walls may occur. To address this, the algorithm provides an option for users to adjust the RVIT data longitudinally before final rendering, ensuring more accurate alignment and visualization.

There is now support for full heart data rendering, including the mitral valve walls. Previously, while the algorithm required pre-segmentation on the 2D iso-chrones, it did not fully support whole-heart rendering. Now, the left, right, and septum walls are processed and rendered as described earlier, while the valve region is treated separately and added in its correct position within the 3D matrix prior to visualization. This allows for more detailed activation data to be visualized in areas that were previously omitted, contributing to more complete and accurate 3D maps.

Finally, the upgraded algorithm significantly reduces computation times and optimizes workflow. One innovative approach taken was to treat the atria as inverted ventricles in the rendering process. This simplification reduces the length and complexity of the code, further decreasing computation times while maintaining accuracy in the visualization. This approach capitalizes on the inherent anatomical similarities between atrial and ventricular structures, allowing the algorithm to generalize across different heart regions without needing distinct handling procedures for each chamber. By using the same fundamental code structure for both atria and ventricles, the algorithm not only becomes more efficient but also reduces the likelihood of errors that can arise from having multiple, separate code paths. This method also facilitates easier updates and maintenance of the software, as changes made to one part of the algorithm automatically propagate to other parts, maintaining coherence in the visualization output.

3.4.4 Graphical User Interface Development

To ensure that the 3D rendering code is accessible and easy to use, all functionalities were consolidated into a single graphical user interface (GUI) developed using MATLAB. MATLAB provides an integrated environment for app development, facilitating the layout of components and programming of app behavior. The GUI designed for Electromechanical Wave Imaging

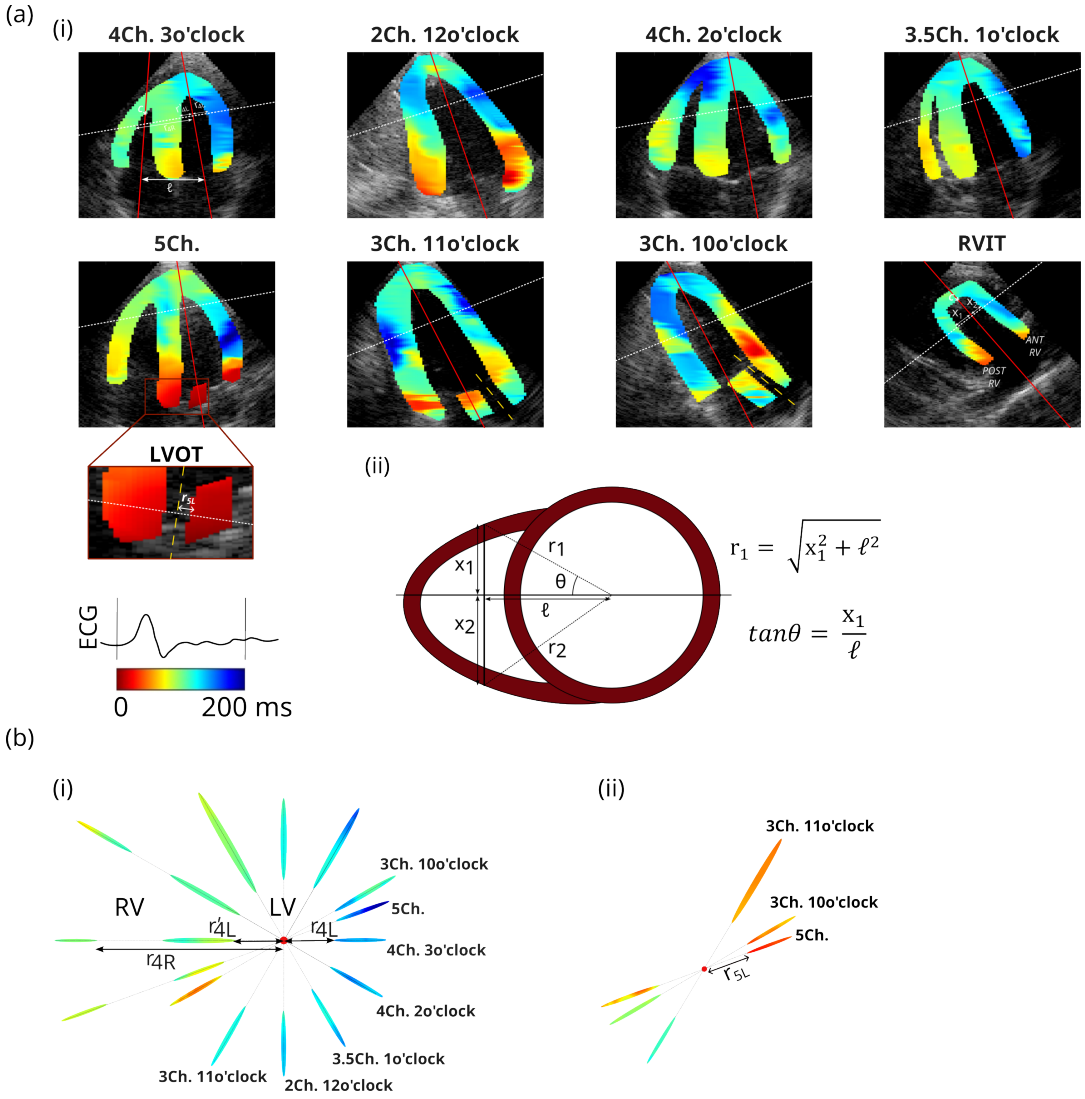

Figure 3.13: (a) (i) Isochrone maps generated from seven apical and one RVIT acquisitions. The median axis is indicated with a solid red line, while the dotted white lines correspond to the considered transverse slice. For views where the LVOT is visible, the median axis of the LVOT is indicated with a dashed yellow line. For the considered slice, in each view, the radial positions of the walls (e.g., r_{4L}, r'_{4L}, r_{4R}) and the activation time values are extracted and organized in a 3-D matrix, in polar coordinates. Where the LVOT is visible, radial positions (e.g., r_5L) and activation of the LVOT walls were also extracted. (ii) The polar positions (r_i, θ_i) of each point (x_1, x_2) along the RVIT wall are calculated relative to the median axis of the 4Ch. 3 o'clock view. A more detailed view of this figure can be found in Appendix A.

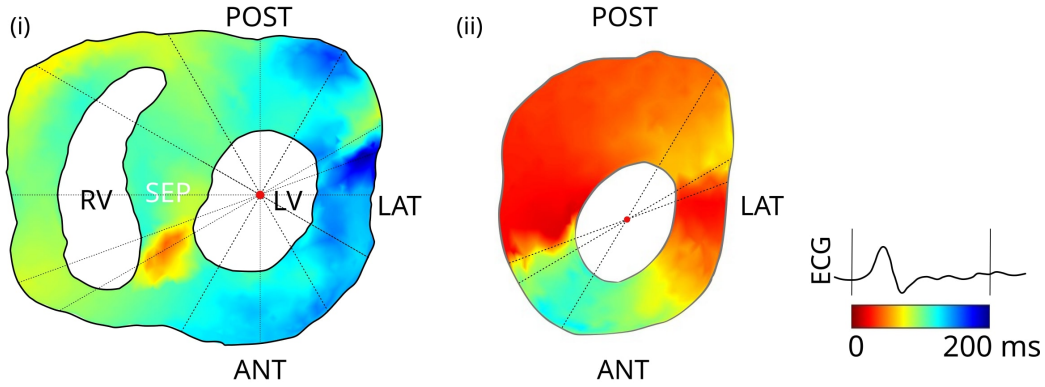

Figure 3.14: All radial and activation time values extracted are organized into a 3-D matrix. A linear interpolation around the circumference of the ventricles (i) and the LVOT (ii) yields smooth activation maps.

(EWI) 3D rendering offers a user-friendly interface that guides users seamlessly from the initial data input stage to the final visualization of rendered models. This approach not only minimizes the need for extensive code handling but also reduces the time required for execution, as all processes are centralized in one place. A flow chart outlining the GUI's main functionalities is presented in Figure 3.15. While this app was developed with the aim of processing 2D EWI maps, it has the ability to render any 2D cardiac imaging data that follow the input specifications, such as strain maps, or even generate 3D anatomical models from data without any activation information.

Data Input

The GUI allows users to easily input data by selecting and adding views for rendering, from a designated directory. Input data, represented as $m \times n$ matrices in MATLAB, are images depicting the left ventricle (LV) or left atrium (LA) on the right side and the right ventricle (RV) or right atrium (RA) on the left side, from the user's perspective. Each view requires three specific types of information:

- *View Name*: This identifier is used to distinguish between different views during plotting.
- *View Position*: Defined by minimum and maximum theta values, these numerical values, which differ by 180 degrees, specify the angular positioning of each view's walls around the LV's median axis. Zero degrees is defined at the 3 o'clock position, increasing counterclockwise. This system allows for custom view positioning while retaining the option to select the four standard, predetermined view positions. The view positions can be visualized from a top-down perspective, enabling the user to verify their accuracy. The minimum and maximum theta values correspond to the left and right sides of the image, separated by the theoretical median axis of the LV (or LA). Although this axis is not visible during the setup, it is calculated during rendering. Consistent with the convention that ventricles are always on the right side of the image, these theta values may also represent the positions of the septum and

ventricular walls. If the septum and ventricle walls are not simultaneously visible, the left-right notation applies.

- *Number of Visible Walls and LVOT Presence*: During data loading, the number of visible walls (excluding the LVOT) and the presence of the LVOT are determined using MATLAB's bwskel function, which performs skeletonization to extract the centerline of objects in a 2D binary image, and the bwconncomp function, which identifies and counts the connected components in the binary image. While these functions generally perform well, it is advisable to manually verify results in cases where data may be "messy" or ambiguous. Knowing the number of walls helps determine what needs to be rendered and the corresponding theta range, while recognizing the LVOT is crucial—even if it is not rendered—since its presence must be accounted for to avoid errors.

The GUI includes built-in checks to prevent potential rendering errors with status cells alongside each view in the table to indicate their presence. Examples include multiple views with identical theta values or default settings that have not been modified for one or more views.

Rendering Window

Once data input is complete, users can proceed to the rendering window. Here, they can select the rendering focus (atria, ventricles, or full heart) and specify whether to include additional structures such as the RVIT and LVOT. The interface also allows for the use of a previously calculated median axis if the same axis is desired. Additional options include a correction for discrepancies caused by the conversion from polar to cartesian coordinates and the separation of structures (LV, RV, and septum) for visualization or other purposes. While specifying an output path is optional, the rendered files will default to the data directory specified earlier. Users may also choose to provide a filename, though a default name will be used if left empty.

Rendering RVIT and LVOT views requires some input from the user, primarily defining the LVOT region, its median axis, and its potential position, should the user opt for manual placement. These inputs ensure accurate representation of the RVIT and LVOT structures within the 3D model.

Visualization Window

The visualization window allows users to open and examine the 3D rendered output, as well as the 3D matrix that stores the initial view positions before rendering. It is compatible with models generated using the original algorithm as well and offers various customization options such as color-map adjustments, mesh visibility, data decimation, transparency, plot titles, axes labels, limits, grid, color bars, and labels. Additionally, the following features are available for plotting and saving models:

- *Crop levels and planes*: Users can define crop levels along the X, Y, and Z axes which is especially useful for inspecting internal chambers in full heart models. Crop levels can also be applied to the LVOT segment, and arbitrary planes can be set to cut models along non-orthogonal sections.

- *Section Visualization*: Offers the ability to visualize specific regions like the LV, RV, or septum.
- *Difference Normalized Maps*: Visualizes the standard deviation of each point.
- *Binary Maps*: Visualizes areas of the model above or below a specific threshold.
- *Saving Options*
  - *Screenshot*: Saves the figure exactly as shown on screen.
  - *Standard Views*: Automatically saves eight predefined viewing positions.
  - *Model Rotation*: Saves a video showing a full 360^o rotation of the model.
  - *Downward Cropping*: Saves a video showing gradual cropping along the Z-axis to reveal activations inside the myocardial walls.
  - *Activation Sequence*: Saves a video showing the gradual activation of the model's walls over time.
- *Other*
  - *Model Info*: Displays key information such as minimum, maximum, and mean activation values for the loaded model.
  - *Bullseye Plot*: Generates a bullseye plot of the outer model's shell (either for the ventricles or the atria and septum) utilizing the open-source MATLAB algorithm Universal Ventricular Bullseye Visualization (UNISYS)[84]. UNISYS was developed to present single-layer 3D ventricular data in a circular bullseye format, which enhances the visual comparison of complex three-dimensional inter- and intra-patient observations. The algorithm transforms 3D single layer data into a circular 2D disk ("bullseye") through a series of translations and rotations, with interpolation to create a standardized, continuous visualization. This algorithm has been adapted from ECGi epicardial 3D ventricular data to accommodate the 3D rendered EWI data.

3.4.5 Comparison of Rendering Methods

The proposed advanced 3D rendering algorithm was evaluated through multiple comparative analyses against the previously developed 3D rendering method. For each subject, models were generated before and after the application of the new algorithm, allowing direct comparisons between the original and enhanced models. The new models introduced one or more additional views that contributed vital data to the original isochrones, enriching the overall visualization and potentially improving diagnostic accuracy.

A detailed comparison was also performed using the same input data for both algorithms to quantify their output similarity. This involved calculating the correlation coefficient between the original and new algorithms, using

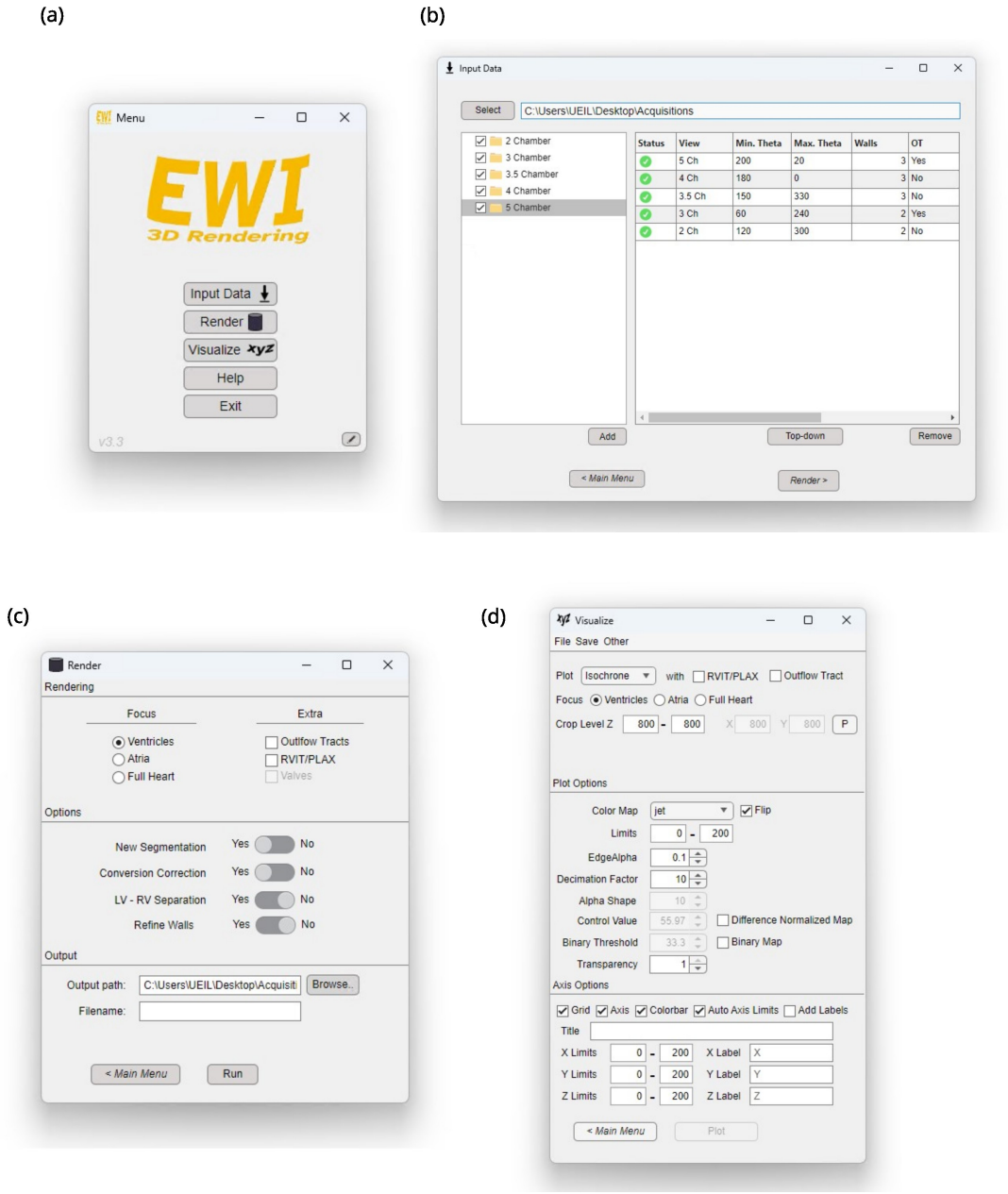

Figure 3.15: Companion app developed for this study, showcasing key features and functionalities, (a) Main Menu, (b) Data Input, (c) Rendering, and (d) Visualization windows.

the same 100 randomly selected non-zero points within a specified section of each model. This step ensured that both algorithms produced consistent and equivalent outputs for identical inputs. Additionally, the models were assessed for their dimensional accuracy and volumetric consistency.

To confirm the robustness of the updated algorithm and to show that the automated median axis detection performed the same despite different runs, it was tested multiple times on the same patient data. More specifically, the same patient data data was processed twice using the new version of the algorithm, and the resulting outputs were correlated to validate the reliability and reproducibility of the updated code. Lastly, the entire rendering process—from data loading to final model output—was timed for each algorithm version, providing a measure of the improvement in rendering times achieved by the new algorithm.

All rendering processes were performed on a dedicated workstation running Windows 11. The system was equipped with an Intel(R) Xeon(R) Gold 6230 CPU, operating at 2.10 GHz with 2 processors and a total of 256 GB of RAM. All algorithms were developed and tested using MATLAB version 2023b[85], utilizing MATLAB's built-in as well as user created functions from the MATLAB File Exchange for computational tasks. No GPU acceleration techniques were employed during the execution of the MATLAB codes. The consistent use of this hardware and software configuration ensured that the performance benchmarks and comparisons between different rendering algorithms were conducted under uniform conditions.

3.5 Results and Discussion

3.5.1 Enhanced Spatial Coverage

A major improvement in the advanced 3D rendering algorithm is the inclusion of the apical 5-chamber (A5C) view and the right ventricular inflow tract (RVIT) views, two key echocardiographic perspectives commonly employed in transthoracic echocardiography (TTE) exams. The addition of these views provides enhanced spatial coverage, particularly in the regions of the anterior septum and right ventricle (RV), which were previously under-sampled. In the original algorithm, the interpolated data in these areas relied solely on the apical 4-chamber (A4C) and apical 3-chamber (A3C) views. This limited coverage risked missing significant activation details, especially between these two views.

Figure 3.16 illustrates a comparison of results for Patient A, highlighting the effects of the additional A5C view. In Figure 3.16a, the 2D ventricular isochrones show early activation within the septal wall, clearly visible due to the integration of the A5C view. Figure 3.16b presents the positional relationships of the views, both before and after the addition of the 5-chamber, with Figure 3.16c offering a 3D representation of the isochrone data positioned around the LV median axis. The impact of the A5C view is most evident in Figure 3.16d, where the 3D-rendered isochrones demonstrate a more precise localization of early (red) and late (blue) activation zones, particularly along the septum. In comparison, the 3D model generated from the original four

apical views provides only vague indications of septal activation. By integrating the A5C view, the model achieves clearer and more defined early activation patterns in the septal region, improving the accuracy and reliability of electromechanical activation mapping.

The advanced algorithm's ability to incorporate the RVIT view further enhances its rendering accuracy and completeness. For Patient B (Figure 3.17), the inclusion of the RVIT view alongside the standard apical views leads to improved activation mapping in the anterior wall of the right ventricle (RV). The 3D plot in Figure 3.17c demonstrates the expanded spatial coverage offered by the advanced algorithm. Without the addition of the extra detail the RVIT view introduces, the anterior RV wall shows earlier activation towards the base of the ventricle due to the data interpolation from the A4C to the A3C views (Figure 3.17d (i)). In contrast to the original algorithm, the additional RVIT view in the advanced algorithm allows for better tracking of electrical activity, as shown in the 3D-rendered isochrones (Figure 3.17d (ii)) where compared to the original standard model, activation details shift closer to the ventricular apex, offering a more realistic representation of the patient's activation map.

With the integration of the A5C and RVIT views, the new 3D rendering algorithm demonstrates significant improvements in spatial coverage, particularly in regions that were previously under-sampled. These additions have enhanced the accuracy of electromechanical activation mapping by providing clearer early activation patterns in both the septal and RV regions. This improved spatial resolution not only results in more precise localization of activation zones but also achieves a more comprehensive and detailed representation of the heart's electrical activity.

3.5.2 Integration of Multiple Apical Views and Left Ventricular Outflow Tract (LVOT)

The advanced 3D rendering algorithm's ability to incorporate a greater number of apical views introduces substantial improvements in both anatomical accuracy and the ability to capture critical regions of electrical activation. Additionally, the ability to visualize the LVOT activation pattern in 3D enables the creation of models with more accurate anatomical and functional details.

In the case of Patient C, the use of seven apical views produces a more anatomically faithful ventricular model, particularly in depicting signs of early anteroseptal activation (Figure 3.18d (i)). As seen in Figure 3.18d (ii), the incorporation of the left ventricular outflow tract (LVOT) into the dataset adds crucial information to the 3D isochrone. By integrating LVOT data into the 3D isochrone model, the advanced algorithm provides more precise visualizations of activation patterns. This improvement is particularly significant when considering Patient C's medical history, where ectopic activity had been previously localized to the aortic root and LVOT. In this context, the 3D-rendered EWI model not only visualizes this known arrhythmogenic region but does so with improved accuracy and clarity, as the addition of the LVOT better represents the true activation onset.

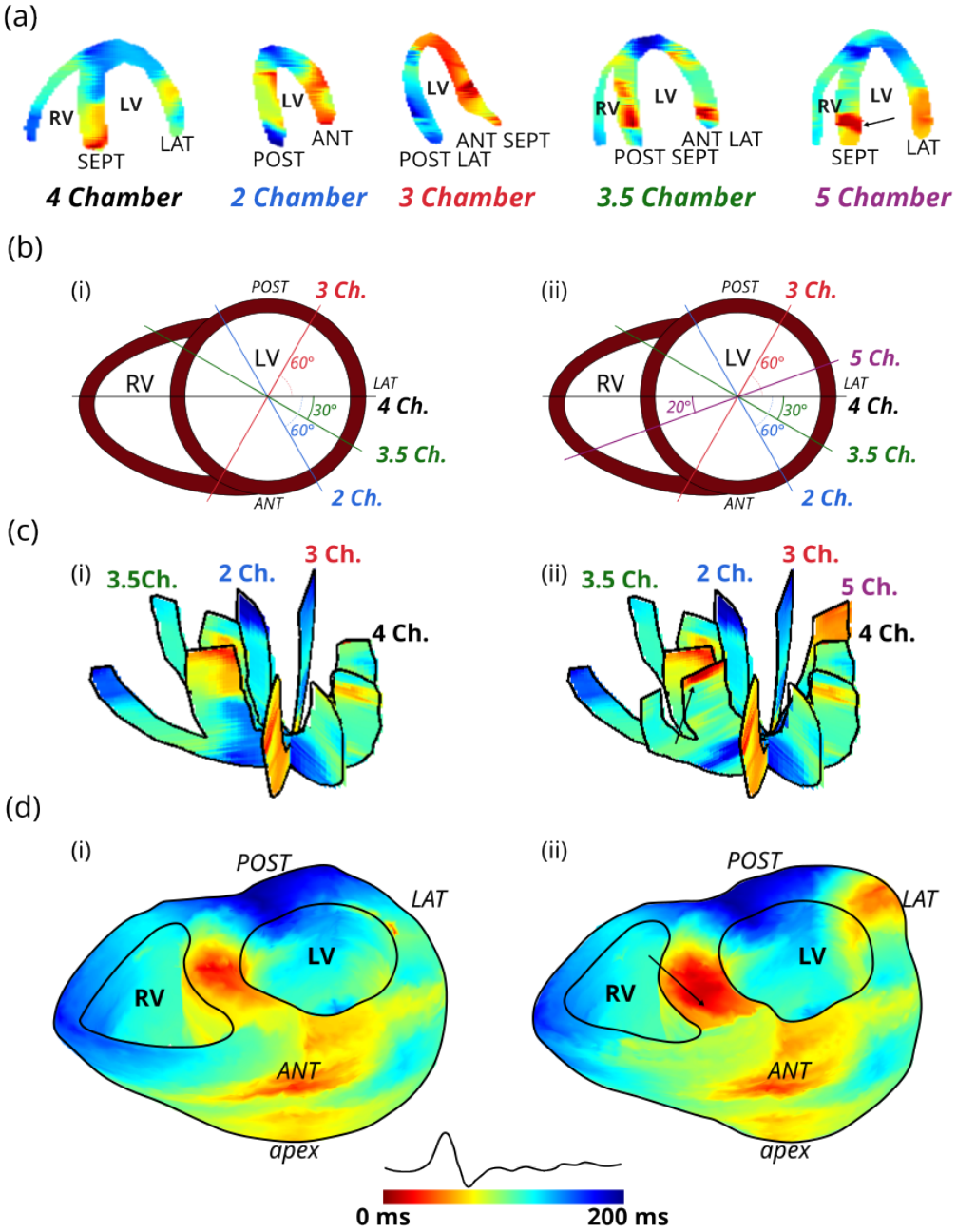

Figure 3.16: (a) 2D processed ventricular isochrones for Patient A displayed for five standard apical views: 4-Chamber, 2-Chamber, 3-Chamber, 3.5-Chamber, and 5-Chamber, (b) Short-axis view diagrams from the heart's base, illustrating the relative positions of the apical planes around the LV median axis for (i) the original algorithm and (ii) the advanced algorithm, incorporating the 5-Chamber view, (c) a 3D plot of each model showing the relative positions of the views before interpolation, (i) using the original algorithm with 4 views (4-, 3-, 2-, 3.5-Chamber), and (ii) using the advanced algorithm with 5 views (5-, 4-, 3-, 2-, 3.5-Chamber), (d) 3D-rendered isochrones showing activation times for the LV and RV for (i) the original and (ii) advanced algorithms. Arrows indicate areas of interest with improved localization. In all figures, red indicates early activation and blue represents late activation (in milliseconds).

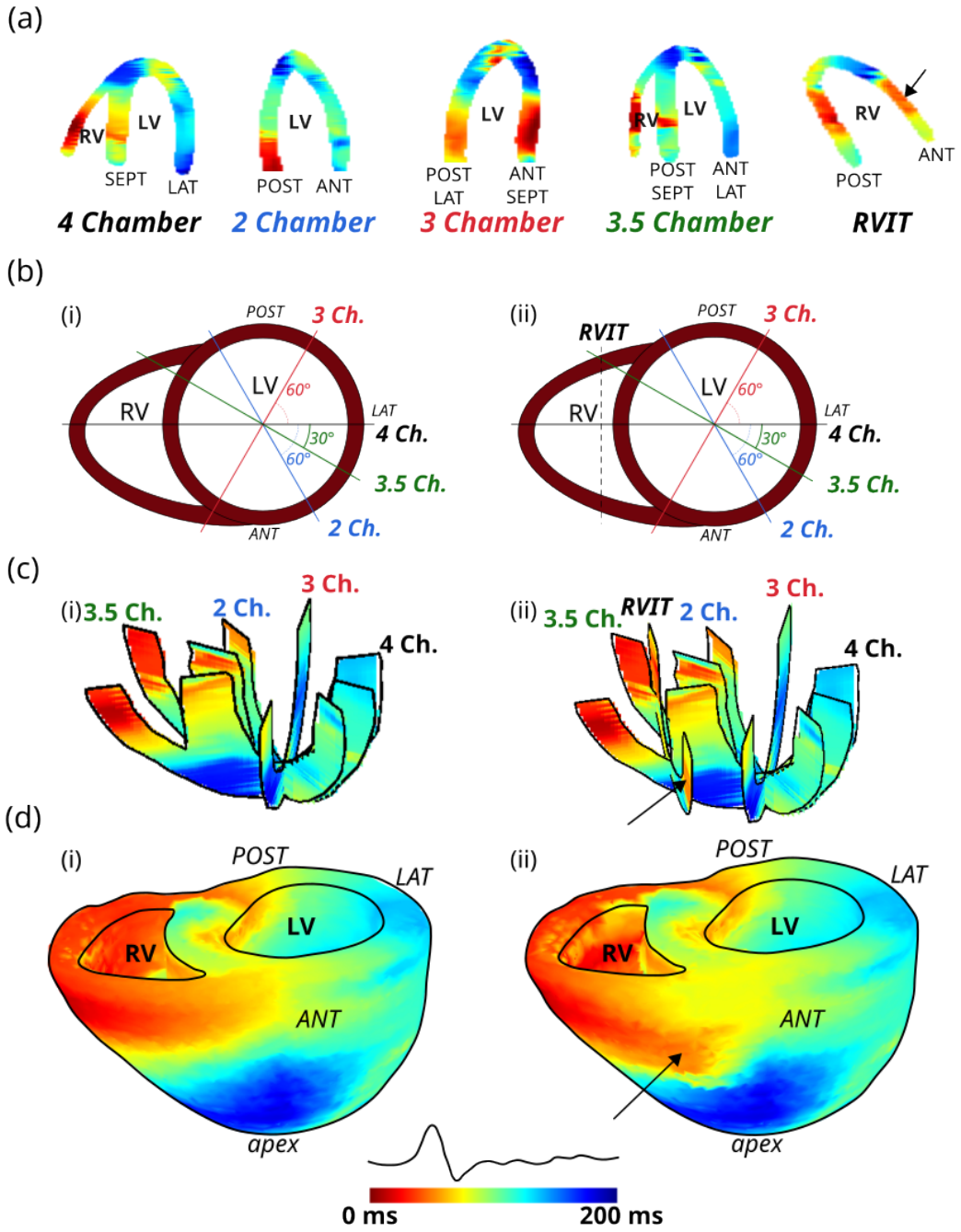

Figure 3.17: (a) 2D processed ventricular isochrones for Patient B displayed for four standard apical views: 4-Chamber, 2-Chamber, 3-Chamber, 3.5-Chamber, and one RVIT view, (b) Short-axis view diagrams from the heart's base, illustrating the relative positions of the apical planes around the LV median axis for (i) the original algorithm and (ii) the advanced algorithm, incorporating the RVIT view, (c) a 3D plot of each model showing the relative positions of the views before interpolation, (i) using the original algorithm with 4 views (4-, 3-, 2-, 3.5-Chamber), and (ii) using the advanced algorithm with 5 views (4-, 3-, 2-, 3.5-Chamber, RVIT), (d) 3D-rendered isochrones showing activation times for the LV and RV for (i) the original and (ii) advanced algorithms. Arrows indicate areas of interest with improved localization. In all figures, red indicates early activation and blue represents late activation (in milliseconds).

This extension from the previous four views to seven enables a more comprehensive sampling of the myocardium, filling gaps in spatial coverage and leading to a more detailed electromechanical activation map.

3.5.3 Full Heart Models and Valve Rendering

The advanced 3D rendering algorithm also introduces the capability to generate full heart models that not only capture detailed internal structures but also incorporate 3D activation maps of the mitral valve. This is a significant enhancement in the level of anatomical and functional detail provided by the model. Figure 3.19a demonstrates four 2D EWI isochrones for the canine subject, and their spatial arrangement is depicted in Figure 3.19b. The 3D model, shown in Figure 3.19c, offers two perspectives—posterior (i) and anterior (ii)—of the artichoke-like representation of the heart, illustrating the precise positioning of each isochrone around the left ventricle (LV). The final 3D-rendered EWI activation map is provided in Figure 3.19d, and cross-sectional geometries are visualized in Figure 3.19e. The mitral valve is isolated in Figure 3.19e (iii).

For the canine subject, which showed healthy heart function with a normal sinus rhythm, the observed activation sequence aligns with typical physiological patterns: atrial activation is followed by ventricular activation, with the wave passing through the mitral valve, as observed in early literature[86]. The opening and closing of the mitral valve occurs in synchronization with the rest of the cardiac cycle. The accompanying color bar, alongside the reference ECG signal, marks these key events—atrial and ventricular activation, as well as mitral valve dynamics. In line with the expected cardiac cycle, the 3D-rendered activation maps of both the full heart (Figure 3.19d) and the mitral valve (Figure 3.19e (iii)) display a correct sequence of electrical activation, closely matching the timing shown in the ECG.

This ability to accurately render the mitral valve and its activation not only enhances the visual clarity of the model but also provides a more holistic understanding of cardiac function. The comprehensive visualization of electrical activity makes this model a powerful diagnostic tool, particularly for evaluating complex arrhythmias that involve multiple regions of the heart.

However, as shown in Figure 3.19c, minor misalignments are occasionally present at the basal points of the LV. These deviations can be attributed to several factors. First, the registration of 2D EWI isochrones relies only on the alignment of the apical points, and second, variations in the relative positioning of the 2D ultrasound images, often due to manual acquisition, may slightly distort the overall 3D geometry. This can result in small imperfections, such as gaps or misalignments in the final 3D map. These gaps can sometimes be resolved successfully by increasing the alpha radius of the alpha shape. However, increasing the alpha value too much may lead to the loss of information in other parts of the rendering.

3.5.4 Accuracy and Performance Comparison

Figure 3.20 provides a comparative analysis of Patient A's models generated using the original and advanced algorithms, viewed from multiple angles. Both models were cropped at the same level to exclude regions inadequately

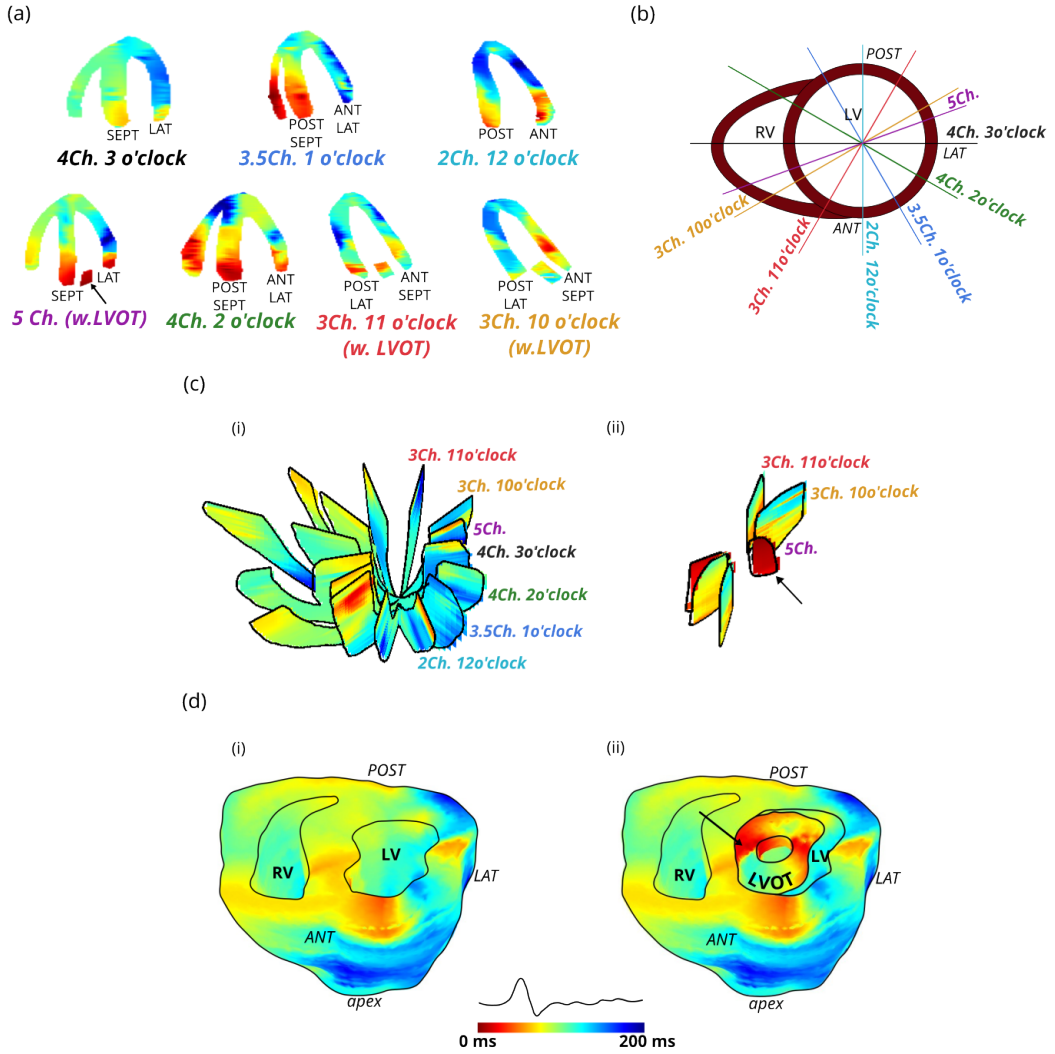

Figure 3.18: (a) 2D processed ventricular isochrones for Patient C displayed across seven apical views, with some including the LVOT. (b) Short-axis view diagrams from the heart's base, illustrating the relative positions of the seven apical planes around the LV median axis using the clock naming convention, (c) a 3D plot of the model showing the relative positions of the views before interpolation, (i) for the ventricles, and (ii) for the LVOT, (d) 3D-rendered isochrones showing activation times for the LV and RV for (i) the ventricle only and (ii) including the LVOT, both generated using the advanced algorithm. Arrows indicate areas of interest with improved localization. In all figures, red indicates early activation and blue represents late activation (in milliseconds).

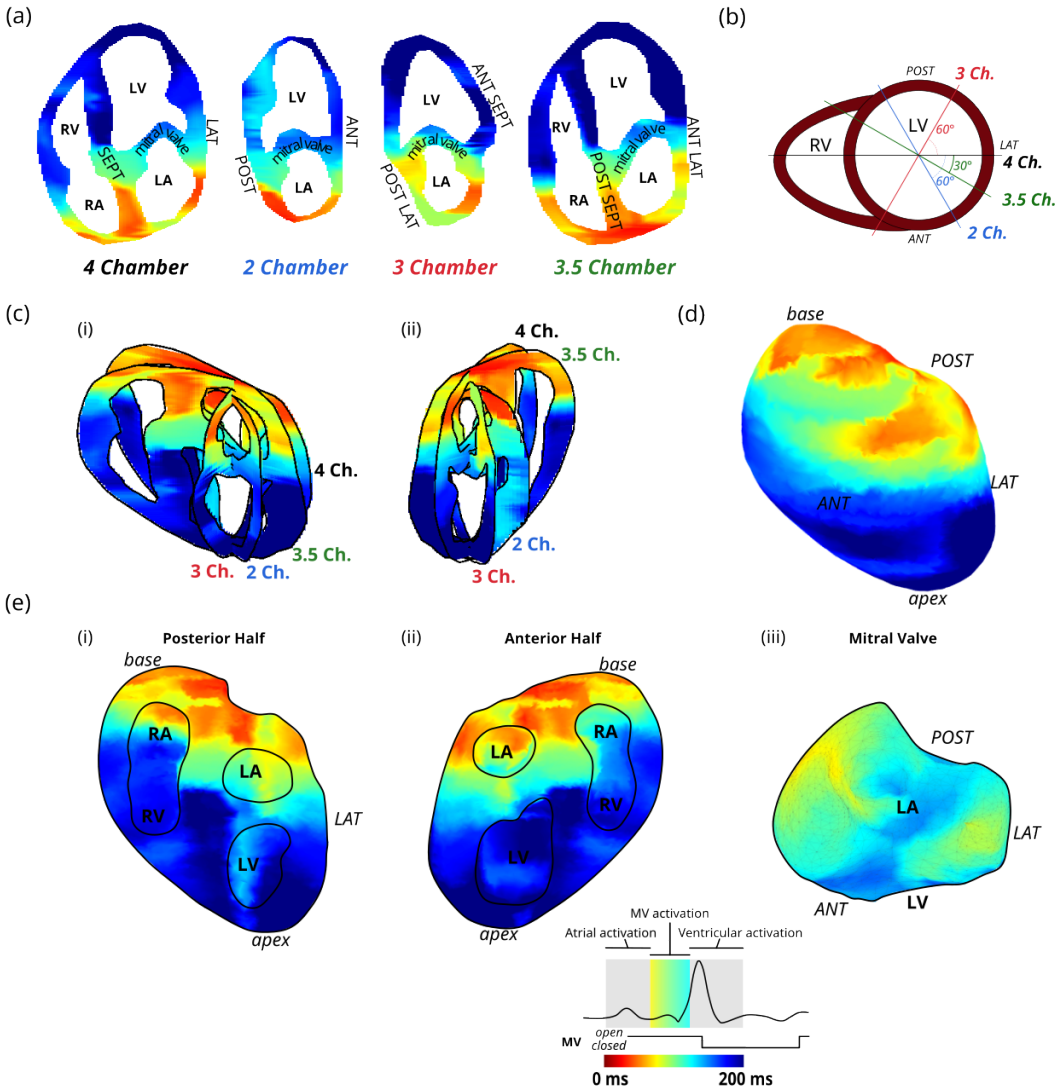

Figure 3.19: (a) 2D processed full heart isochrones with the mitral valve for the canine subject displayed for four standard apical views: 4-Chamber, 2-Chamber, 3-Chamber, 3.5-Chamber. (b) Short-axis view diagram from the heart's base, illustrating the relative positions of the apical planes around the LV median axis. (c) a 3D plot showing the relative positions of the views before interpolation in (i) anterolateral, and (ii) posterolateral view. (d) 3D-rendered isochrone showing activation times for both ventricles and atria. (e) Internal structures of the 3D-rendered full heart (i) posterior half, (ii) anterior half, (iii) mitral valve. In all figures, red indicates early activation and blue represents late activation (in milliseconds).

rendered by the original algorithm, particularly near the base where data consistency is unreliable. This issue often arises in cases where the septum extends beyond the boundaries of the LV or RV walls, creating discrepancies that the advanced algorithm can now handle effectively. For comparison, these areas were omitted from both models. Additionally, a uniform alpha radius of 0.0035 was applied to maintain consistency in the visualization of alpha shapes.

In the posterior RV walls shown in Figure 3.20a, c, and d (i), an empty area on the wall surface can be observed. These gaps are due to the inherent nature of the data, and not deficiencies in the algorithm itself. Typically, these voids can be filled by increasing the alpha radius value. Although the new model also exhibits this 'hole,' the section is filled in by maintaining the same alpha values for consistency (Figure 3.20a, c, d (ii)).

Although minor variations in shape are present, the overall geometric consistency between the models remains robust. An area of interest is highlighted on the anteroseptal wall (Figure 3.20a), where slight discrepancies in activation data are noted. These differences are likely superficial, resulting from the surface interpolation process rather than inherent algorithmic flaws. To further evaluate the algorithm's robustness, a cross-sectional analysis was conducted at three levels—apex, mid, and base—each divided into 16 segments at 30-degree intervals. The correlation coefficients for each segment are shown in Figure 3.21, comparing models generated using the original and new algorithms on identical datasets and median axes. Calculated using 100 random points per segment, the coefficients indicate excellent agreement between the models.

Figures 3.22 and 3.23 extend this analysis to validate the median axis calculation's reliability. Figure 3.22 presents correlation coefficients for 16 segments per cross-section, again using 30-degree intervals. Here, the original algorithm was run twice on patient A's data, with manual segmentation for median axis calculation performed each time. This comparison highlights how even slight variations in manual segmentation can affect model outcomes. Figure 3.23 presents coefficients for two models of patient A generated by the advanced algorithm using automatic median axis calculation. All coefficients were derived from 100 random points per segment. While manual segmentation still yields high correlations (most coefficients being ≥ 0.99), the automatic detection consistently produces identical results, underscoring the robustness of the new algorithm.

An essential aspect to consider is the geometric dimensions and overall volume of the produced models. Table 3.1 provides a comparison of the dimensions across each axis and the total volume in cubic meters (m^3) for both models. The consistency across all axes demonstrates that the advanced algorithm preserves the spatial accuracy of the 3D reconstructions generating models equivalent to the original when provided with the same input data, thereby validating its reliability.

Finally, Table 3.2 compares the execution times for various processing stages and total computational time between the original and advanced code implementations using Patient A's dataset. A 30% reduction in total processing time is observed, from approximately 8.4 minutes to 5.8 minutes. This reduction is most notable in the manual pre-segmentation phase, which has

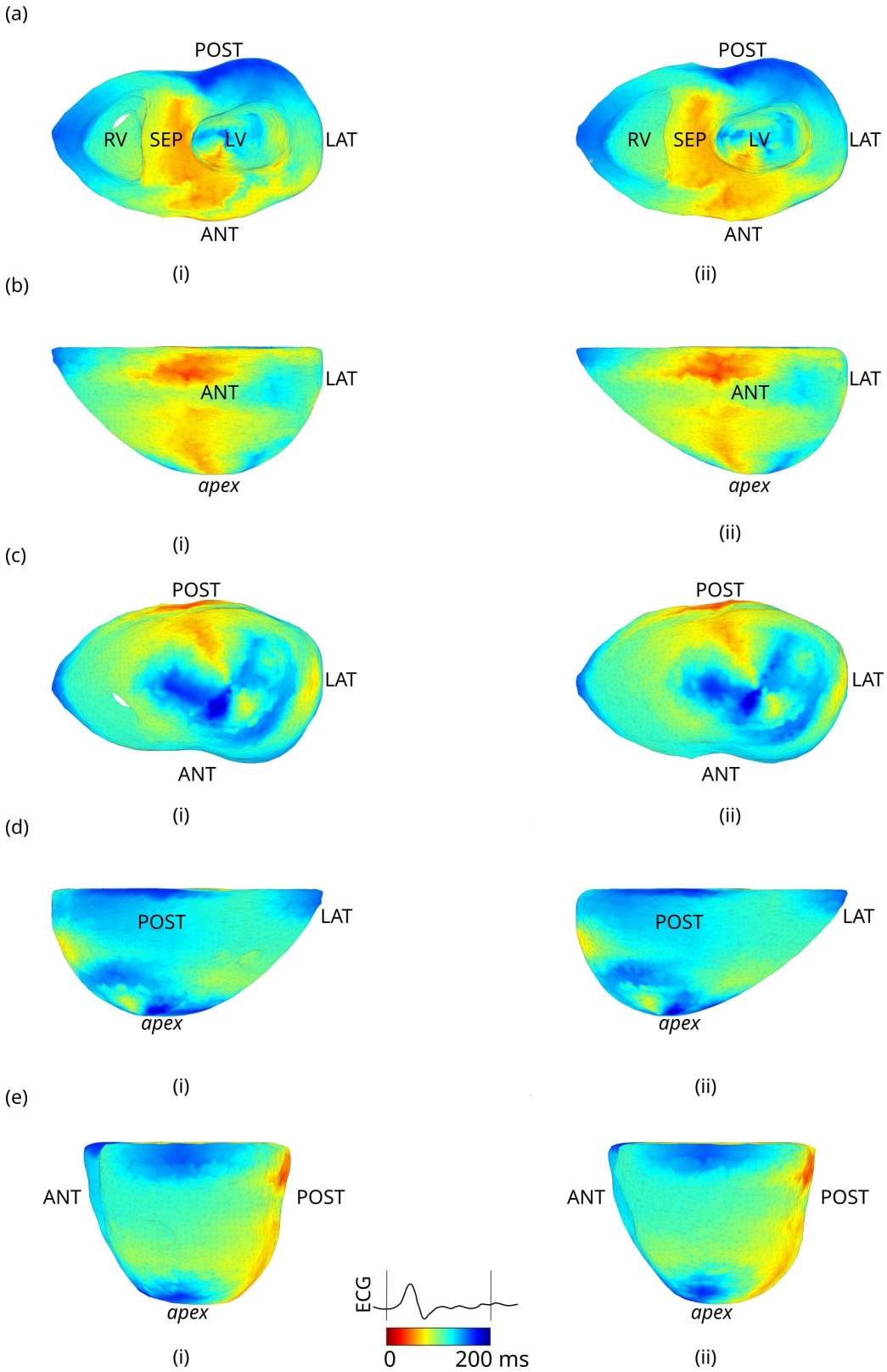

Figure 3.20: Comparison of Patient's A model created using the original and advanced algorithms, with each section showing a before (i) and after (ii) view from different perspectives. (a) Top-down view of the ventricles. (b) View of the lateral wall and the apex. (c) Bottom-up view from the apex. (d) View of the posterior walls. (e) View of the lateral wall. The same crop level and alpha radius for the alpha shapes are used in both cases to ensure consistent comparison of the models' outputs.

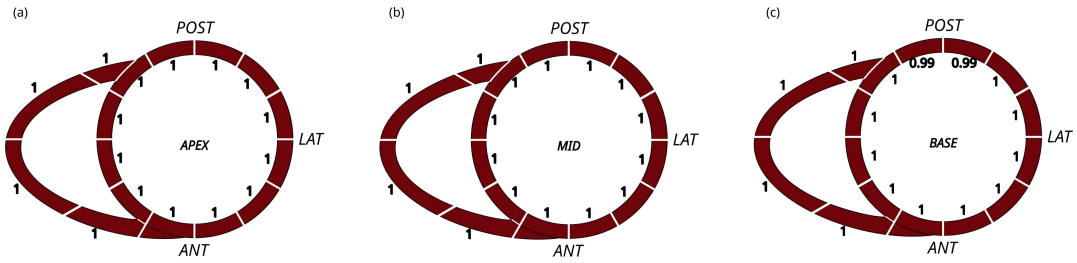

Figure 3.21: Cross-sectional analysis of the heart at three levels: (a) apex, (b) mid, and (c) base, each divided into 16 segments at 30-degree intervals. The correlation coefficients are displayed adjacent to each segment. These coefficients compare two patient A models generated by the original and new algorithms, using identical datasets and median axes. The coefficients were calculated using 100 random points per segment.

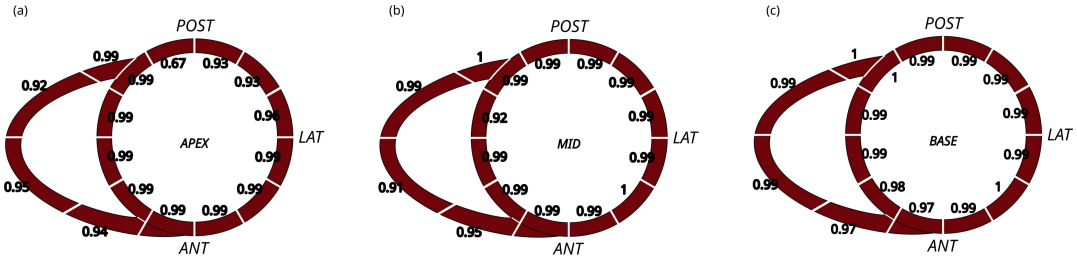

Figure 3.22: Cross-sectional analysis of the heart at three levels: (a) apex, (b) mid, and (c) base, each divided into 16 segments at 30-degree intervals. The correlation coefficients are displayed adjacent to each segment. These coefficients compare the results of running patient A's data twice using the original code with manual segmentation for median axis calculation. The coefficients were calculated using 100 random points per segment.

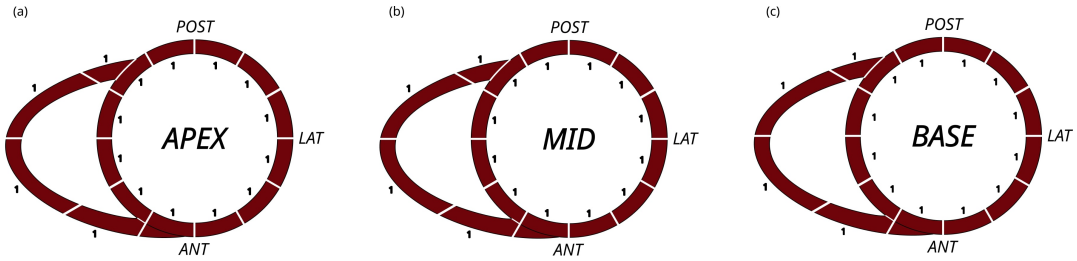

Figure 3.23: Cross-sectional analysis of the heart at three levels: (a) apex, (b) mid, and (c) base, each divided into 16 segments at 30-degree intervals. The correlation coefficients are displayed adjacent to each segment. These coefficients compare the results of running patient A's data twice using the advanced algorithm with automatic median axis calculation. The coefficients were calculated using 100 random points per segment.

Algorithm	*Range (m)*			*Volume (m^2)*
	X	Y	Z	
Original	0.1160	0.0799	0.0613	$2.9188 \cdot 10^{-4}$
New	0.1173	0.0799	0.0613	$2.9156 \cdot 10^{-4}$
Ratio	0.998	1	1	1.001

Table 3.1: Dimensional comparison of models created using the original and new 3D rendering algorithms

been entirely automated in the new algorithm, eliminating the need for user intervention and potential errors. An increase in the 'Other' section of the table for the new algorithm comes from the additional saving process, as it stores more data for later visualization purposes. Although a total decrease of 2.6 minutes may seem marginal for a model with four views, the performance gains are substantial when scaling to multiple or full-heart models. It is also noteworthy that the original algorithm's execution for patient A was conducted by an experienced user familiar with the code's intricacies. For an inexperienced user, the processing time could be significantly longer, with an increased likelihood of errors during manual segmentation.

	Original Code (sec)	*Advanced Code (sec)*	*Percentage Change*
Manual Pre-Segmentation	*93*	*0*	*-100%*
Median Axes & Wall Detection	*35.17*	*32.25*	*-8.3%*
LV & RV Rendering	*355.2*	*283.67*	*-20.1%*
Other	*20.56*	*35.61*	*+73.2%*
Total	*∼504*	*∼351*	*-30.4%*

Table 3.2: Comparison of execution times for different sections and total times between the original and advanced code implementations, using the same dataset.

3.5.5 3D Visualizations of EWI

In this section, examples from different visualization methods are presented to provide a better understanding of the available plotting options for 3D rendered EWI models. In addition to standard orthogonal cropping along the X, Y, or Z axes, as shown in Figures 3.20 and 3.19e(i), alternative methods offer more flexible approaches. One option involves the intersection of two orthogonal planes to create 3/4 models, as illustrated in Figure 3.24, which is particularly useful for full heart models with internal structures. Another method allows for the use of arbitrarily defined planes in space, enabling the user to cut the model along planes that are not parallel to the axes. Figure 3.25 showcases a ventricular model divided into three sections using this approach, where the user defines three vertices on the model to generate the cutting plane.

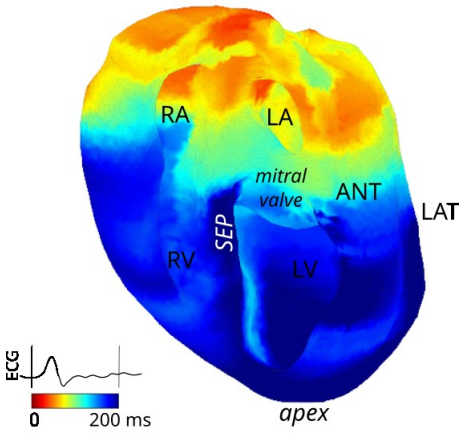

Figure 3.24: Full heart model cropped using orthogonal planes to show internal structures like the septum and mitral valve for better visualization.

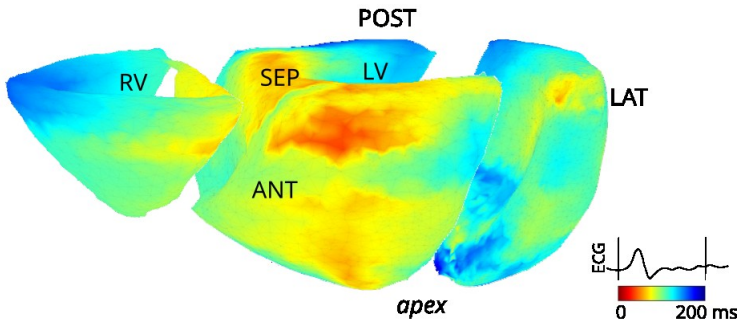

Figure 3.25: 3D ventricular model cropped into three separate sections using arbitrarily defined planes in space, enabling the user to cut the model along planes that are not parallel to the axes.

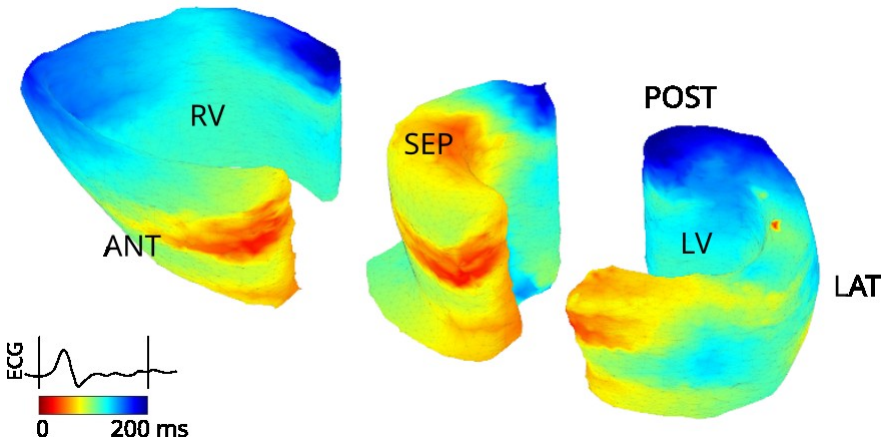

Figure 3.26: Ventricular model with its right ventricular, septal, and left ventricular walls separated.

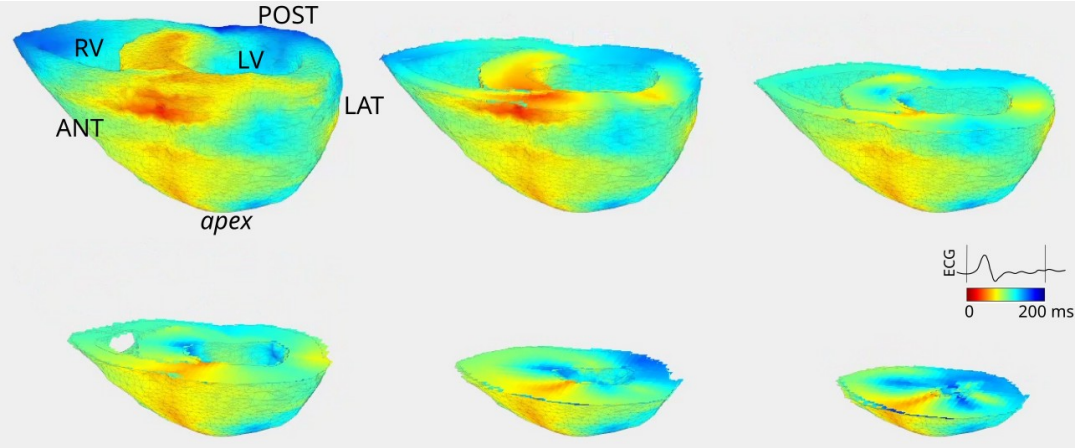

Figure 3.27: Six frames extracted from a downward cropping video of a 3D ventricular EWI model showing activation details in the myocardium walls.

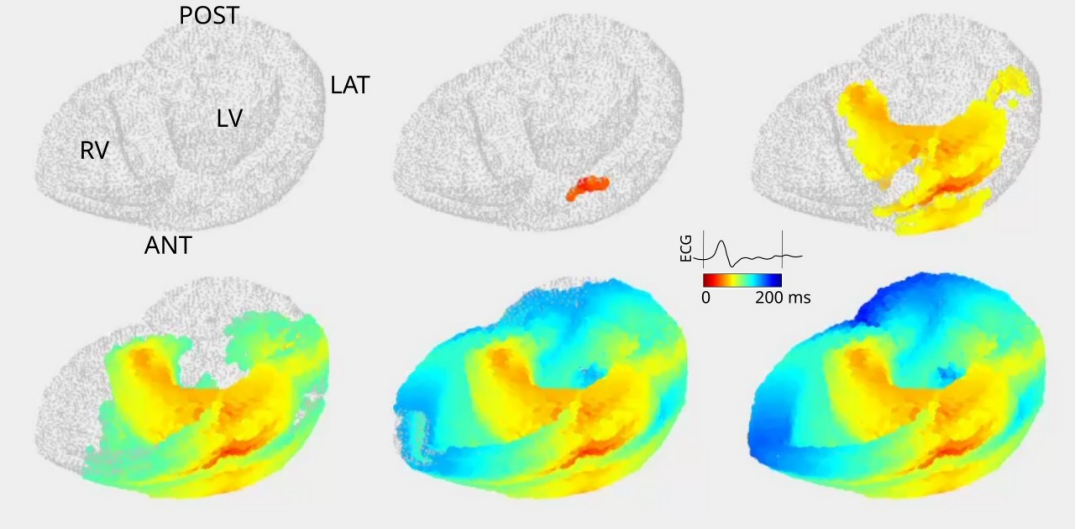

Figure 3.28: Six frames extracted from an activation sequence video of a 3D ventricular EWI model showing the propagation of the activation in the myocardium walls.

While the above cropping options offer great flexibility for visualizing different heart walls, a predefined separation option is also available for more straightforward analysis. The 'LV-RV Separation' toggle can be selected during rendering to automatically divide the RV, septum/apex, and LV walls into three separate 3D matrices (Figure 3.15c). These can be easily accessed from the drop-down menu in the visualization window (Figure 3.15d), making it easier to inspect the internal chamber walls, especially in cases where simple visualization might not adequately present these details. Figure 3.26 shows one such ventricular model where the RV, septal, and LV walls are separated. This works similarly for atrial and full heart models.

Video files of sequential downward cropping on the Z-axis can be generated, as shown in Figure 3.27, where six frames are presented for reference.

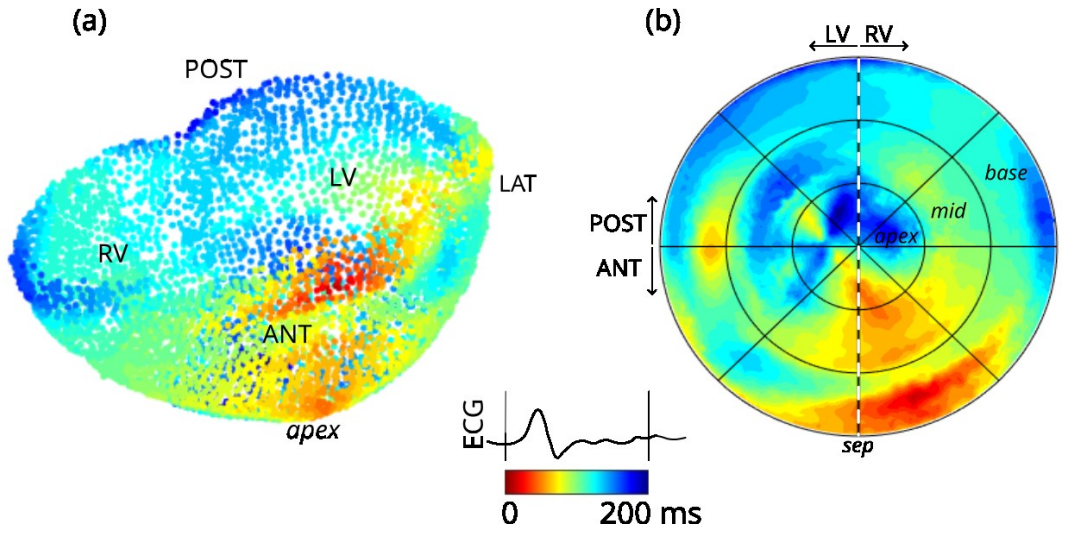

Figure 3.29: (a) Outer shell extracted from a bi-ventricular EWI model, (b) two-dimensional bullseye plot in generated from the extracted shell. The myocardium is divided into a total of 24 segments with three circles to separate the apex, mid, and basal planes. The septum is marked with a white dotted line on the bullseye plot.

This feature allows for quick visualization of integral activations of the myocardium walls without the need for manually cropping the model at different Z levels. Additionally, a video of the sequential activation of the model can be created and saved, offering a clearer understanding of the propagation of activation across the myocardial walls. Figure 3.28 displays six frames from an activation sequence. The user can customize the frames per second and video duration, providing flexibility to control the level of detail displayed in each frame.

Lastly, Figure 3.29a shows the outer shell extracted from a bi-ventricular EWI model, which was used to generate the two-dimensional bullseye plot in Figure 3.29b. The myocardium is divided into eight segments with each segment further split into three regions representing the apex, mid, and basal planes for a total of 24 segments. The septum is marked with a white dashed line. Bullseye plots are widely used in clinical cardiology, and because the algorithm used here is adapted from ECGi data, it enables a more direct comparison between 3D EWI and ECGi data. Various statistical parameters, such as minimum, maximum values, and standard deviation, can be calculated for each segment. Additionally, given the ability to isolate the septal and left ventricular walls, a bullseye plot can also be constructed specifically for the left ventricle, providing further information about the septal region that is not captured here.

Chapter 4

3D Registration of EWI with CT Models

4.1 Introduction

In cardiac imaging, 3D registration plays a critical role in integrating anatomical and functional data from different imaging modalities. By registering models such as Electromechanical Wave Imaging (EWI) and Computed Tomography (CT), clinicians can achieve a more accurate visualization of the heart's structures and electromechanical function. While CT provides detailed anatomical information, EWI captures functional data related to electrical activity. Fusing these datasets offers a comprehensive view of both the anatomy and electromechanical behavior of the heart, leading to more precise diagnosis and treatment planning.

Starting with a literature review of current 3D imaging techniques and commonly used registration algorithms, this chapter details the methodology developed for 3D registration of EWI models with the patient's anatomical data from CT scans. The goal of this integration is to enhance arrhythmia localization by improving the anatomical accuracy of the rendered images. Finally, results from applying the methodology to data from Patient C are presented, followed by a discussion of the findings.

4.2 Introduction to 3D Imaging Techniques

In modern medical imaging, multiple modalities are often employed to provide complementary information for a more comprehensive understanding of anatomical and physiological structures. Two of the most prominent imaging techniques used for these purposes are Computed Tomography (CT) and Magnetic Resonance Imaging (MRI). Each modality brings unique strengths and limitations, particularly in the context of complex procedures like arrhythmia treatment, where high anatomical accuracy is crucial.

Beyond individual imaging modalities, the growing importance of 3D surface registration techniques enables the fusion of data from multiple sources to enhance the quality and interpretability of medical images. 3D surface registration aligns point clouds or surfaces derived from different scans, allowing clinicians to combine structural and functional data from multiple imaging methods. This is particularly relevant in multimodal imaging (MMI), where registration helps mitigate discrepancies caused by different

resolutions, imaging techniques, or physiological factors like respiratory motion. Through techniques like the Iterative Closest Point (ICP) algorithm and its non-rigid variants, 3D registration ensures the alignment of data sets, enabling more precise visualization and better-informed therapeutic decisions, especially in cardiac imaging.

This section gives an overview of the technical aspects of CT and MRI, their applications in arrhythmia treatment, and introduces the concept of 3D surface registration as a crucial step in multimodal medical imaging. This is a crucial step for understanding how these methods are applied in specific contexts, such as cardiac imaging, where precision and integration of data from various modalities are essential for successful outcomes.

4.2.1 Computed Tomography

Computed Tomography (CT) is a well-established and widely utilized imaging modality that generates detailed cross-sectional images of internal body structures. By acquiring multiple tomographic slices, CT allows for the reconstruction of a 3D representation of the patient's anatomy. The core principle of CT imaging is rooted in conventional X-ray technology. However, unlike 2D X-rays, where the source is static, in CT the X-ray beam rotates around the patient, enabling the collection of a comprehensive set of images as the patient lies inside the scanner. These rotational images are processed by specialized software to generate 2D tomographic slices, which are subsequently assembled to create a 3D model of the region of interest.

During a CT scan, the patient remains stationary on a motorized table that moves incrementally through the center of a donut-shaped scanner. The X-ray tube continuously rotates around the body, capturing images in a spiral pattern as it acquires data along the entire length of the target anatomy. To ensure clear, motion-free images, the patient must remain completely still throughout the procedure. Additionally, metallic objects must be removed to prevent image artifacts caused by their interference with the X-ray beam.

The basic mechanism underlying CT imaging is similar to that of traditional X-rays. X-rays, a high-energy form of electromagnetic radiation, pass through the body and interact with tissues of varying densities. Denser tissues, such as bone, absorb more X-ray energy and consequently appear brighter (whiter) on the final image, while less dense tissues, like air-filled cavities, absorb less and appear darker (black). As the X-rays exit the body, detectors on the opposite side capture the transmitted rays, and these signals are processed to reconstruct the final tomographic image[87, 88]. Figure 4.1 shows an example thoracic CT scan from three different orthogonal views where the chest, lungs, spine, and rib cage can be seen.

To enhance the visualization of soft tissues, which often absorb minimal X-ray energy and may therefore be difficult to discern, contrast agents are employed. These agents, which absorb a higher amount of X-rays, increase the visibility of specific anatomical structures, such as blood vessels or soft tissues. Contrast agents are generally safe for use in humans and can be administered intravenously, orally, or rectally, depending on the diagnostic requirement. The choice of contrast agent is determined by the nature of the examination and the specific area of the body being imaged. Several factors

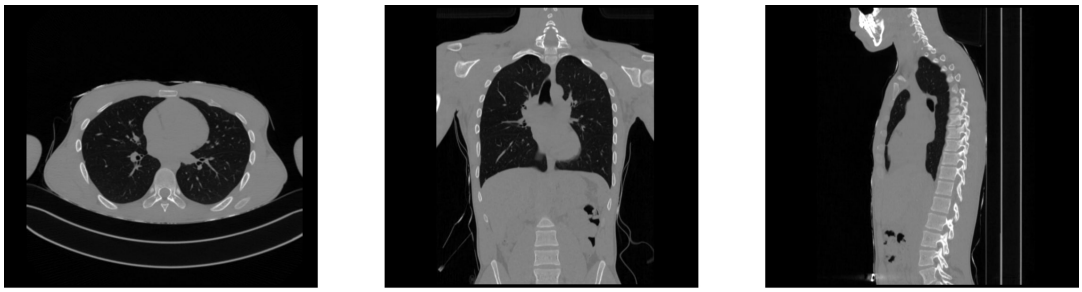

(a) (b) (c)

Figure 4.1: Three orthogonal views of a patient's thorax from a CT scan. (a) Transverse view showing a cross-section of the chest at the level of the lungs. (b) Coronal view displaying a frontal slice of the thoracic cavity, including the lungs, heart, and spine. (c) Long axis view providing a side profile of the chest, illustrating the lungs, heart, spine, and rib cage.

can influence CT image quality, including the specifications of the scanner, the methodology employed for image acquisition and reconstruction, and the use of contrast media[89].

Advances in CT technology, particularly the significant improvements in spatial and temporal resolution, have made cardiac CT a valuable tool in clinical cardiology. Modern CT systems enable non-invasive characterization of coronary arteries, facilitating CT angiography for the diagnosis of coronary artery disease. Cardiac CT is now utilized for a variety of applications, including the anatomical assessment of the heart and surrounding vasculature, as well as 3D post-processing to extract detailed geometric data for surgical planning. In cardiac resynchronization therapy, for example, CT imaging provides high-resolution, 3D maps that assist in the optimal placement of pacemaker leads, ensuring precise intervention. Additionally, CT aids in the identification of structural abnormalities, such as tumors, valvular diseases, or congenital defects[90].

Despite its many advantages, there are several limitations associated with CT imaging. Since CT relies on X-rays, patients are exposed to a considerable amount of radiation, making it less suitable for repeated examinations or for use in certain populations, such as pregnant women. The administration of contrast agents, particularly those containing iodine, carries the risk of allergic reactions or, in rare cases, temporary kidney dysfunction. Although contrast agents are generally safe, their use must be carefully considered in individuals with pre-existing renal conditions. Additionally, CT imaging is not uniformly accessible in all regions, and the high cost of the equipment and associated procedures can be a barrier to widespread adoption in certain healthcare settings[91, 92].

4.2.2 Magnetic Resonance Imaging

Magnetic Resonance Imaging (MRI) is a non-invasive imaging technique that leverages the magnetic properties of atoms within the human body to generate highly detailed images of internal organs and tissues. Unlike Computed Tomography (CT), which relies on ionizing radiation, MRI uses powerful

magnetic fields and radiofrequency (RF) pulses to produce high-contrast images, especially useful for soft tissue differentiation. This makes MRI particularly valuable in clinical scenarios where detailed soft tissue contrast is required, such as the assessment of brain, musculoskeletal structures, or cardiovascular tissues. MRI scans are capable of imaging any region of the body, including the head, chest, abdomen, and extremities, and can be performed in various planes. Like CT, MRI produces 2D slices that can be compiled into 3D models using post-processing software. In cardiovascular medicine, MRI is particularly beneficial for evaluating conditions like cardiomyopathies, tissue damage, valve dysfunction, and heart muscle diseases, including heart failure and cardiac tumors[93].

The imaging process is somewhat similar to that of CT, though with key differences. During an MRI scan, the patient is placed on a table that is moved into the bore of the scanner. MRI scanning can last from 20 minutes to over an hour, depending on the area being imaged and the protocol used. As MRI is highly sensitive to motion, it is critical that the patient remains completely still throughout the scan to avoid artifacts or blurring. Additionally, due to the strong magnetic fields involved, it is imperative that patients with metallic implants or external devices inform their physician, as such devices can interfere with the magnetic field, degrade image quality, or pose safety risks[94].

The fundamental principle of MRI lies in the interaction of water molecules within the body with the magnetic field. The nucleus of hydrogen atoms (which are abundant in water and fat) contains a single proton, making them ideal for MRI. In their natural state, these protons spin around their axes in random directions. However, when exposed to the strong magnetic field generated by the MRI machine (typically between 0.5 and 1.5 Tesla, though higher-field systems are also in use), the protons align along the field. A radiofrequency (RF) pulse is then applied, causing the protons to momentarily deviate from their alignment. As the RF pulse is turned off, the protons return to their aligned state, releasing energy in the process. The time it takes for the protons to realign, and the amount of energy released, differs among various tissue types, allowing MRI to distinguish between different structures based on these characteristics[95].

MRI also offers several specialized imaging techniques, which are particularly useful for cardiac imaging. Cardiac MRI (CMR) can assess cardiac morphology, tissue composition, and function with high precision, making it an essential tool for evaluating heart conditions such as arrhythmias, cardiomyopathies, and ischemic heart disease. Techniques such as prospective ECG-gating are employed to manage irregular heart rhythms like atrial fibrillation, while real-time cine imaging and motion-corrected late gadolinium enhancement (LGE) help in visualizing myocardial scarring and fibrosis during the cardiac cycle. Perfusion MRI can estimate blood flow, while diffusion-weighted MRI tracks water movement within cells, both of which are highly useful for assessing cardiac tissue integrity and function[96].

Although MRI is highly advantageous for soft tissue imaging and does not expose patients to ionizing radiation, it has certain limitations. The procedure is lengthy and can be uncomfortable, particularly for patients with claustrophobia, though open MRI systems have been developed to mitigate

this issue. Additionally, the strong magnetic fields pose safety concerns for patients with metallic implants, such as pacemakers or metal stents, as these devices may move, heat, or malfunction in the magnetic environment. MRI is also associated with loud noise due to the rapid switching of magnetic gradients, though ear protection and panic buttons are typically provided for patient comfort. Another consideration is the use of contrast agents, such as gadolinium-based compounds, which enhance image contrast by altering the magnetic properties of nearby tissues. While generally safe, gadolinium-based agents can pose risks for individuals with kidney disease and are typically avoided in pregnant women and dialysis patients. Side effects of contrast administration, though rare, may include headaches, nausea, or dizziness[97]. Lastly, MRI is not as widely available in some regions and is more expensive than CT, which may limit its accessibility. The high costs arise from equipment acquisition and staffing expenses. Due to these factors and a lack of domain expertise, MRI is generally restricted in developing nations[98, 99].

4.3 Introduction to 3D Surface Registration

Many applications nowadays make use of 3D scanning technology. This is not only limited to medical and biomedical applications but it extends to other sectors like roads, autonomous vehicles, buildings etc. with different technologies and software algorithms developed depending on the application. These methods result in a set of points that describe the geometry of an object or scene in three-dimensional space, typically referred to as point clouds. A point cloud is essentially a collection of data points represented by their coordinates in a 3D coordinate system (x, y, z). Additional properties such as color or surface normals can further describe the cloud. Point clouds are a digital representation of a physical object or environment and can be transformed into more structured forms such as meshes or surfaces[100]. Common surface reconstruction techniques include Delaunay triangulation and alpha shapes, which can interpolate a point cloud into a continuous surface without additional information such as surface normals or scanner information[101].

A single object can be scanned and represented digitally from multiple different locations or positions in time resulting in several point clouds. The process of finding a point-to-point correspondence between two or more point clouds and applying transformations to align one with the other is called surface registration or simply registration. A transformation can be either rigid (translation and rotation), or non-rigid (scaling, shearing). Over time, numerous registration techniques have been developed, including iterative methods, feature-based techniques, and more recently, deep learning algorithms[102].

One of the most commonly used techniques for registration is the Iterative Closest Point (ICP) algorithm, introduced in 1992. ICP is a general-purpose method known for its computational efficiency and accuracy in 3D shape registration. However, ICP is restricted to rigid transformations. The growing need for locally accurate matching, especially in fields like medical imaging and autonomous navigation, has driven the development of more flexible

algorithms such as affine and non-rigid ICP (NRICP) methods. These types of algorithms have found numerous applications in the automotive industry with autonomous vehicles, the education and entertainment sector and most relevant to the medical imaging field with multi modal imaging (MMI). Multimodal refers to the combination of two or more imaging modalities with the aim of deriving complementary information. In MMI, point clouds obtained from different imaging modalities—such as CT, MRI, or ultrasound—must be aligned. MMI poses unique challenges, as point clouds generated by different imaging technologies can represent the same structure in different ways due to varying resolutions, imaging techniques or physiological conditions.

This chapter introduces the ICP and NRICP frameworks, with a particular focus on the optimal step nonrigid ICP algorithm. Additionally, it presents some of the challenges and applications of MMI, especially in medical contexts. This background provides the foundation for later discussion on how these methods are used to align 3D data from EWI and CT in cardiac imaging.

4.3.1 Iterative Closest Point (ICP)

Given two distinct point clouds, the goal of ICP is to find a translational and rotational transformation matrix that best aligns the two shapes. Assuming one surface defines the fixed master set and the other one is the source, the best transformation matrix is the one that minimizes the distance between them. Mathematically, given two finite sets M and S that contain N_M and N_S points respectively, what is the rigid transformation matrix that minimizes the distance between the two sets via a mean-square distance metric?

A standard ICP algorithm proceeds iteratively. It begins with an initial guess of the transformation and refines this guess step by step until an error metric is minimized. The general ICP algorithm can be broken down into six distinct steps:

- *Selection of some set of points in one or both clouds*: A subset of points is chosen from the source cloud S (or from both S and M) to reduce computational load.
- *Matching these points to samples in the other mesh*: Each selected point in S is matched to the nearest point in M based on a chosen distance metric, typically the Euclidean distance.
- *Weighting the corresponding pairs appropriately*: Weights are assigned to each matched pair based on a specific metric, such as the distance between corresponding points or the confidence in the match. The aim is to give higher weights to more reliable correspondences, improving the overall alignment accuracy.
- *Rejecting unreliable point pairs*: Pairs are rejected based on specific criteria. This often includes removing correspondences where the distance between matched points exceeds a threshold, as these are likely to represent outliers or noise.

- *Assigning an error metric based on the point pairs*: The error metric is computed. In the basic ICP algorithm, this is typically the mean squared distance between corresponding points.
- *Minimizing the error metric*: The rigid transformation (translation and rotation) is updated iteratively to minimize the computed error. The algorithm continues refining this transformation until the error is reduced to an acceptable level, or a predefined convergence criterion is satisfied.

While numerous variants exist, all of them operate by modifying one or more of the six steps outlined above[103, 104].

Although ICP has been widely adopted, it has several limitations. Standard ICP often exhibits slow convergence, especially when the initial guess of the transformation is poor. It is also highly sensitive to outliers, incomplete data, and partial overlaps, which can lead to inaccurate alignments. Symmetric surfaces present additional challenges for ICP, as the algorithm may struggle to identify the correct correspondences, leading to improper alignment. Furthermore, ICP is unable to handle non-rigid transformations (e.g., scaling or shearing), which limits its applicability in cases where the point clouds differ in scale. Despite the development of various ICP variants to address these limitations, many adaptations are designed for specific applications, resulting in inconsistent performances across different use cases[105, 106].

4.3.2 Non-Rigid Iterative Closest Point (NRICP)

In the field of surface registration, several improvements have been proposed to enhance the traditional Iterative Closest Point (ICP) algorithm. Classic ICP assumes rigid body transformations, which limits its application in cases where non-rigid or deformable surfaces are involved. To address this, Non-Rigid Iterative Closest Point (NRICP) algorithms modify the error minimization process to accommodate local deformations and flexible transformations. Figure 4.2 illustrates an example of non-rigid 2D point cloud registration, where blue points are progressively registered to red points using translations, rotations, and affine transformations. The frames demonstrate the progression of the registration process, with each iteration adjusting the points to better match the target surface. By allowing for non-linear adjustments, these algorithms better handle the complex geometries often encountered in medical imaging applications, where anatomical structures like the heart undergo localized shape changes due to motion or deformation[107].

Numerous variations of NRICP exist, each tailored to specific challenges in high-dimensional, deformable datasets. For instance, approaches that leverage local statistical models can mitigate the high dimensionality problem in large datasets, improving accuracy in local deformations[108]. Other adaptations, such as vertex-level affine transformations and the incorporation of local smoothness constraints, allow for more realistic modeling of surface deformations[109]. Moreover, several non-linear registration algorithms utilize the ICP framework, essentially reducing the problem to identifying point-to-point correspondences and applying transformations between surfaces[110]. These advancements have found applications in various domains, including

facial recognition and biomedical surface registration, each offering distinct advantages and limitations. One specific algorithm that is highly relevant to this thesis is the Optimal Step Nonrigid ICP Algorithm[111]. This algorithm is characterized by several key features that make it ideal for cardiac imaging applications:

- *Non-Rigid Local Deformations*: The algorithm allows for flexible, localized transformations of the template surface or point cloud to accommodate the deformable nature of cardiac structures.
- *Iterative Stiffness Reduction*: Initially, the algorithm permits global transformations and gradually refines them to become increasingly localized, which is critical for capturing fine-scale anatomical details.
- Optional Initial Rigid Registration: To enhance robustness, the NRICP can perform an initial rigid alignment using standard ICP before applying non-rigid deformations, improving the overall accuracy of the registration.
- *Bi-Directional Distance Metric*: By employing a bi-directional distance metric, the algorithm encourages the template surface to fully cover the target surface, minimizing unregistered regions.
- *Handling Missing Data*: The NRICP algorithm is designed to manage incomplete target surfaces, such as those with missing or corrupted regions, by ignoring points at the boundaries of the target surface.
- *Landmark Integration*: Optional use of anatomical landmarks allows for further refinement, making the algorithm adaptable to cases where certain known reference points can be leveraged for more accurate registration.

The algorithm operates by iteratively deforming a template surface to match a target surface. It begins by identifying a preliminary set of correspondences through a nearest-point search. These correspondences are then used to calculate an optimal deformation for the template. This process is governed by a stiffness parameter, which gradually decreases as iterations progress, allowing the template to better conform to the target surface over time. During each iteration, the algorithm finds corresponding points between the deformed template and the target by identifying the nearest points on the target for each vertex of the template. Once the correspondences are established, the algorithm computes an optimal deformation that minimizes the distance between corresponding points. This is achieved through a regularization term that ensures smooth and physically plausible deformations. The regularization is locally affine, meaning that each vertex in the template is allowed to undergo an affine transformation (translation, rotation, scaling, or shearing). Importantly, the algorithm minimizes the difference in transformations between neighboring vertices, ensuring that the deformations remain smooth and consistent across the surface. Figure 4.3 shows an such example of 3D surface registration, where the red source surface demonstrates improved alignment post-registration.

In cardiac imaging, the Optimal Step NRICP algorithm is particularly advantageous because of its ability to handle incomplete or noisy data, which

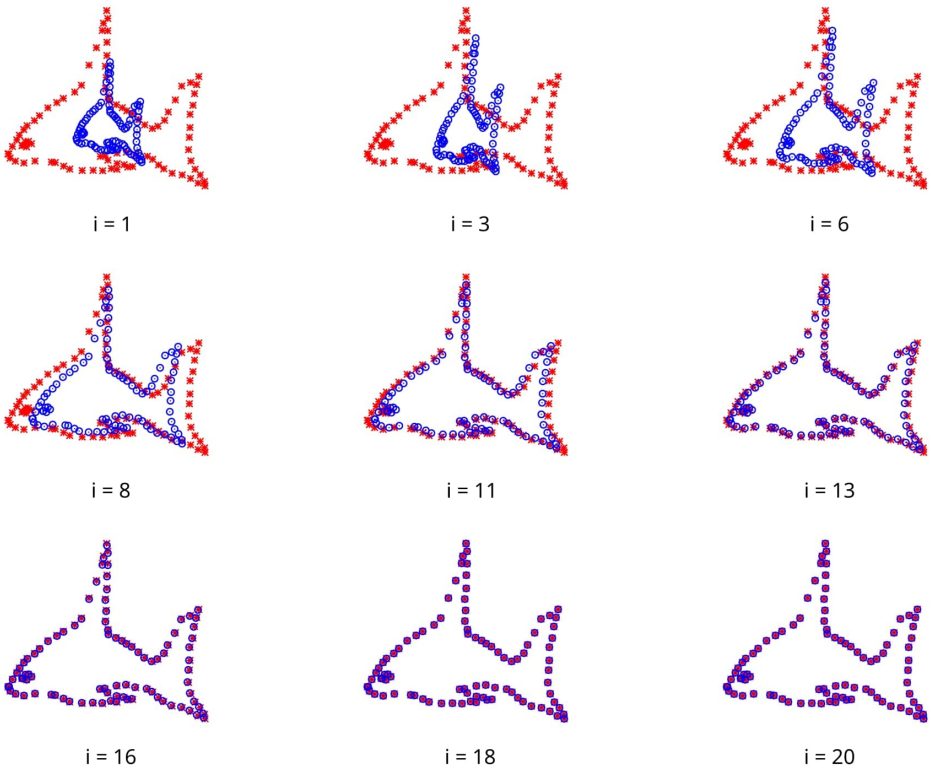

Figure 4.2: Example of non-rigid 2D point cloud registration. The blue points are registered to the red points using a combination of translations, rotations, and affine transformations. The frames show the progression of the registration process, with i indicating the iteration number for each frame.

are common in real-world medical scenarios. For instance, surfaces derived from EWI may contain missing regions or artifacts, and the algorithm can account for these by ignoring edge correspondences. Furthermore, its optimal step approach makes it more efficient compared to traditional methods, leading to faster convergence and reduced computational overhead. This efficiency, combined with its robustness to poor initial alignment, makes this NRICP method an ideal choice for medical applications where pre-alignment may be difficult to achieve. The algorithm is readily available, provided by its authors, and implemented in MATLAB, which allows for easy integration into the research pipeline. The ability to handle non-rigid deformations is crucial when registering anatomical structures that undergo local shape changes, such as different phases of the cardiac cycle or pre- and post-operative scans. By incorporating non-rigid ICP into the workflow, this thesis aims to enhance the accuracy of EWI and CT data integration, leading to more reliable representations of cardiac anatomy and function.

4.3.3 Applications and Challenges of Multimodal Imaging

Multimodal medical imaging registration is a critical tool in clinical practice, enabling the integration of data from two or more imaging modalities into a single 2D image or 3D volume. This combination provides more comprehensive information, enhancing the interpretability of the images by leveraging

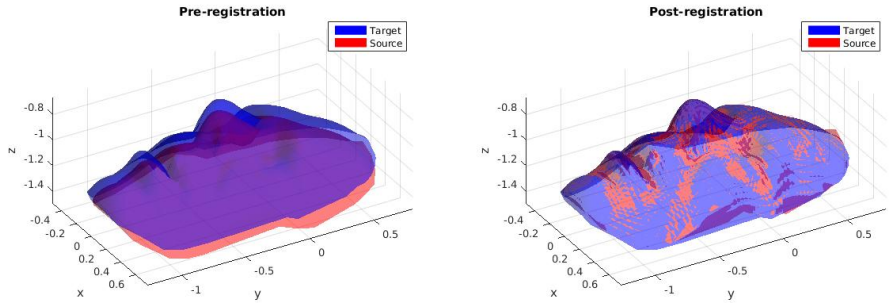

Figure 4.3: 3D surface registration example showing pre- and post-registration alignment of two datasets. The blue surface represents the target, and the red surface represents the source. (Left) Pre-registration: the source and target surfaces are misaligned. (Right) Post-registration: the source surface has been aligned with the target, demonstrating improved surface correspondence.

the strengths of each modality. For instance, CT and MRI can be co-registered to merge the detailed anatomical structure of bones from CT with soft tissue information from MRI, providing a more complete representation of patient anatomy. Such composite images are particularly beneficial for therapy planning, where detailed anatomical and functional insights are necessary for accurate intervention[112]. One key application of multimodal imaging registration is in intracardiac mapping, which aids in guiding catheter ablation procedures for arrhythmias. By fusing CT or MRI with intracardiac maps, physicians can access enhanced anatomical detail, which is essential for complex operative sites. Commercial software solutions, such as CartoMerge, provide this capability by supporting multiple registration methods, including manual selection of corresponding points, the use of Iterative Closest Point (ICP) algorithms to minimize spatial discrepancies, and a hybrid approach combining both techniques[113]. These technologies offer direct surgical guidance during procedures, improving the precision of catheter placement and ablation. Multimodal registration also addresses challenges related to cardiac imaging, particularly in mitigating the effects of respiratory motion on the heart. Respiratory motion can introduce spatial inaccuracies by altering the heart's size and position. Correcting for this motion ensures more accurate imaging, which is crucial for diagnostic and therapeutic purposes.

In echocardiography, several fusion techniques have been proposed, particularly in combination with CT scans. One approach involves acquiring 3D echocardiographic volumes and registering them with CT data. An example of this is the registration of a coronary tree from CT with a 3D ultrasound volume of the left ventricle (LV) endocardial surface to locate coronary stenosis. This method helps refine the anatomical understanding of coronary pathologies. Similarly, techniques have been developed to align 3D ultrasound data with CT scans to improve visualization of the heart wall regions, addressing misalignment issues often encountered in 3D echocardiography. Promising results have also been shown in real-time alignment and visualization of 3D echocardiography with cardiac magnetic resonance (CMR) volumes during live scanning[114, 115, 116]. However, despite these advancements, 3D ultrasound imaging remains a specialized technique and has not yet been widely

adopted, particularly in lower-income countries, where the high cost limits accessibility.

Further techniques have been developed to align 2D transthoracic echocardiography (TTE) images with CT scans. These techniques involve temporally and spatially synchronizing the two datasets, aiming to match the ultrasound acquisition of one cardiac cycle with the corresponding phase in the CT data. While these images can either be fused or displayed side-by-side to provide additional structural information, they lack the intuitive understanding that a 3D volume can offer[117]. Although full 3D echocardiography might still be beyond reach in certain settings, 3D volume reconstruction from multiple 2D echocardiographic images could offer a potential solution.

Machine learning and neural networks are expanding the possibilities in this domain. For example, the Pix2Vox++ network framework facilitates single- and multi-view 3D object reconstruction[118]. Recent adaptations aim to reduce memory usage and computational complexity while enabling 3D anatomical reconstruction from standard 2D cardiac views. These approaches are making it feasible to generate 3D anatomical models from limited 2D data[119]. However, several limitations persist in the current methods. Many of these techniques are either highly specialized, too time-consuming, or not applicable to previously acquired datasets. While advances are continually being made, there is still a need for a more versatile and robust registration methodology. Ideally, such a method would not only be easily applicable in clinical settings but would also provide more comprehensive insights than simple geometric or spatial relationships, enhancing the diagnostic and therapeutic potential of multimodal imaging.

4.4 Methodology

A novel method was developed to achieve spatial registration of 3D EWI data with patient CT scans, allowing for the integration of 3D surface geometries from both modalities. This method starts by aligning the two 3D point clouds in space, followed by using a surface registration algorithm to morph the 3D EWI surface onto the CT scan. After successful registration, the transformed 3D EWI surface can be visualized. This process also allows for transferring activation data from the EWI onto the CT scan, providing a comprehensive view of electromechanical activity overlaid on anatomical structures.

4.4.1 Data Collection and Processing

A VTK file containing the segmented endocardium and pericardium from a previously acquired non-contrast chest CT scan for Patient C was available. The VTK file was imported into MATLAB for further processing and analysis.

4.4.2 Point Cloud Registration

The registration process assumes that the median axes of the left ventricle (LV) point clouds from both the 3D EWI data and the CT scans should be aligned similarly in space. Initially, the median axes of each point cloud are

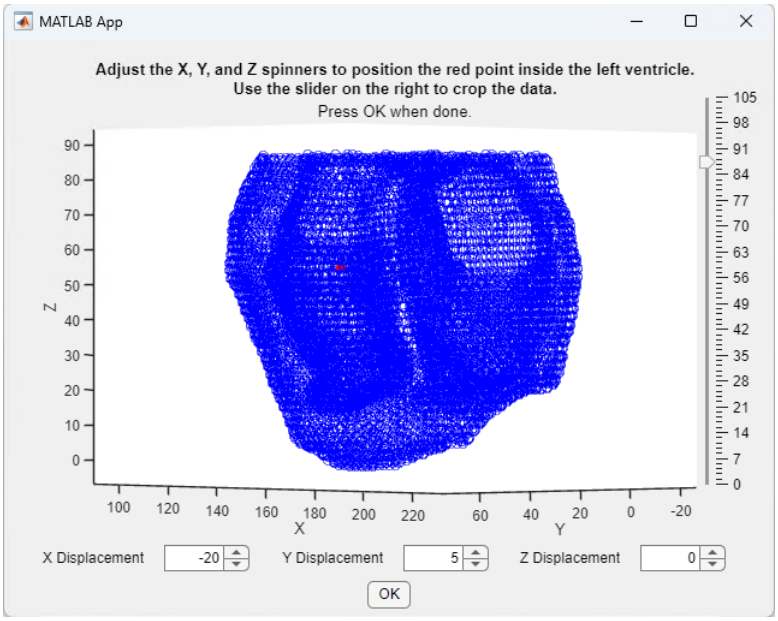

Figure 4.4: GUI for LV point extraction for CT model. This interface allows for manual adjustment of the X, Y, and Z displacements to position the red reference point inside the LV. The blue point cloud represents the CT scan data, with the red point indicating the ray origin point. The right-hand slider can be used to crop external structures.

calculated and used as references for registration. Both models are converted into point clouds for efficient manipulation and transformation in the subsequent steps. The CT model is cropped manually at the ventricular annulus, to remove any external heart structures, like the aorta, and leave only the ventricles (Figure 4.4). The 3D Isochrone model is referred to as the ISO model, and the CT scan model as the CT model.

If a 3D ellipsoid were to be fitted to the LV points in each point cloud, its major axis would represent the median axis of the LV. Since both point clouds define one continuous surface both internally and externally, a technique was developed to isolate internal LV points. This method extends the approach used for isolating the LV chamber in 2D isochrones for calculating the median axis, modified to handle 3D data. An origin point within the LV of each point cloud is defined, either automatically or manually (Figure 4.4). From this origin, a custom algorithm, based on the Triangle/Ray Intersection function in MATLAB[120], is used to extract internal LV points. This algorithm works by generating a vector (ray) from the origin toward each point in the cloud. For each triangle in the mesh (defined by its three vertices), the algorithm checks for intersections with the ray. The distance from the ray's origin to the intersection point is calculated, and the closest intersection is selected. To ensure accurate identification, the algorithm treats the mesh triangles as two-sided, and the ray's length is defined to include all relevant points. This step produces two matrices containing the LV point coordinates for each point cloud.

Figure 4.5 shows a simplified workflow of the isolation of the LV for both models. These points are then used with the ellipsoid fitting function from MATLAB's File Exchange[121] to fit an ellipsoid to the 3D data. The function

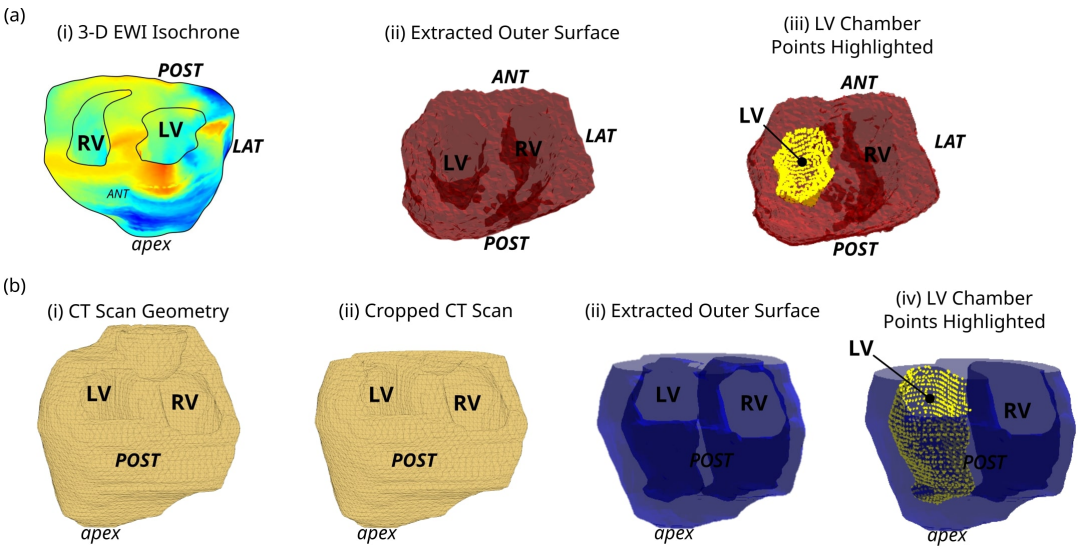

Figure 4.5: Workflow for LV Isolation. (a) ISO Model: (i) 3D EWI Isochrone of Patient C showing the full ventricular geometry, (ii) Boundary extracted from the EWI data, (iii) Extracted boundary with marked LV points identified using the Triangle/Ray intersection method. (b) CT Model: (i) 3D ventricular geometry extracted from Patient C's CT scan. (ii) Cropped CT model isolating the ventricular structures by removing external anatomy. (iii) Boundary extracted from the CT data. (iv) Cropped bi-ventricular shell showing extracted LV points marked with yellow dots.

provides key parameters such as the center coordinates and radii of the ellipsoid, with the largest radius representing the major axis of the LV. This axis is used as a reference for further registration and morphing processes to ensure anatomical accuracy.

4.4.3 Surface Registration

After calculating the major axes (long, middle, and short) for each model, they are aligned using the Iterative Closest Point (ICP) algorithm in MATLAB[122]. This step ensures consistent initial orientation of the models. It is important to manually scale the ISO model before registration. The transformation matrix obtained from this process is applied to the major axes and the ISO model itself for initial alignment. A 180-degree rotation may be necessary to properly align the ventricles, minimizing large-scale misalignments. If there is any residual misalignment, particularly in the right ventricle (RV), a custom MATLAB application allows interactive manual adjustments for fine-tuning (Figure 4.6). Figure 4.7 illustrates a streamlined workflow for the registration of ellipsoid axes and surfaces between the two models.

Next, a non-rigid ICP transformation is applied with the CT model as the fixed reference and the ISO model as the source. An initial global deformation is allowed, followed by iterations with reduced stiffness. After non-rigid transformation, the activation data from the ISO model is mapped onto the CT model using nearest-neighbor interpolation, enabling the visualization of point-wise data across the aligned models. The final registered models, along with the interpolated data, can then be visualized.

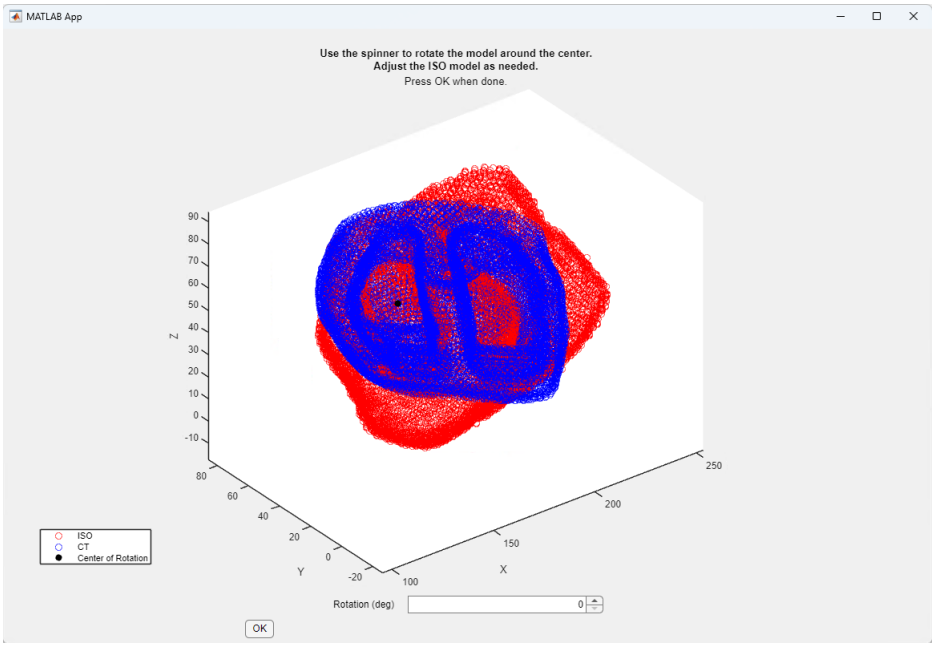

Figure 4.6: Custom GUI allowing for interactive adjustments to manually fine-tune the alignment between the 3D isochrone (ISO, in red) and CT scan (in blue) models after the initial transformation. The user can rotate the models around the center of rotation (black dot) to achieve better alignment, especially for correcting residual misalignment in the right ventricle (RV).

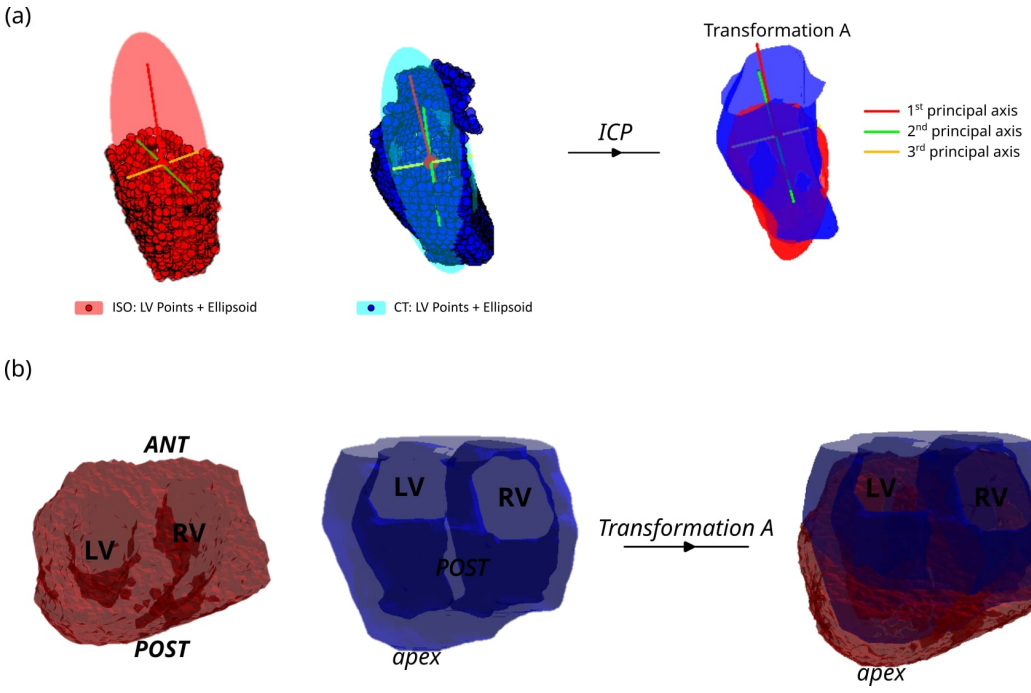

Figure 4.7: Workflow for 3D Shell Registration. (a) Both the ISO and CT models' LV points are fitted with ellipsoids, and the principal axes are calculated. This is followed by the Iterative Closest Point (ICP) transformation (Transformation A), aligning the principal axes of both models for registration. (b) Visualization of the 3D shell registration process, where the ISO shell (red) is transformed into the CT shell (blue), aligning both models' ventricular geometries through Transformation A.

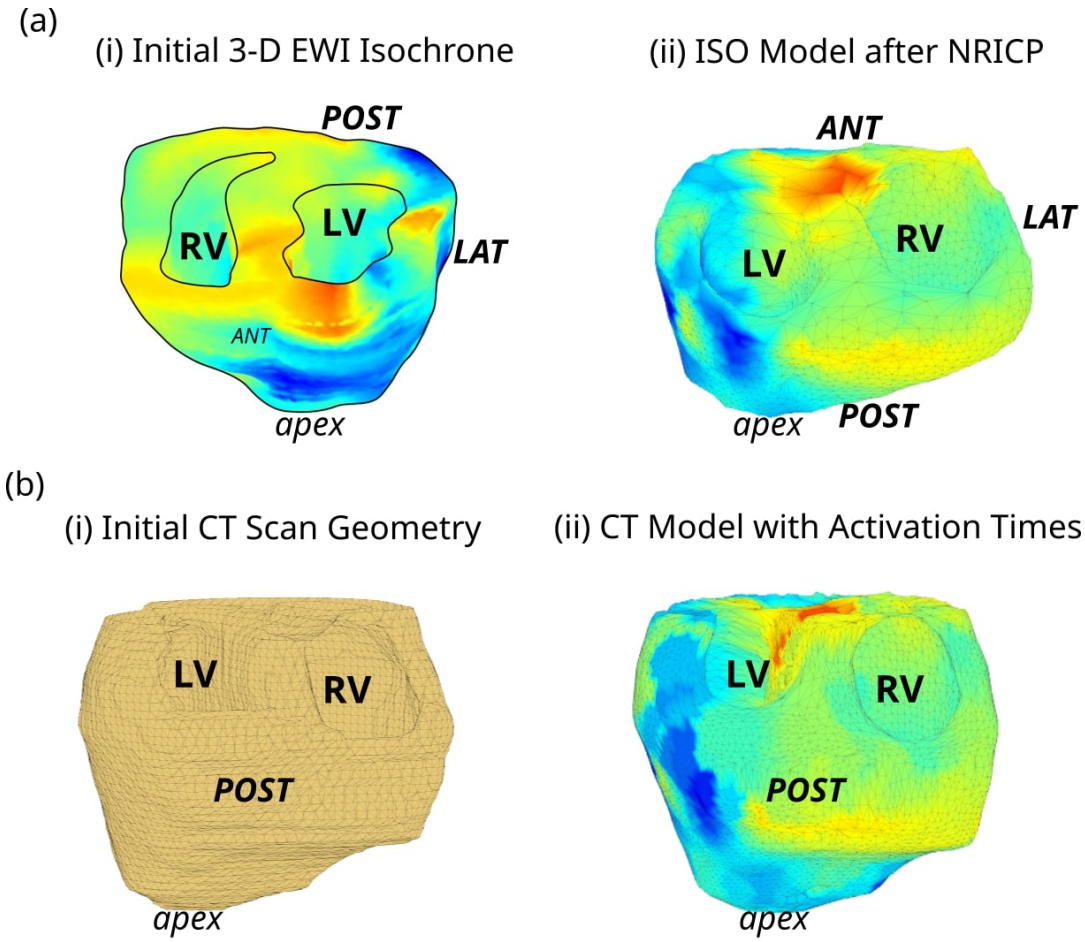

Figure 4.8: Non-Rigid ICP Transformation and Nearest-Neighbor Interpolation for Shell Registration. (a) (i) Initial 3D rendered Isochrone for Patient C, (ii) ISO model after applying the non-rigid ICP transformation. (b) (i) Initial cropped Patient C's CT model, (ii) CT model with nearest-neighbor interpolated activation data mapped from the transformed ISO model.

4.5 Results and Discussion

The registration results for Patient C are displayed in Figure 4.8. The updated geometry of the EWI map is presented in Figure 4.8(a)(ii), and the corresponding CT model, with interpolated activation data, is shown in Figure 4.8(b)(ii). This approach has demonstrated improved spatial accuracy in aligning 3D isochrones with CT data, serving as a promising first step toward multimodal imaging of EWI. Additionally, this method holds potential for further applications, such as integration with MRI data or intracardiac CT-based mapping. It is important to note that the CT model for Patient C reveals an overestimation of the right ventricular (RV) volume compared to the left ventricle (LV), despite no corresponding evidence in the patient's medical history. This discrepancy is likely due to manual segmentation of a non-contrast-enhanced CT scan, where the RV chamber volume has been overestimated.

There are several challenges in accurately registering 3D-rendered isochrones with CT data. The process may require further optimization to ensure consistent multimodal imaging integration, particularly as ventricular and atrial volumes obtained from CT scans may not always serve as reliable ground truths. Additionally, the manual scaling of the isochrones could be improved by utilizing scaling factors available in DICOM data, which would allow for more precise dimensional adjustments. Another limitation involves the non-rigid ICP algorithm, which was employed without using landmark points. Incorporating manually selected landmark points at specific locations, such as the walls of the standard apical 4-chamber view, could enhance the accuracy of the non-rigid ICP transformation. This refinement would potentially lead to more accurate registrations and better alignment between the EWI and CT data.

To build on this work, future developments could include integrating additional imaging modalities, such as MRI, to provide more comprehensive insights into cardiac function. Expanding the registration methodology to intracardiac CT mapping data would also enhance the versatility of this technique in clinical applications.

Chapter 5

Conclusions and Future Work

Cardiovascular diseases remain one of the leading causes of death globally. Arrhythmias are a type of heart condition that disrupt the heart's conductive system, leading to abnormal and irregular heart rhythms. There are many types and classifications of arrhythmias, some of which are more severe than others and require immediate medical attention. While immediate treatment may not always be necessary, certain cases demand drug therapies or more invasive procedures, such as ablation or device implantation. Early detection and accurate spatiotemporal mapping of arrhythmias are crucial for reducing the risk of fatal events and ensuring timely treatment.

In clinical practice today, the electrocardiogram (ECG) is the most commonly used non-invasive method for diagnosing and localizing arrhythmias, often supplemented by echocardiography for additional insights into heart structure and function. However, for more precise diagnosis, invasive electrophysiology (EP) studies are often employed, where catheters are inserted into the heart with the assistance of radiation imaging, to record intracardiac electrical activity directly. This approach remains one of the most reliable methods for diagnosing and treating arrhythmias, but it comes with inherent risks and limitations.

In recent years, pushing toward a non-invasive, widely accessible, and accurate localization technique, Electromechanical Wave Imaging (EWI) has emerged as a promising solution, building on the principles of echocardiography. EWI provides real-time, high-resolution 2D maps (isochrones) of the heart's electromechanical activity by tracking the mechanical deformations in the myocardium that are caused by electrical activation. Unlike traditional methods that focus solely on either electrical or mechanical aspects, EWI captures both, offering a more precise localization of arrhythmia origins without the need for invasive procedures. These 2D maps can then be combined to produce a 3D activation map, giving clinicians a more complete understanding of wave propagation across the myocardium.

While 2D EWI offers valuable slice-by-slice data, it has limitations in observing the continuous propagation of electrical activity. This can obscure critical patterns, such as the initiation and spread of ectopic beats. The previous algorithm for generating 3D electromechanical maps also faced limitations, particularly in usability and in being restricted to four predefined views, which limited the spatial coverage of the heart.

This thesis aimed to address these challenges by advancing the 3D rendering technique for improved arrhythmia localization. An enhanced 3D

rendering algorithm was developed, which not only overcame the limitation on the number of apical views but also integrated additional perspectives commonly used in echocardiography, such as the apical five chamber (A5C) and the right ventricular inflow tract (RVIT) views. Furthermore, the algorithm now supports full heart models, including additional structures like the mitral valve and the left ventricular outflow tract (LVOT), providing a more comprehensive and detailed representation of cardiac anatomy and function. To further refine the anatomical accuracy of these electromechanical maps, a 3D surface registration method was developed to integrate patient-specific CT geometries with the 3D rendered EWI data, allowing for a more personalized analysis. Additionally, the entire process has been made more accessible through the development of a user-friendly graphical interface.

The key findings from this research highlight significant improvements in spatial coverage and activation mapping accuracy. The resolution in previously under-sampled areas, such as the anterior septum and right ventricle, has been enhanced, leading to more detailed electromechanical activation patterns, particularly in complex arrhythmia cases. The ability to render multiple apical views has allowed for a more comprehensive sampling of the myocardium, which results in better spatial resolution and more precise activation maps.

The inclusion of structures such as the LVOT and mitral valve in the 3D models has provided a more accurate anatomical context, enabling more detailed visualization of their activation patterns. This added complexity could help clinicians gain a more holistic understanding of cardiac function. The development of a user-friendly graphical user interface (GUI) played a crucial role in this advancement, making the process more accessible. By integrating the GUI, the workflow for 3D rendering and data analysis has been streamlined, allowing for easier manipulation and visualization of complex 3D models. The GUI not only simplifies user interactions but also improves the practicality of this approach in clinical and research environments. Given that it is not limited to processing only EWI data but can also handle 'empty' 2D datasets to provide a 3D anatomical model, its flexibility extends beyond EWI. A simplified version of the GUI will be released in the future to provide additional usability for non-EWI cardiac modeling.

Another important achievement is the enhanced efficiency of the algorithm. The rendering process was simplified, reducing computational demands while maintaining accuracy. This optimization improved both usability and processing speed, allowing for quicker processing of the electromechanical and anatomical data while still maintaining high levels of precision in the visualization. The combination of the optimized algorithm and the GUI further contributes to making this approach more practical for real-world applications, where time and accuracy are essential.

Finally, the fusion of functional and anatomical data through the 3D registration of EWI maps with CT-derived models provided a more complete view of the heart's electromechanical behavior, improving arrhythmia localization and potentially leading to better treatment outcomes.

While this work made significant advancements, several limitations should

be acknowledged, which point to areas for future improvement. One inherent limitation of echocardiography-based approaches lies in the variability of image quality and patient anatomy. Since the accuracy of 3D-rendered localization heavily depends on these factors, the image resolution may sometimes fall short of providing precise spatial details, especially in patients with complex anatomical variations. The enhanced algorithm also necessitated more sophisticated interpolation techniques to manage sparse activation data, particularly in the RVIT region. While this refinement improved spatial resolution, it increased computational time, introducing a challenge in balancing efficiency with accuracy. Additionally, although the algorithm successfully incorporates RVIT data, manual adjustments were still required to correct alignment discrepancies. As a result, the visualization may not always be robust, and inconsistencies may appear in the final rendering, which affects the overall clarity of the activation map.

Another issue is minor misalignments in full heart rendering, especially at the basal points of the LV. These misalignments stem from the method's reliance on aligning only the apical points during registration, as well as from slight distortions caused by manual image acquisition. These factors can cause imperfections, such as small gaps or misalignments in the final 3D map and should be addressed in future versions.

In terms of surface registration, accurately aligning 3D-rendered isochrones with CT scan data presented its own set of challenges. The registration process between these modalities sometimes required additional refinement to achieve consistent, reliable integration of functional and anatomical data. Lastly, while CT scans provide detailed anatomical models, the volumes of ventricles and atria they capture may not always serve as reliable ground truths, potentially introducing discrepancies between anatomical and functional data sets.

To further advance the findings of this thesis, several promising directions could be explored. First, expanding the dataset to include a more diverse patient population, featuring varying arrhythmia types and heart geometries, would provide a more comprehensive validation of the algorithm. This would also allow for assessing its clinical relevance across a broader spectrum of cases, including more severe arrhythmias or anatomical abnormalities. Another important step would be refining the interpolation techniques. Developing more advanced algorithms that enhance spatial resolution, particularly in regions where data are sparse, while maintaining computational efficiency, could significantly improve the accuracy of non-invasive activation mapping. Further, incorporating additional short-axis and out-of-LV median-axis views into the rendering process could provide an even more detailed representation of the myocardium, filling gaps in the spatial coverage and reducing the likelihood of data interpolation errors.

Future steps also include the development of a similar algorithm tailored for 3D strain visualization during a single cardiac cycle. This feature will provide the ability to assess mechanical deformation and strain patterns in the myocardium, offering valuable insights into myocardial contractility and dysfunction. Although the initial work has begun, further refinements are needed to fully integrate strain visualization into the existing GUI framework and optimize the algorithm for accurate strain mapping.

Exploring the potential integration of the advanced 3D rendering algorithm with other imaging modalities, such as MRI or intracardiac echocardiography (ICE), could offer a more comprehensive understanding of the heart's electromechanical function. This multimodal approach may improve the precision of arrhythmia treatment strategies by combining the strengths of different imaging techniques. Finally, continuous improvements to the GUI could enhance user experience and reduce the manual adjustments currently needed for data alignment, making the algorithm more accessible and practical in clinical settings.

In conclusion, 3D-rendered EWI is a non-invasive method that provides an intuitive understanding of spatial relationships within the heart, facilitating precise localization of arrhythmogenic regions. The advanced 3D rendering algorithm proposed significantly enhances the spatial accuracy and efficiency of electromechanical activation mapping, while integrating EWI data with CT-derived anatomical models helps with accurate geometrical detail. These improvements offer considerable clinical potential in diagnosing and treating cardiac arrhythmias. The incorporation of multiple apical views and the LVOT into the 3D model marks a significant advancement by adding greater anatomical and functional detail. The model enhances both diagnostic precision and usability, especially in complex cases where conventional 2D methods fall short. Furthermore, the inclusion of mitral valve activation introduces an additional layer of diagnostic accuracy, allowing for more comprehensive assessments of arrhythmogenic regions. Although challenges remain, this work represents a pivotal step toward more precise arrhythmia localization. With further refinements and broader validation, this algorithm could become a valuable clinical tool, offering deeper insights into arrhythmogenic regions and guiding more effective therapeutic interventions.

Appendix A

Detailed View of Figure 3.13

This appendix presents magnified sections of Figure 3.13 to offer a clearer and more detailed view of key areas of interest.

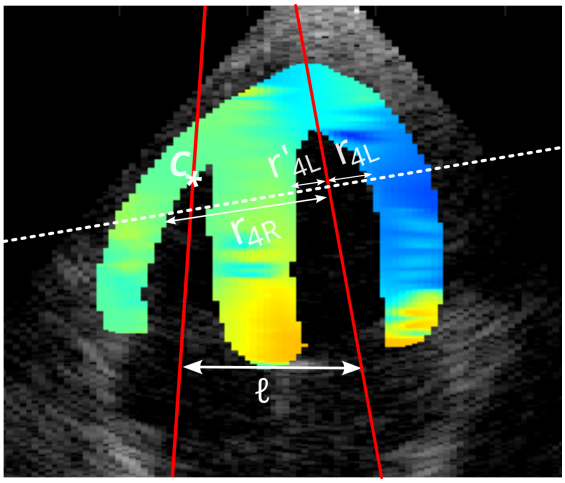

Figure A.1: Zoomed in version of the 4Ch. 3o'clock view. The median axis is indicated with a solid red line, while the dotted white line corresponds to the considered transverse slice. The radial positions of the walls (e.g., r_{4L}, r'_{4L}, r_{4R}) and the activation time values are extracted.

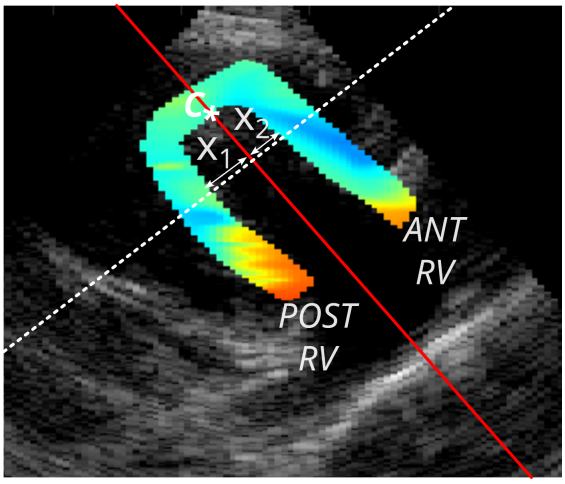

Figure A.2: Zoomed in version of the RVIT view. The median axis is indicated with a solid red line, while the dotted white line corresponds to the considered transverse slice. The positions of the walls (e.g., x_1, x_2) and the activation time values are extracted.

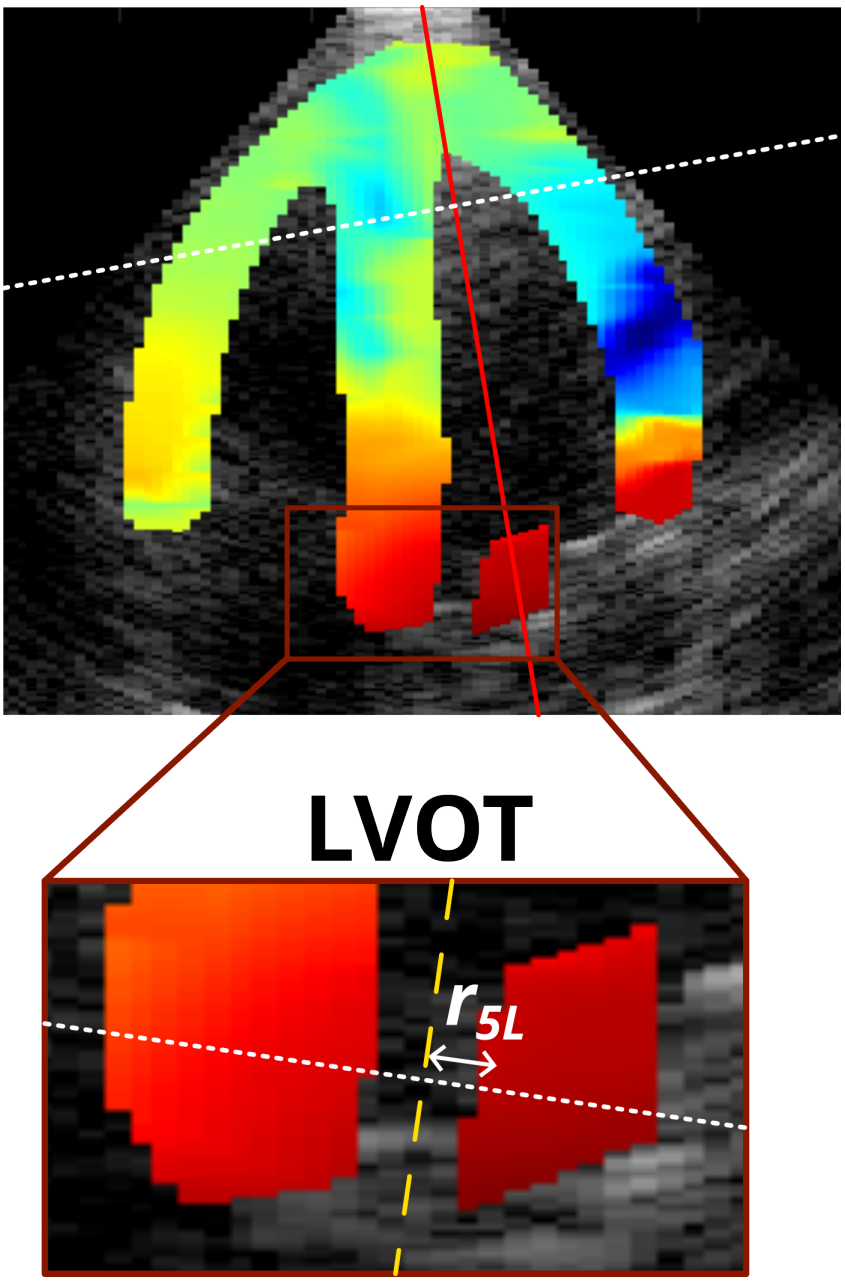

Figure A.3: Zoomed in version of the 5Ch. view with the LVOT region enlarged. The median axis is indicated with a solid red line, while the dashed yellow line corresponds to the median axis of the LVOT. The dotted white lines corresponds to the considered transverse slices. The radial positions (e.g., r_{5L}) and activation of the LVOT walls are extracted.

Appendix B

Table of Image Sources

Figure	Source	Comments
Figure 2.1a	BodyParts3D/Anatomography, Heart near, CC BY-SA 1.0	Cropped and annotated
Figure 2.1b	anonymous, Diagram of the human heart (valves improved), CC BY-SA 3.0	N/A
Figure 2.2	Clker-Free-Vector-Images, Human Heart Pumping	N/A
Figure 2.3	Madhero88, Conductionsystemoftheheart, CC BY 3.0	N/A
Figure 2.4	OpenStax College, 2028 Cardiac Cycle vs Electrocardiogram, CC BY 3.0	N/A
Figure 2.5	OpenStax College, 2024 Cardiac Arrhythmias, CC BY 3.0	Cropped and annotated
Figure 2.6	[79]	Combined
Figure 2.7a	[123]	N/A
Figure 2.7b	[124]	N/A
Figure 2.8	[125]	Cropped
Figure 2.9	[126]	Cropped
Figure 3.1	Created by the author	Based on [37]
Figure 3.2a	Blausen.com staff (2014). Medical gallery of Blausen Medical 2014. WikiJournal of Medicine 1 (2). DOI:10.15347/wjm/2014.010. ISSN. 2002-4436, Blausen 0467 HeartLocation, CC BY 3.0	Cropped and annotated
Figure 3.2b	Human_anatomy_planes.svg, YassineMrabet. This PNG graphic was created with Inkscape., Human anatomy planes-ES, CC BY-SA 3.0	Annotated
Figure 3.2c	[80]	N/A
Figure 3.2d	[80]	N/A
Figure 3.3	[79]	Combined
Figure 3.4a	[79]	N/A
Figure 3.4b	Created by the author	N/A
Figure 3.5a	[79]	N/A
Figure 3.5b	Created by the author	N/A
Figure 3.6a	[79]	N/A
Figure 3.6b	Created by the author	N/A

TABLE B.1: Table of Image Sources

Figure	Source	Comments
Figure 3.7a	[79]	N/A
Figure 3.7b	[79]	N/A
Figure 3.7c	Created by the author	N/A
Figure 3.8	Created by the author	Based on [62]
Figure 3.9a-d	[79]	Combined
Figure 3.9	Created by the author	N/A
Figure 3.10	Created by the author	Based on [62]
Figure 3.11	Created by the author	Based on [62]
Figure 3.12	Created by the author	N/A
Figure 3.13	Created by the author	N/A
Figure 3.14	Created by the author	N/A
Figure 3.15	Created by the author	N/A
Figure 3.16	Created by the author	N/A
Figure 3.17	Created by the author	N/A
Figure 3.18	Created by the author	N/A
Figure 3.19	Created by the author	N/A
Figure 3.20	Created by the author	N/A
Figure 3.21	Created by the author	N/A
Figure 3.22	Created by the author	N/A
Figure 3.23	Created by the author	N/A
Figure 3.24	Created by the author	N/A
Figure 3.25	Created by the author	N/A
Figure 3.26	Created by the author	N/A
Figure 3.27	Created by the author	N/A
Figure 3.28	Created by the author	N/A
Figure 3.29	Created by the author	N/A
Figure 4.1	Created by the author	N/A
Figure 4.2	Dllu, Cpd fish affine, CC BY-SA 3.0	Extracted frames, resized, and arranged in a grid layout
Figure 4.3	[127]	N/A
Figure 4.5	Created by the author	N/A
Figure 4.7	Created by the author	N/A
Figure 4.8	Created by the author	N/A

TABLE B.2: Table of Image Sources (continued)

Appendix C

ISBI 2024 Poster

Poster titled "FAST AND ROBUST ALGORITHM FOR 3D RENDERING OF 2D ELECTROMECHANICAL WAVE IMAGING MAPS AND CT REGISTRATION" presented at the 21st IEEE International Symposium on Biomedical Imaging (ISBI 2024) held in Athens, Greece from May 27 to May 30, 2024. The key findings emphasized the enhanced spatial accuracy of 3D-rendered electromechanical maps, improving their clinical adaptability. Additionally, the registration of 3D-rendered EWI maps with patient CT scans demonstrated the potential for better multimodal imaging integration, although challenges in registration consistency remain. This study also highlighted future directions, including the incorporation of short-axis views and intracardiac CT-based mapping data.

ID: 1542

FAST AND ROBUST ALGORITHM FOR 3D RENDERING OF 2D ELECTROMECHANICAL WAVE IMAGING MAPS AND CT REGISTRATION

Katerina Afentouli[1], Melina Tourni[2], Johanna Tonko[3], Elisa E. Konofagou[4]
[1]School of Electrical and Computer Engineering, National Technical University of Athens, Athens, Greece
[2]Department of Biomedical Engineering, Columbia University, New York, NY, USA
[3]Institute of Cardiovascular Sciences, University College London, London, UK
[4]Department of Radiology, Columbia University, New York, NY, USA

Introduction

2D Electromechanical Wave Imaging (EWI) is a non-invasive, high frame rate ultrasound imaging modality capable of localizing and visualizing electromechanical activation in the four chambers of the heart of human and canine models in normal rhythm or paced[1,2]. While it offers valuable slice-by-slice representations, it may obscure the continuous 3D wave propagation across the myocardium, hindering comprehensive understanding. Although 3D rendered electromechanical activation maps clearly depict the propagation of the electromechanical wave, detecting small arrhythmogenic sources can still be challenging[3].

Objectives

- **Advance the 3D rendering algorithm** by enhancing its view-agnostic capabilities.
- **Make 3D EWI more clinically adaptable** by transforming the current manually run algorithm into an accessible platform.
- **Enhance 3D-rendered anatomical accuracy** with CT registration.

Methods

Electromechanical Wave Imaging & 3D Rendering

Electromechanical Wave Imaging

High frame rate acquisition[4]
- Single Diverging Wave
- 2000 fps
- Verasonics Vantage 256 system
- P4-2 phased array, f0 = 2.5MHz

Myocardium segmentation and axial displacement estimation[5]
- Radiofrequency data
- 1D cross-correlation

Axial incremental strain estimation[6]

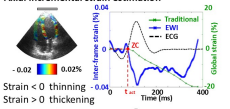

Strain < 0 thinning
Strain > 0 thickening

2D EWI isochrone generation[7]

Electromechanical Activation Time

For each point, t_{act} = 1st sign change in axial strain (zero-crossing) after QRS onset

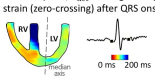

Standard 3D-rendered EWI[3]

Registration of 4 standard apical views (4-, 3-, 2-, 3.5-Chamber) around the manually selected LV median axis of symmetry and interpolation around the circumference.

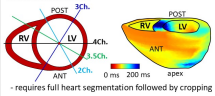

- requires full heart segmentation followed by cropping

Advanced 3D Rendering

Registration of apical LV-focused views around the LV median axis and interpolation around the circumference.

Improvements
- View-agnostic capabilities to render any combination of apical LV focused views *(Fig. 1(a),(d))*
- Addition of RV Parasternal Long Axis (PLAX) view *(Fig. 1(a),(b))*
- Addition of Left Ventricular Outflow Tract (LVOT) render *(Fig.1 (c))*

Optimizations
- Ventricle/Atria-only rendering instead of Full Heart
- Auto-cavity and median axis detection
- ~50% decrease in rendering time (before: 13.8 min, now: 7.5 min)

PC Specifications
- Dual Intel Xeon E5-2680 v4 @ 2.40GHz, 192GB RAM, NVIDIA Quadro RTX 8000, 3.6TB SSD, Windows 10
- Matlab 2023b

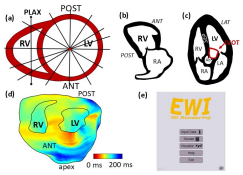

Figure 1. (a) View from the heart base of the relative positions of the imaging planes. (b) Schematic of RV PLAX view. (c) Schematic of 5 Chamber apical view with Left Ventricular Outflow Tract (LVOT) outlined. (d) Example 3D Isochrone utilizing 7 apical views. (e) Graphical user interface for 3D rendering.

3D Isochrone – CT Registration

1. Bi-ventricular Shell Extraction

- 3D-rendered isochrone boundary extraction and scaling
- CT scan cropping to isolate ventricular points

3D Isochrone (ISO) and CT shell

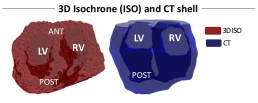

2. Left Ventricle Point Extraction & Ellipsoid Fitting

- LV point extraction using triangle-ray intersection[8]
- LV ellipsoid fit and principal axes calculation

3D ISO and CT shells with LV points outlined

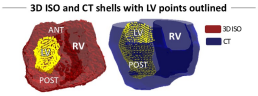

LV point data and ellipsoid fit for each shell

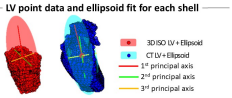

3. 3D Shell Registration

- Principal axes registration to determine 3D geometric transformation A
- Shell registration by applying transformation A to the 3D ISO

Principal axes registration before & after

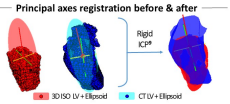

Shell registration before & after

4. 3D Surface Warping

- Non-Rigid ICP[10] transformation on 3D ISO shell
- Nearest-neighbor interpolation on CT shell

3D ISO shell NR-ICP transformation

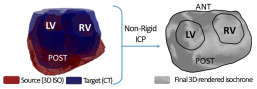

LAT: Lateral, POST: Posterior, LV: Left Ventricle, RV: Right Ventricle, SEP: Septum, PLAX: Parasternal Long Axis, LVOT: Left Ventricular Outflow Tract, CT: Computed Tomography, ISO: Isochrone, ICP: Iterative Closest Point, NR-ICP: Non-Rigid Iterative Closest Point

Results

In all figures, red indicates early activation and blue represents late activation (in milliseconds).

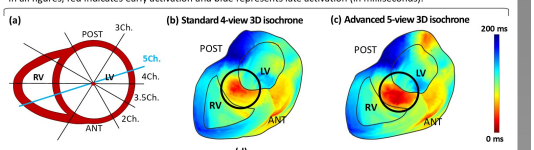

Figure 2. 24-year-old female patient with dilated cardiomyopathy (DCM) and mid-septal fibrosis, experiencing a high burden of symptomatic ventricular ectopy originating from the outflow tracts. (a) View from the heart base of the relative positions of the 5 imaging planes. (b) 3D-rendered isochrone of 4 standard apical views (4-, 3-, 2-, 3.5-Chamber) using the original algorithm. (c) 3D-rendered isochrone of 5 apical views (5-, 4-, 3-, 2-, 3.5-Chamber) using the advanced algorithm. (d) 2D isochrones of the 5 views.

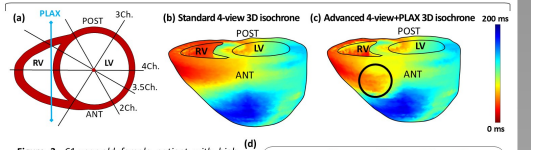

Figure 3. 61-year-old female patient with high ventricular ectopy in the right ventricular outflow tract (RVOT) (15-31% in repeated Holter ECGs). Baseline ECG showed features of arrhythmogenic right ventricular cardiomyopathy (ARVC) but no structural alterations on cardiac MRI and PET CT. (a) View from the heart base of the relative positions of the 4 apical and PLAX imaging planes. (b) 3D-rendered isochrone of 4 standard apical views (4-, 3-, 2-, 3.5-Chamber) using the original algorithm. (c) 3D-rendered isochrone of 4 standard apical and PLAX views using the advanced algorithm. (d) 2D isochrones of the 5 views.

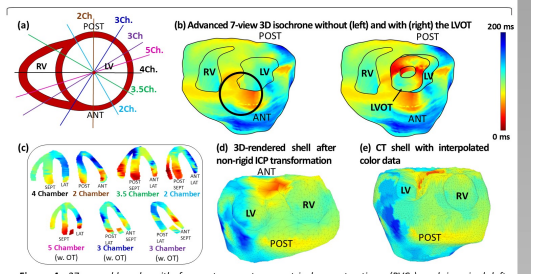

Figure 4. 27-year-old male with frequent premature ventricular contractions (PVCs) and impaired left ventricular function (EF 45%). The patient has a high burden of ventricular ectopy originating from the aortic root/left ventricular outflow tract (LVOT). (a) View from the heart base of the relative positions of 7 apical imaging planes. (b) 3D-rendered isochrone of all 7 apical views using the advanced algorithm without (left) and with (right) the addition of the LVOT. (c) 2D isochrones of the 7 views color-coded. (d) 3D-rendered shell after non-rigid ICP transformation (e) CT shell with nearest neighbor interpolated color data.

Discussion and Conclusions

Proposed Advanced 3D-Rendering Algorithm

- **Enhanced data coverage** in areas previously under-sampled
- **Improved localization** with more anatomically accurate ventricular and atrial shapes
- **Streamlined workflow** with no manual code manipulation and reduced computation times by ~50%
- **Increased spatial accuracy** with 3D isochrone-CT registration

Limitations

- 3D-rendered localization may be limited by image quality and patient anatomy.
- Accurately registering 3D-rendered isochrones with CT scan data may face registration challenges and require optimization for consistent multimodal imaging integration.
- CT scan's ventricular/atrial volumes may not always constitute a reliable ground truth.

Future Work

- Include additional short-axis and out-of-LV median-axis views in the rendering process
- Expand the registration methodology to integrate data from intracardiac CT-based mapping

References

1. Costet A. *et al.*, Physics in Medicine & Biology 2016
2. Provost J. *et al.*, Heart Rhythm 2013
3. Nauleau P. *et al.*, Medical Physics, 2017
4. Provost J. *et al.*, Proceedings of the National Academy of Sciences 2011
5. Luo J. & Konofagou E., IEEE T-UFFC 2010
6. Kallel F. & Ophir J., Ultrasonic Imaging 1997
7. Melki L. *et al.*, Ultrasound in Medicine and Biology 2017
8. Mouller T. & Trumbore B., Journal of Graphics Tools 1997
9. Besl P. & McKay N., IEEE Trans. Pattern Anal. Mach. Intell. 1992
10. Amberg B. *et al.*, IEEE CVPR 2007

Figure C.1: Poster titled "FAST AND ROBUST ALGORITHM FOR 3D RENDERING OF 2D ELECTROMECHANICAL WAVE IMAGING MAPS AND CT REGISTRATION" presented at the 21st IEEE International Symposium on Biomedical Imaging (ISBI 2024) held in Athens, Greece from May 27 to May 30, 2024.

Bibliography

[1] *More than half of U.S. adults don't know heart disease is leading cause of death, despite 100-year reign*. American Heart Association. URL: http://newsroom.heart.org/news/more-than-half-of-u-s-adults-dont-know-heart-disease-is-leading-cause-of-death-despite-100-year-reign (visited on 09/09/2024).

[2] *Causes of death statistics*. URL: https://ec.europa.eu/eurostat/statistics-explained/index.php?title=Causes_of_death_statistics (visited on 09/28/2024).

[3] *Cardiovascular diseases statistics*. URL: https://ec.europa.eu/eurostat/statistics-explained/index.php? (visited on 09/28/2024).

[4] Min Jiao et al. "Estimates of the global, regional, and national burden of atrial fibrillation in older adults from 1990 to 2019: insights from the Global Burden of Disease study 2019". In: *Frontiers in Public Health* 11 (June 12, 2023), p. 1137230. ISSN: 2296-2565. DOI: 10.3389/fpubh.2023.1137230. URL: https://www.ncbi.nlm.nih.gov/pmc/articles/PMC10291625/ (visited on 09/09/2024).

[5] Marco Zuin et al. "Trends in atrial fibrillation-related mortality in Europe, 2008–2019". In: *European Heart Journal - Quality of Care and Clinical Outcomes* 10.5 (Aug. 8, 2024), pp. 467–478. ISSN: 2058-5225, 2058-1742. DOI: 10.1093/ehjqcco/qcae007. URL: https://academic.oup.com/ehjqcco/article/10/5/467/7592009 (visited on 09/09/2024).

[6] Olivier Piot et al. "Prospective evolution of cardiac arrhythmia care: 2030 vision". In: *Archives of Cardiovascular Diseases* 115.3 (Mar. 1, 2022), pp. 179–189. ISSN: 1875-2136. DOI: 10.1016/j.acvd.2022.02.008. URL: https://www.sciencedirect.com/science/article/pii/S1875213622000456 (visited on 09/11/2024).

[7] A. John Camm et al. "Guidelines for the management of atrial fibrillation: the Task Force for the Management of Atrial Fibrillation of the European Society of Cardiology (ESC)". In: *Europace: European Pacing, Arrhythmias, and Cardiac Electrophysiology: Journal of the Working Groups on Cardiac Pacing, Arrhythmias, and Cardiac Cellular Electrophysiology of the European Society of Cardiology* 12.10 (Oct. 2010), pp. 1360–1420. ISSN: 1532-2092. DOI: 10.1093/europace/euq350.

[8] Etienne Aliot et al. "Quality of life in patients with atrial fibrillation: how to assess it and how to improve it". In: *EP Europace* 16.6 (June 1, 2014), pp. 787–796. ISSN: 1099-5129. DOI: 10.1093/europace/eut369. URL: https://doi.org/10.1093/europace/eut369 (visited on 09/11/2024).

[9] Zain Sharif and Leon M. Ptaszek. "Global disparities in arrhythmia care: Mind the gap". In: *Heart Rhythm O2* 3.6 (Dec. 16, 2022), pp. 783–792. ISSN: 2666-5018. DOI: 10.1016/j.hroo.2022.09.007. URL: https://www.ncbi.nlm.nih.gov/pmc/articles/PMC9795303/ (visited on 09/11/2024).

[10] *Arrhythmia*. nhs.uk. Section: conditions. Feb. 19, 2018. URL: https://www.nhs.uk/conditions/arrhythmia/ (visited on 09/09/2024).

[11] Josep Brugada. *Cardiac arrhythmias and sudden death*. URL: https://www.escardio.org/Journals/E-Journal-of-Cardiology-Practice/Volume-2/Cardiac-Arrhythmias-and-Sudden-Death-Title-Cardiac-Arrhythmias-and-Sudden-Dea (visited on 09/09/2024).

[12] Ambrose S. Kibos, ed. *Cardiac arrhythmias: From Basic Mechanism to State-of-the-Art Management*. London Heidelberg: Springer, 2014. 678 pp. ISBN: 978-1-4471-5315-3.

[13] B. Olshansky. "Clinical Assessment of the Cardiac Arrhythmia Patient". In: *Reference Module in Biomedical Sciences*. Elsevier, 2018, B978012801238399768X. ISBN: 978-0-12-801238-3. DOI: 10.1016/B978-0-12-801238-3.99768-X. URL: https://linkinghub.elsevier.com/retrieve/pii/B978012801238399768X (visited on 09/11/2024).

[14] Jean Provost et al. "Imaging the electromechanical activity of the heart in vivo". In: *Proceedings of the National Academy of Sciences* 108.21 (May 24, 2011), pp. 8565–8570. ISSN: 0027-8424, 1091-6490. DOI: 10.1073/pnas.1011688108. URL: https://pnas.org/doi/full/10.1073/pnas.1011688108 (visited on 09/12/2024).

[15] Joshua D. Pollock and Amgad N. Makaryus. "Physiology, Cardiac Cycle". In: *StatPearls*. Treasure Island (FL): StatPearls Publishing, 2024. URL: http://www.ncbi.nlm.nih.gov/books/NBK459327/ (visited on 09/09/2024).

[16] Paul A. Iaizzo, ed. *Handbook of Cardiac Anatomy, Physiology, and Devices*. Totowa, NJ: Humana Press, 2005. ISBN: 978-1-58829-443-2 978-1-59259-835-9. DOI: 10.1007/978-1-59259-835-9. URL: http://link.springer.com/10.1007/978-1-59259-835-9 (visited on 09/28/2024).

[17] Anthony H. Kashou, Hajira Basit, and Lovely Chhabra. "Physiology, Sinoatrial Node". In: *StatPearls*. Treasure Island (FL): StatPearls Publishing, 2024. URL: http://www.ncbi.nlm.nih.gov/books/NBK459238/ (visited on 09/09/2024).

[18] Putri Madona, Rahmat Ilias Basti, and Muhammad Mahrus Zain. "PQRST wave detection on ECG signals". In: *Gaceta Sanitaria* 35 (2021), S364–S369. ISSN: 02139111. DOI: 10.1016/j.gaceta.2021.10.052. URL: https://linkinghub.elsevier.com/retrieve/pii/S0213911121002466 (visited on 09/28/2024).

[19] Dhaval S. Desai and Said Hajouli. "Arrhythmias". In: *StatPearls*. Treasure Island (FL): StatPearls Publishing, 2024. URL: http://www.ncbi.nlm.nih.gov/books/NBK558923/ (visited on 09/09/2024).

[20] Charles Antzelevitch and Alexander Burashnikov. "Overview of Basic Mechanisms of Cardiac Arrhythmia". In: *Cardiac Electrophysiology Clinics* 3.1 (Mar. 2011), pp. 23–45. ISSN: 18779182. DOI: 10.1016/j.ccep.2010.10.012. URL: https://linkinghub.elsevier.com/retrieve/pii/S1877918210001425 (visited on 09/28/2024).

[21] Rowan Cook, ed. *Cardiac Arrhythmias: From Mechanisms to Management*. FOSTER ACADEMICS, June 28, 2019. 181 pp. ISBN: 978-1-63242-605-5.

[22] Nadir Saoudi et al. "Classification of Atrial Flutter and Regular Atrial Tachycardia According to Electrophysiologic Mechanism and Anatomic Bases: A Statement from a Joint Expert Group from the Working Group of Arrhythmias of the European Society of Cardiology and the North American Society of Pacing and Electrophysiology". In: *Journal of Cardiovascular Electrophysiology* 12.7 (July 2001), pp. 852–866. ISSN: 1045-3873, 1540-8167. DOI: 10.1046/j.1540-8167.2001.00852.x. URL: https://onlinelibrary.wiley.com/doi/10.1046/j.1540-8167.2001.00852.x (visited on 09/09/2024).

[23] *Overview of Abnormal Heart Rhythms - Heart and Blood Vessel Disorders*. MSD Manual Consumer Version. URL: https://www.msdmanuals.com/home/heart-and-blood-vessel-disorders/abnormal-heart-rhythms/overview-of-abnormal-heart-rhythms (visited on 09/09/2024).

[24] Du-guan Fu. "Cardiac Arrhythmias: Diagnosis, Symptoms, and Treatments". In: *Cell Biochemistry and Biophysics* 73.2 (Nov. 1, 2015), pp. 291–296. ISSN: 1559-0283. DOI: 10.1007/s12013-015-0626-4. URL: https://doi.org/10.1007/s12013-015-0626-4 (visited on 09/09/2024).

[25] John Kingma, Chantale Simard, and Benoît Drolet. "Overview of Cardiac Arrhythmias and Treatment Strategies". In: *Pharmaceuticals* 16.6 (June 6, 2023), p. 844. ISSN: 1424-8247. DOI: 10.3390/ph16060844. URL: https://www.ncbi.nlm.nih.gov/pmc/articles/PMC10301085/ (visited on 09/09/2024).

[26] Gan-Xin Yan, Peter R. Kowey, and Charles Antzelevitch, eds. *Management of Cardiac Arrhythmias*. Contemporary Cardiology. Cham: Springer International Publishing, 2020. ISBN: 978-3-030-41966-0 978-3-030-41967-7. DOI: 10.1007/978-3-030-41967-7. URL: https://link.springer.com/10.1007/978-3-030-41967-7 (visited on 09/10/2024).

[27] *Challenges in the Cardiovascular Evaluation and Management of Patients With Obesity*. American College of Cardiology. URL: https://www.acc.org/Latest-in-Cardiology/Articles/2024/01/05/13/21/http%3a%2f%2fwww.acc.org%2fLatest-in-Cardiology%2fArticles%2f2024%2f01%2f05%2f13%2f21%2fChallenges-in-the-CV-Evaluation-and-Management-of-Patients-With-Obesity (visited on 09/10/2024).

[28] Peter M. Kistler et al. "P-wave morphology in focal atrial tachycardia: development of an algorithm to predict the anatomic site of origin". In: *Journal of the American College of Cardiology* 48.5 (Sept. 5, 2006), pp. 1010–1017. ISSN: 1558-3597. DOI: 10.1016/j.jacc.2006.03.058.

[29] Zhi-Yong Qian et al. "An algorithm to predict the site of origin of focal atrial tachycardia". In: *Pacing and clinical electrophysiology: PACE* 34.4 (Apr. 2011), pp. 414–421. ISSN: 1540-8159. DOI: 10.1111/j.1540-8159.2010.02980.x.

[30] S. Milstein et al. "An algorithm for the electrocardiographic localization of accessory pathways in the Wolff-Parkinson-White syndrome". In: *Pacing and clinical electrophysiology: PACE* 10.3 (May 1987), pp. 555–563. ISSN: 0147-8389. DOI: 10.1111/j.1540-8159.1987.tb04520.x.

[31] Joshua D. Moss et al. "ECG criteria for accurate localization of left anterolateral and posterolateral accessory pathways". In: *Pacing and clinical electrophysiology: PACE* 35.12 (Dec. 2012), pp. 1444–1450. ISSN: 1540-8159. DOI: 10.1111/pace.12011.

[32] Victor Bazan and Francis E. Marchlinski. "The 12-lead ECG during ventricular tachycardia: Still an important tool for ventricular tachycardia localization in structural heart disease". In: *Heart Rhythm* 15.10 (Oct. 2018), pp. 1498–1499. ISSN: 1556-3871. DOI: 10.1016/j.hrthm.2018.06.039.

[33] Sanjay Dixit et al. "Identification of distinct electrocardiographic patterns from the basal left ventricle: distinguishing medial and lateral sites of origin in patients with idiopathic ventricular tachycardia". In: *Heart Rhythm* 2.5 (May 2005), pp. 485–491. ISSN: 1547-5271. DOI: 10.1016/j.hrthm.2005.01.023.

[34] Elisa Ebrille et al. "Distinguishing Ventricular Arrhythmia Originating from the Right Coronary Cusp, Peripulmonic Valve Area, and the Right Ventricular Outflow Tract: Utility of Lead I". In: *Journal of Cardiovascular Electrophysiology* 25.4 (Apr. 2014), pp. 404–410. ISSN: 1045-3873, 1540-8167. DOI: 10.1111/jce.12330. URL: https://onlinelibrary.wiley.com/doi/10.1111/jce.12330 (visited on 09/10/2024).

[35] Christopher S. Grubb et al. "Noninvasive localization of cardiac arrhythmias using electromechanical wave imaging". In: *Science Translational Medicine* 12.536 (Mar. 25, 2020), eaax6111. ISSN: 1946-6234, 1946-6242. DOI: 10.1126/scitranslmed.aax6111. URL: https://www.science.org/doi/10.1126/scitranslmed.aax6111 (visited on 09/18/2023).

[36] Anita Sadeghpour and Azin Alizadehasl, eds. *Case-Based Textbook of Echocardiography*. Cham: Springer International Publishing, 2018. ISBN: 978-3-319-67689-0 978-3-319-67691-3. DOI: 10.1007/978-3-319-67691-3. URL: http://link.springer.com/10.1007/978-3-319-67691-3 (visited on 09/10/2024).

[37] Bernard E. Bulwer and Jose M. Rivero. *Echocardiography Pocket Guide: The Transthoracic Examination*. 1st. Jones & Bartlett Publishers, 2010. 352 pp. ISBN: 978-0-7637-7935-1.

[38] Susanna Price. "Echocardiography in post-cardiac surgery". In: *Oxford Textbook of Advanced Critical Care Echocardiography*. Ed. by Anthony McLean et al. Oxford University Press, Feb. 1, 2020, p. 0. ISBN: 978-0-19-874928-8. DOI: 10.1093/med/9780198749288.003.0023. URL: https://doi.org/10.1093/med/9780198749288.003.0023 (visited on 09/10/2024).

[39] Constantinos H. Papadopoulos et al. "Echocardiography and cardiac arrhythmias". In: *Hellenic Journal of Cardiology* 59.3 (May 2018), pp. 140–149. ISSN: 11099666. DOI: 10.1016/j.hjc.2017.11.017. URL: https://linkinghub.elsevier.com/retrieve/pii/S1109966617304104 (visited on 09/10/2024).

[40] Roberto M. Lang et al. "Recommendations for Cardiac Chamber Quantification by Echocardiography in Adults: An Update from the American Society of Echocardiography and the European Association of Cardiovascular Imaging". In: *European Heart Journal – Cardiovascular Imaging* 16.3 (Mar. 2015), pp. 233–271. ISSN: 2047-2404, 2047-2412. DOI: 10.1093/ehjci/jev014. URL: https://academic.oup.com/ehjcimaging/article-lookup/doi/10.1093/ehjci/jev014 (visited on 09/10/2024).

[41] Maninder Singh et al. "Echocardiographic Imaging Challenges in Obesity: Guideline Recommendations and Limitations of Adjusting to Body Size". In: *Journal of the American Heart Association* 9.2 (Jan. 21, 2020). Publisher: Wiley, e014609. DOI: 10.1161/JAHA.119.014609. URL: https://www.ahajournals.org/doi/10.1161/JAHA.119.014609 (visited on 09/10/2024).

[42] Irene Nicastro et al. "Professional Education, Training and Role of the Cardiac Sonographer in Different Countries". In: *Journal of Cardiovascular Echography* 23.1 (Mar. 2013). Publisher: Wolters Kluwer – Medknow Publications, p. 18. ISSN: 2211-4122. DOI: 10.4103/2211-4122.117981. URL: https://www.ncbi.nlm.nih.gov/pmc/articles/PMC5353438/ (visited on 09/10/2024).

[43] Kennosuke Yamashita et al. "Intracardiac electrogram–based atrial pace mapping for detecting the earliest activation site in atrial arrhythmias". In: *Heart Rhythm* 21.8 (Aug. 1, 2024). Publisher: Elsevier, pp. 1400–1408. ISSN: 1547-5271, 1556-3871. DOI: 10.1016/j.hrthm.2024.02.028. URL: https://www.heartrhythmjournal.com/article/S1547-5271(24)00199-1/fulltext (visited on 09/10/2024).

[44] Shu Meng et al. "Non-Contact Intracardiac Potential Mapping Using Mesh-Based and Meshless Inverse Solvers". In: *Frontiers in Physiology* 13 (July 7, 2022), p. 873630. ISSN: 1664-042X. DOI: 10.3389/fphys.2022.873630. URL: https://www.ncbi.nlm.nih.gov/pmc/articles/PMC9301455/ (visited on 09/10/2024).

[45] Benjamin Schaeffer and William G. Stevenson. "Entrainment mapping: Theoretical considerations and practical implementation". In: *Journal of Cardiovascular Electrophysiology* 29.1 (Jan. 2018), pp. 204–213. ISSN: 1540-8167. DOI: 10.1111/jce.13348.

[46] Peter W. Macfarlane et al., eds. *Comprehensive Electrocardiology*. London: Springer London, 2010. ISBN: 978-1-84882-045-6 978-1-84882-046-3. DOI: 10.1007/978-1-84882-046-3. URL: http://link.springer.com/10.1007/978-1-84882-046-3 (visited on 09/10/2024).

[47] Ranghadham Nagarakanti and Sanjeev Saksena. "Three-dimensional mapping and intracardiac echocardiography in the treatment of sinoatrial nodal tachycardias". In: *Journal of Interventional Cardiac Electrophysiology: An International Journal of Arrhythmias and Pacing* 46.1 (June 2016), pp. 55–61. ISSN: 1572-8595. DOI: 10.1007/s10840-015-0072-7.

[48] Simon C. Sporton et al. "Electroanatomic versus fluoroscopic mapping for catheter ablation procedures: a prospective randomized study". In: *Journal of Cardiovascular Electrophysiology* 15.3 (Mar. 2004), pp. 310–315. ISSN: 1045-3873. DOI: 10.1111/j.1540-8167.2004.03356.x.

[49] Paulus Kirchhof et al. "A novel nonfluoroscopic catheter visualization system (LocaLisa) to reduce radiation exposure during catheter ablation of supraventricular tachycardias". In: *The American Journal of Cardiology* 90.3 (Aug. 1, 2002), pp. 340–343. ISSN: 0002-9149. DOI: 10.1016/s0002-9149(02)02481-5.

[50] H. A. Kopelman et al. "Slow pathway catheter ablation of atrioventricular nodal re-entrant tachycardia guided by electroanatomical mapping: a randomized comparison to the conventional approach". In: *Europace: European Pacing, Arrhythmias, and Cardiac Electrophysiology: Journal of the Working Groups on Cardiac Pacing, Arrhythmias, and Cardiac Cellular Electrophysiology of the European Society of Cardiology* 5.2 (Apr. 2003), pp. 171–174. ISSN: 1099-5129. DOI: 10.1053/eupc.2002.0296.

[51] Deepak Bhakta and John M Miller. "Principles of Electroanatomic Mapping". In: *Indian Pacing and Electrophysiology Journal* 8.1 (Feb. 1, 2008), pp. 32–50. ISSN: 0972-6292. URL: https://www.ncbi.nlm.nih.gov/pmc/articles/PMC2231602/ (visited on 09/10/2024).

[52] Anselma Intini et al. "Electrocardiographic imaging (ECGI), a novel diagnostic modality used for mapping of focal left ventricular tachycardia in a young athlete". In: *Heart rhythm : the official journal of the Heart Rhythm Society* 2.11 (Nov. 2005), pp. 1250–1252. ISSN: 1547-5271. DOI: 10.1016/j.hrthm.2005.08.019. URL: https://www.ncbi.nlm.nih.gov/pmc/articles/PMC2000800/ (visited on 09/11/2024).

[53] Matthijs Cluitmans et al. "Validation and Opportunities of Electrocardiographic Imaging: From Technical Achievements to Clinical Applications". In: *Frontiers in Physiology* 9 (Sept. 20, 2018). Publisher: Frontiers. ISSN: 1664-042X. DOI: 10.3389/fphys.2018.01305. URL: https://www.frontiersin.org/journals/physiology/articles/10.3389/fphys.2018.01305/full (visited on 09/11/2024).

[54] Ping Jia et al. "Electrocardiographic imaging of cardiac resynchronization therapy in heart failure: observation of variable electrophysiologic responses". In: *Heart Rhythm* 3.3 (Mar. 2006), pp. 296–310. ISSN: 1547-5271. DOI: 10.1016/j.hrthm.2005.11.025.

[55] Helder Pereira, Steven Niederer, and Christopher A Rinaldi. "Electrocardiographic imaging for cardiac arrhythmias and resynchronization therapy". In: *Europace* 22.10 (Aug. 5, 2020), pp. 1447–1462. ISSN: 1099-5129. DOI: 10.1093/europace/euaa165. URL: https://www.ncbi.nlm.nih.gov/pmc/articles/PMC7544539/ (visited on 09/11/2024).

[56] Howard S. Oster et al. "Noninvasive Electrocardiographic Imaging". In: *Circulation* 96.3 (Aug. 5, 1997). Publisher: American Heart Association, pp. 1012–1024. DOI: 10.1161/01.CIR.96.3.1012. URL: https://www.ahajournals.org/doi/full/10.1161/01.cir.96.3.1012 (visited on 09/11/2024).

[57] *Noninvasive ECG imaging of electrophysiologically abnormal substrates in infarcted hearts : A model study - PubMed*. URL: https://pubmed.ncbi.nlm.nih.gov/10662751/ (visited on 09/11/2024).

[58] J. E. Burnes et al. "Noninvasive electrocardiogram imaging of substrate and intramural ventricular tachycardia in infarcted hearts". In: *Journal of the American College of Cardiology* 38.7 (Dec. 2001), pp. 2071–2078. ISSN: 0735-1097. DOI: 10.1016/s0735-1097(01)01653-9.

[59] *Noninvasive electrocardiographic imaging for cardiac electrophysiology and arrhythmia - PubMed*. URL: https://pubmed.ncbi.nlm.nih.gov/15034569/ (visited on 09/11/2024).

[60] Christoph Hintermüller et al. "Sensitivity- and effort-gain analysis: multilead ECG electrode array selection for activation time imaging". In: *IEEE transactions on bio-medical engineering* 53.10 (Oct. 2006), pp. 2055–2066. ISSN: 0018-9294. DOI: 10.1109/TBME.2006.881797.

[61] Shougang Wang et al. "A composite high-frame-rate system for clinical cardiovascular imaging". In: *IEEE Transactions on Ultrasonics, Ferroelectrics and Frequency Control* 55.10 (Oct. 2008), pp. 2221–2233. ISSN: 0885-3010. DOI: 10.1109/TUFFC.921. URL: http://ieeexplore.ieee.org/document/4638908/ (visited on 09/12/2024).

[62] Pierre Nauleau et al. "Technical Note: A 3-D rendering algorithm for electromechanical wave imaging of a beating heart". In: *Medical Physics* 44.9 (Sept. 2017), pp. 4766–4772. ISSN: 00942405. DOI: 10.1002/mp.12411. URL: https://onlinelibrary.wiley.com/doi/10.1002/mp.12411 (visited on 09/18/2023).

[63] Lea Melki, Alexandre Costet, and Elisa E Konofagou. "Reproducibility and Angle Independence of Electromechanical Wave Imaging for the Measurement of Electromechanical Activation during Sinus Rhythm in Healthy Humans". In: *Ultrasound in Medicine and Biology* 43.10 (Oct. 2017), pp. 2256–2268. DOI: 10.1016/j.ultrasmedbio.2017.06.019. URL: https://www.umbjournal.org/article/S0301-5629(17)30287-9/abstract (visited on 09/12/2024).

[64] Alexandre Costet et al. "Electromechanical wave imaging (EWI) validation in all four cardiac chambers with 3D electroanatomic mapping in canines *in vivo*". In: *Physics in Medicine and Biology* 61.22 (Nov. 21, 2016), pp. 8105–8119. ISSN: 0031-9155, 1361-6560. DOI: 10.1088/0031-9155/61/22/8105. URL: https://iopscience.iop.org/article/10.1088/0031-9155/61/22/8105 (visited on 09/29/2023).

[65] Julien Grondin et al. "Validation of electromechanical wave imaging in a canine model during pacing and sinus rhythm". In: *Heart Rhythm* 13.11 (Nov. 2016), pp. 2221–2227. ISSN: 1556-3871. DOI: 10.1016/j.hrthm.2016.08.010.

[66] J. Provost et al. "Electromechanical Wave Imaging of Normal and Ischemic Hearts In Vivo". In: *IEEE Transactions on Medical Imaging* 29.3 (Mar. 2010), pp. 625–635. ISSN: 0278-0062, 1558-254X. DOI: 10.1109/TMI.2009.2030186. URL: http://ieeexplore.ieee.org/document/5223577/ (visited on 09/12/2024).

[67] Lea Melki et al. "A New Electromechanical Wave Imaging Dispersion Metric for the Characterization of Ventricular Activation in Different Cardiac Resynchronization Therapy Pacing Schemes". In: *IEEE Transactions on Biomedical Engineering* 70.3 (Mar. 2023), pp. 853–859. ISSN: 0018-9294, 1558-2531. DOI: 10.1109/TBME.2022.3203653. URL: https://ieeexplore.ieee.org/document/9873912/ (visited on 09/12/2024).

[68] Johanna Tonko et al. "Spatial Accuracy of Non-Invasive Activation Mapping Modalities for Complex Ventricular Arrhythmias: A Direct Comparison of Electromechanical Wave Imaging (EWI) Using High Frame Rate Transthoracic Echocardiography and Electrocardiographic Imaging (ECGi) With Cardiac CT". In: *Circulation* 148 (Suppl_1 Nov. 7, 2023). ISSN: 0009-7322, 1524-4539. DOI: 10.1161/circ.148.suppl_1.16985. URL: https://www.ahajournals.org/doi/10.1161/circ.148.suppl_1.16985 (visited on 09/12/2024).

[69] Melina Tourni et al. "Long-term response classification and prediction of atrial fibrillation ablation using non-invasive 3D-rendered electromechanical cycle length mapping". In: *2024 IEEE International Symposium on Biomedical Imaging (ISBI)*. Vol. 2888. Athens, Greece: IEEE, May 2024, pp. 1–5.

[70] Melina Tourni et al. "Long-term atrial arrhythmia characterization and treatment efficacy evaluation using non-invasive echocardiography-based electromechanical cycle length mapping: a case series". en. In: *Eur. Heart J. Case Rep.* 8.8 (Aug. 2024), ytae303.

[71] Melina Tourni et al. "Electromechanical Cycle Length Mapping for atrial arrhythmia detection and cardioversion success assessment". en. In: *Comput. Biol. Med.* 163.107084 (Sept. 2023), p. 107084.

[72] Joseph H. Holmes. "Diagnostic ultrasound during the early years of A.I.U.M." In: *Journal of Clinical Ultrasound* 8.4 (Aug. 1980), pp. 299–308. ISSN: 0091-2751, 1097-0096. DOI: 10.1002/jcu.1870080404. URL: https://onlinelibrary.wiley.com/doi/10.1002/jcu.1870080404 (visited on 09/13/2024).

[73] Peter R. Hoskins, Kevin Martin, and Abigail Thrush, eds. *Diagnostic ultrasound: physics and equipment*. Third edition. Boca Raton, FL: CRC Press/Taylor & Francis Group, 2019. 387 pp. ISBN: 978-1-138-89293-4 978-0-367-19041-5.

[74] Alaa A. Mohamed, Ahmed A. Arifi, and Ahmed Omran. "The basics of echocardiography". In: *Journal of the Saudi Heart Association* 22.2 (Apr. 2010), pp. 71–76. ISSN: 10167315. DOI: 10.1016/j.jsha.2010.02.011. URL: https://linkinghub.elsevier.com/retrieve/pii/S1016731510000345 (visited on 09/13/2024).

[75] J. David N. Cheeke. *Fundamentals and applications of ultrasonic waves*. CRC series in pure and applied physics. Boca Raton, Fla.: CRC Press, 2002. 462 pp. ISBN: 978-0-8493-0130-8.

[76] Manish Bansal and Ravi R. Kasliwal. "How do I do it? Speckle-tracking echocardiography". In: *Indian Heart Journal* 65.1 (Jan. 2013), pp. 117–123. ISSN: 0019-4832. DOI: 10.1016/j.ihj.2012.12.004. URL: https://www.ncbi.nlm.nih.gov/pmc/articles/PMC3860973/ (visited on 09/13/2024).

[77] Valentina S. Lucas et al. "Utility of High-Frequency Ultrasound: Moving Beyond the Surface to Detect Changes in Skin Integrity". In: *Plastic surgical nursing : official journal of the American Society of Plastic and Reconstructive Surgical Nurses* 34.1 (2014), pp. 34–38. ISSN: 0741-5206. DOI: 10.1097/PSN.0000000000000031. URL: https://www.ncbi.nlm.nih.gov/pmc/articles/PMC4027962/ (visited on 09/13/2024).

[78] Lea Melki, Melina Tourni, and Elisa E. Konofagou. "Electromechanical Wave Imaging With Machine Learning for Automated Isochrone Generation". In: *IEEE Transactions on Medical Imaging* 40.9 (Sept. 2021), pp. 2258–2271. ISSN: 0278-0062, 1558-254X. DOI: 10.1109/TMI.2021.3074808. URL: https://ieeexplore.ieee.org/document/9410293/ (visited on 09/13/2024).

[79] Thomas Böhmeke et al. *Pocket atlas of echocardiography*. Flexibook. Stuttgart: Thieme, 2006. 225 pp. ISBN: 978-1-58890-433-1 978-3-13-141241-6.

[80] Carol Mitchell et al. "Guidelines for Performing a Comprehensive Transthoracic Echocardiographic Examination in Adults: Recommendations from the American Society of Echocardiography". In: *Journal of the American Society of Echocardiography* 32.1 (Jan. 2019), pp. 1–64. ISSN: 08947317. DOI: 10.1016/j.echo.2018.06.004. URL: https://linkinghub.elsevier.com/retrieve/pii/S0894731718303183 (visited on 09/13/2024).

[81] Mathieu Pernot et al. "ECG-gated, Mechanical and Electromechanical Wave Imaging of Cardiovascular Tissues In Vivo". In: *Ultrasound in Medicine & Biology* 33.7 (July 2007), pp. 1075–1085. ISSN: 03015629. DOI: 10.1016/j.ultrasmedbio.2007.02.003. URL: https://linkinghub.elsevier.com/retrieve/pii/S0301562907000786 (visited on 09/14/2024).

[82] Jianwen Luo and Elisa E Konofagou. "A fast normalized cross-correlation calculation method for motion estimation". In: *IEEE Transactions on Ultrasonics, Ferroelectrics and Frequency Control* 57.6 (June 2010), pp. 1347–1357. ISSN: 0885-3010. DOI: 10.1109/TUFFC.2010.1554. URL: http://ieeexplore.ieee.org/document/5480177/ (visited on 09/15/2024).

[83] Faouzi Kallel and Jonathan Ophir. "A Least-Squares Strain Estimator for Elastography". In: *Ultrasonic Imaging* 19.3 (July 1997), pp. 195–208. ISSN: 0161-7346, 1096-0910. DOI: 10.1177/016173469701900303. URL: http://journals.sagepub.com/doi/10.1177/016173469701900303 (visited on 05/20/2024).

[84] Job Stoks et al. "An Open-Source Algorithm for Standardized Bullseye Visualization of High-Resolution Cardiac Ventricular Data: UNISYS". In: 2020 Computing in Cardiology Conference. Dec. 30, 2020. DOI: 10.22489/CinC.2020.160. URL: http://www.cinc.org/archives/2020/pdf/CinC2020-160.pdf (visited on 09/28/2023).

[85] The MathWorks Inc. *MATLAB version: 23.2.0 (R2023b)*. Natick, Massachusetts, United States, 2023. URL: https://www.mathworks.com (visited on 09/24/2024).

[86] J J Fenoglio Jr et al. "Canine mitral complex. Ultrastructure and electromechanical properties". en. In: *Circ. Res.* 31.3 (Sept. 1972), pp. 417–430.

[87] Martin Berger, Qiao Yang, and Andreas Maier. "X-ray Imaging". In: *Medical Imaging Systems*. Ed. by Andreas Maier et al. Vol. 11111. Series Title: Lecture Notes in Computer Science. Cham: Springer International Publishing, 2018, pp. 119–145. ISBN: 978-3-319-96519-2 978-3-319-96520-8. DOI: 10.1007/978-3-319-96520-8_7. URL: http://link.springer.com/10.1007/978-3-319-96520-8_7 (visited on 09/14/2024).

[88] *Computed Tomography (CT) - Special Subjects*. MSD Manual Consumer Version. URL: https://www.msdmanuals.com/home/special-subjects/common-imaging-tests/computed-tomography-ct (visited on 09/14/2024).

[89] Shady Hermena and Michael Young. "CT-scan Image Production Procedures". In: *StatPearls*. Treasure Island (FL): StatPearls Publishing, 2024. URL: http://www.ncbi.nlm.nih.gov/books/NBK574548/ (visited on 09/14/2024).

[90] Ehsan Samei and Norbert J. Pelc, eds. *Computed Tomography: Approaches, Applications, and Operations*. Cham: Springer International Publishing, 2020. ISBN: 978-3-030-26956-2 978-3-030-26957-9. DOI: 10.1007/978-3-030-26957-9. URL: http://link.springer.com/10.1007/978-3-030-26957-9 (visited on 09/14/2024).

[91] Kalgi Modi, Sandeep A. Padala, and Mohit Gupta. "Contrast-Induced Nephropathy". In: *StatPearls*. Treasure Island (FL): StatPearls Publishing, 2024. URL: http://www.ncbi.nlm.nih.gov/books/NBK448066/ (visited on 09/14/2024).

[92] Herbert L. Fred. "Drawbacks and Limitations of Computed Tomography". In: *Texas Heart Institute Journal* 31.4 (2004), pp. 345–348. ISSN: 0730-2347. URL: https://www.ncbi.nlm.nih.gov/pmc/articles/PMC548232/ (visited on 09/14/2024).

[93] *Cardiac Magnetic Resonance Imaging (MRI)*. www.heart.org. URL: https://www.heart.org/en/health-topics/heart-attack/diagnosing-a-heart-attack/magnetic-resonance-imaging-mri (visited on 09/15/2024).

[94] Center for Devices {and} Radiological Health. "Benefits and Risks". In: *FDA* (Feb. 9, 2019). Publisher: FDA. URL: https://www.fda.gov/radiation-emitting-products/mri-magnetic-resonance-imaging/benefits-and-risks (visited on 09/15/2024).

[95] A. Berger. "How does it work?: Magnetic resonance imaging". In: *BMJ* 324.7328 (Jan. 5, 2002), pp. 35–35. ISSN: 0959-8138, 1468-5833. DOI: 10.1136/bmj.324.7328.35. URL: https://www.bmj.com/lookup/doi/10.1136/bmj.324.7328.35 (visited on 09/15/2024).

[96] Chrysovalantou Nikolaidou et al. "The Role of Cardiovascular Magnetic Resonance Imaging in Patients with Cardiac Arrhythmias". In: *Reviews in Cardiovascular Medicine* 24.9 (Sept. 15, 2023), p. 252. ISSN: 1530-6550. DOI: 10.31083/j.rcm2409252. URL: https://www.imrpress.com/journal/RCM/24/9/10.31083/j.rcm2409252 (visited on 09/15/2024).

[97] Maryam Ghadimi and Amit Sapra. "Magnetic Resonance Imaging Contraindications". In: *StatPearls*. Treasure Island (FL): StatPearls Publishing, 2024. URL: http://www.ncbi.nlm.nih.gov/books/NBK551669/ (visited on 09/15/2024).

[98] Bander S Hilabi, Sami A Alghamdi, and Mansour Almanaa. "Impact of Magnetic Resonance Imaging on Healthcare in Low- and Middle-Income Countries". In: *Cureus* (Apr. 17, 2023). ISSN: 2168-8184. DOI: 10.7759/cureus.37698. URL: https://www.cureus.com/articles/147284-impact-of-magnetic-resonance-imaging-on-healthcare-in-low--and-middle-income-countries (visited on 09/15/2024).

[99] Francisco Reyes-Santias et al. "Cost Analysis of Magnetic Resonance Imaging and Computed Tomography in Cardiology: A Case Study of a University Hospital Complex in the Euro Region". In: *Healthcare* 11.14 (July 21, 2023), p. 2084. ISSN: 2227-9032. DOI: 10.3390/healthcare11142084. URL: https://www.mdpi.com/2227-9032/11/14/2084 (visited on 09/15/2024).

[100] *What is a Point Cloud? - GIGABYTE Global*. GIGABYTE. URL: https://www.gigabyte.com/Glossary/point-cloud (visited on 09/15/2024).

[101] Matthew Berger et al. "A Survey of Surface Reconstruction from Point Clouds". In: *Computer Graphics Forum* 36.1 (Jan. 2017), pp. 301–329. ISSN: 0167-7055, 1467-8659. DOI: 10.1111/cgf.12802. URL: https://onlinelibrary.wiley.com/doi/10.1111/cgf.12802 (visited on 09/15/2024).

[102] *Point Cloud Registration: Beyond the Iterative Closest Point Algorithm*. Welcome to The Library! July 28, 2023. URL: https://www.thinkautonomous.ai/blog/point-cloud-registration/ (visited on 09/15/2024).

[103] S. Rusinkiewicz and M. Levoy. "Efficient variants of the ICP algorithm". In: *Proceedings Third International Conference on 3-D Digital Imaging and Modeling*. Third International Conference on 3-D Digital Imaging and Modeling. Quebec City, Que., Canada: IEEE Comput. Soc, 2001, pp. 145–152. ISBN: 978-0-7695-0984-6. DOI: 10.1109/IM.2001.924423. URL: http://ieeexplore.ieee.org/document/924423/ (visited on 09/15/2024).

[104] Jana Procházková and Dalibor Martišek. "Notes on Iterative Closest Point Algorithm". In: *17th Conference on Applied Mathematics (APLIMAT 2018)*. Journal of Applied Mathematics and Engineerings. Bratislava, Slovak Republic: Institute of Mathematics and Physics, Faculty of Mechanical Engineering, Apr. 2018, p. 1119. ISBN: 978-1-5108-6248-7. (Visited on 09/15/2024).

[105] Juyong Zhang, Yuxin Yao, and Bailin Deng. "Fast and Robust Iterative Closest Point". In: *IEEE Transactions on Pattern Analysis and Machine Intelligence* (2021), pp. 1–1. ISSN: 0162-8828, 2160-9292, 1939-3539. DOI: 10.1109/TPAMI.2021.3054619. URL: https://ieeexplore.ieee.org/document/9336308/ (visited on 09/15/2024).

[106] F.A. Donoso, K.J. Austin, and P.R. McAree. "Three new Iterative Closest Point variant-methods that improve scan matching for surface mining terrain". In: *Robotics and Autonomous Systems* 95 (Sept. 2017), pp. 117–128. ISSN: 09218890. DOI: 10.1016/j.robot.2017.05.003. URL: https://linkinghub.elsevier.com/retrieve/pii/S0921889016307102 (visited on 09/15/2024).

[107] Luming Liang et al. "Nonrigid iterative closest points for registration of 3D biomedical surfaces". In: *Optics and Lasers in Engineering* 100 (Jan. 2018), pp. 141–154. ISSN: 01438166. DOI: 10.1016/j.optlaseng.2017.08.005. URL: https://linkinghub.elsevier.com/retrieve/pii/S0143816617305985 (visited on 09/14/2024).

[108] Shiyang Cheng et al. "Statistical non-rigid ICP algorithm and its application to 3D face alignment". In: *Image and Vision Computing* 58 (Feb. 2017), pp. 3–12. ISSN: 02628856. DOI: 10.1016/j.imavis.2016.10.007. URL: https://linkinghub.elsevier.com/retrieve/pii/S0262885616301901 (visited on 09/14/2024).

[109] Brett Allen, Brian Curless, and Zoran Popović. "The space of human body shapes: reconstruction and parameterization from range scans". In: *ACM SIGGRAPH 2003 Papers*. SIGGRAPH03: Special Interest Group on Computer Graphics and Interactive Techniques. San Diego California: ACM, July 2003, pp. 587–594. ISBN: 978-1-58113-709-5. DOI: 10.1145/1201775.882311. URL: https://dl.acm.org/doi/10.1145/1201775.882311 (visited on 09/14/2024).

[110] Benoit Combes and Sylvain Prima. "Prior affinity measures on matches for ICP-like nonlinear registration of free-form surfaces". In: *2009 IEEE International Symposium on Biomedical Imaging: From Nano to Macro*. 2009 IEEE International Symposium on Biomedical Imaging: From Nano to Macro (ISBI). Boston, MA, USA: IEEE, June 2009, pp. 370–373. ISBN: 978-1-4244-3931-7. DOI: 10.1109/ISBI.2009.5193061. URL: http://ieeexplore.ieee.org/document/5193061/ (visited on 09/14/2024).

[111] Brian Amberg, Sami Romdhani, and Thomas Vetter. "Optimal Step Nonrigid ICP Algorithms for Surface Registration". In: *2007 IEEE Conference on Computer Vision and Pattern Recognition*. 2007 IEEE Conference on Computer Vision and Pattern Recognition. Minneapolis, MN, USA: IEEE, June 2007, pp. 1–8. ISBN: 978-1-4244-1179-5 978-1-4244-1180-1. DOI: 10.1109/CVPR.2007.383165. URL: http://ieeexplore.ieee.org/document/4270190/ (visited on 05/20/2024).

[112] Hamid R. Arabnia and Quoc-Nam Tran, eds. *Multimodality Medical Image Registration and Fusion Techniques Using Mutual Information and Genetic Algorithm-Based Approaches*. Vol. 696. Software Tools and Algorithms for Biological Systems, Advances in Experimental Medicine and Biology. New York, NY: Springer New York, 2011. ISBN: 978-1-4419-7045-9 978-1-4419-7046-6. DOI: 10.1007/978-1-4419-7046-6. URL: https://link.springer.com/10.1007/978-1-4419-7046-6 (visited on 09/15/2024).

[113] Lixia Shu et al. "An automatic and accurate registration method for electro-anatomical map and CT surface". In: *The International Journal of Medical Robotics and Computer Assisted Surgery* 13.4 (Dec. 2017), e1818. ISSN: 1478-5951, 1478-596X. DOI: 10.1002/rcs.1818. URL: https://onlinelibrary.wiley.com/doi/10.1002/rcs.1818 (visited on 09/15/2024).

[114] Gabriel Kiss et al. "Fusion of 3D echo and cardiac magnetic resonance volumes during live scanning". In: *2013 IEEE International Ultrasonics Symposium (IUS)*. 2013 IEEE International Ultrasonics Symposium (IUS). Prague, Czech Republic: IEEE, July 2013, pp. 832–835. ISBN: 978-1-4673-5686-2 978-1-4673-5684-8. DOI: 10.1109/ULTSYM.2013.0214. URL: http://ieeexplore.ieee.org/document/6724872/ (visited on 09/15/2024).

[115] R. Shekhar et al. "Registration of Real-Time 3-D Ultrasound Images of the Heart for Novel 3-D Stress Echocardiography". In: *IEEE Transactions on Medical Imaging* 23.9 (Sept. 2004), pp. 1141–1149. ISSN: 0278-0062. DOI: 10.1109/TMI.2004.830527. URL: http://ieeexplore.ieee.org/document/1327693/ (visited on 09/15/2024).

[116] Francesco Maffessanti et al. "FUSION IMAGING OF COMPUTED TOMOGRAPHY AND 3D ECHOCARDIOGRAPHY: FEASIBILITY OF COMBINED ASSESSMENT OF CORONARY ANATOMY AND MYOCARDIAL FUNCTION". In: *Journal of the American College of Cardiology* 63.12 (Apr. 2014), A1101. ISSN: 07351097. DOI: 10.1016/S0735-1097(14)61101-3. URL: https://linkinghub.elsevier.com/retrieve/pii/S0735109714611013 (visited on 09/15/2024).

[117] Azira Khalil et al. "Echocardiography to cardiac CT image registration: Spatial and temporal registration of the 2D planar echocardiography images with cardiac CT volume". In: *2016 IEEE 18th International Conference on e-Health Networking, Applications and Services (Healthcom)*. 2016 IEEE 18th International Conference on e-Health Networking, Applications and Services (Healthcom). Munich, Germany: IEEE, Sept. 2016, pp. 1–5. ISBN: 978-1-5090-3370-6. DOI: 10.1109/HealthCom.2016.7749520. URL: http://ieeexplore.ieee.org/document/7749520/ (visited on 09/15/2024).

[118] Haozhe Xie et al. "Pix2Vox++: Multi-scale Context-aware 3D Object Reconstruction from Single and Multiple Images". In: (2020). Publisher: arXiv Version Number: 2. DOI: 10.48550/ARXIV.2006.12250. URL: https://arxiv.org/abs/2006.12250 (visited on 09/15/2024).

[119] David Stojanovski et al. "Efficient Pix2Vox++ for 3D Cardiac Reconstruction from 2D Echo Views". In: *Simplifying Medical Ultrasound*. Ed. by Stephen Aylward et al. Vol. 13565. Series Title: Lecture Notes in Computer Science. Cham: Springer International Publishing, 2022, pp. 86–95. ISBN: 978-3-031-16901-4 978-3-031-16902-1. DOI: 10.1007/978-3-031-16902-1_9. URL: https://link.springer.com/10.1007/978-3-031-16902-1_9 (visited on 09/15/2024).

[120] Jaroslaw Tuszynski. *Triangle/Ray Intersection*. Sept. 25, 2024. URL: https://www.mathworks.com/matlabcentral/fileexchange/33073-triangle-ray-intersection (visited on 09/25/2024).

[121] *Ellipsoid fit - File Exchange - MATLAB Central*. URL: https://www.mathworks.com/matlabcentral/fileexchange/24693-ellipsoid-fit (visited on 09/25/2024).

[122] The MathWorks Inc. *pcregistericp*. URL: https://www.mathworks.com/help/vision/ref/pcregistericp.html (visited on 09/25/2024).

[123] *Categories of arrhythmias*. en. https://www.texasheart.org/heart-health/heart-information-center/topics/categories-of-arrhythmias/. Accessed: 2024-10-5. Dec. 2017.

[124] Thomas Bartel et al. "Why is intracardiac echocardiography helpful? Benefits, costs, and how to learn". en. In: *Eur. Heart J.* 35.2 (Jan. 2014), pp. 69–76.

[125] Lisa M Verheul et al. "State-of-the-art multimodality imaging in sudden cardiac arrest with focus on idiopathic ventricular fibrillation: A review". en. In: *J. Clin. Med.* 11.16 (Aug. 2022), p. 4680.

[126] Lea Melki et al. "Localization of Accessory Pathways in Pediatric Patients With Wolff-Parkinson-White Syndrome Using 3D-Rendered Electromechanical Wave Imaging". In: *JACC: Clinical Electrophysiology* 5.4 (Apr. 2019), pp. 427–437. ISSN: 2405500X. DOI: 10.1016/j.jacep.2018.12.001. URL: https://linkinghub.elsevier.com/retrieve/pii/S2405500X18309757 (visited on 09/23/2024).

[127] Charlie Nash. *nricp: Matlab implementation of non-rigid iterative closest point*. en. Accessed: 2024-09-23. 2015. URL: https://github.com/charlienash/nricp.